

**ADVANCED SENSOR FUSION AND
VIBRATION CONTROL TECHNOLOGIES FOR
ULTRA-HIGH DENSITY HARD DISK DRIVES**

BIN HU

NATIONAL UNIVERSITY OF SINGAPORE

2016

**ADVANCED SENSOR FUSION AND VIBRATION CONTROL
TECHNOLOGIES FOR ULTRA-HIGH DENSITY HARD DISK
DRIVES**

BIN HU

(B. Eng. (Hons.), National University of Singapore)

**A DISSERTATION SUBMITTED
FOR THE DEGREE OF DOCTOR OF PHILOSOPHY
DEPARTMENT OF ELECTRICAL AND COMPUTER
ENGINEERING
NATIONAL UNIVERSITY OF SINGAPORE**

2016

Supervisors:

Assistant Professor Pang Chee Khiang, Justin, Main Supervisor
Dr. Jie Wan, Co-Supervisor, Western Digital Corporation

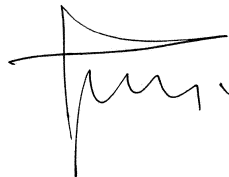
Examiners:

Associate Professor Tan Kok Kiong
Associate Professor Abdullah Al Mamun
Dr. Jinchuan Zheng, Swinburne University of Technology

Declaration

I hereby declare that this thesis is my original work and it has been written by me in its entirety. I have duly acknowledged all the sources of information which have been used in the thesis.

This thesis has also not been submitted for any degree in any university previously.

A handwritten signature in black ink, consisting of a stylized 'H' followed by a series of loops and a final flourish.

Bin Hu

29 September 2016

Acknowledgements

Pursuing a Ph.D. is similar to conquering Mount Everest: both are immense tasks, risky, and inherently-privileged pursuits in life. Knowledge, logic, intuition and perseverance are the climbing tools; friendship and love are the oxygen; and advisers are the Sherpas. When I stand on the summit at the end of the hard work, breathlessly enthralled with the beautiful scenery, I realize that it is that another critical factor helped to bring about my success: teamwork. Words are never enough, but I nevertheless wish to extend my gratitude to the following people.

First of all, I am grateful to my advisor, Prof. Pang Chee Khiang, Justin. I am indebted to him for his strong support, guidance and faith. His rigour, professionalism and constant striving for excellence have been great lessons for me. I have appreciated his help at critical moments of my Ph.D. journey. Without him, I would not have been able to study in such a privileged program, nor would this dissertation have been possible.

Special thanks are due to my co-advisor, Dr. Jie Wan. I am amazed by his curious mind, deep expertise, openness and can-do attitude. When I experience setbacks, he is always there to cheer me up and offer a helping hand. I have greatly enjoyed our wide-ranging discussions about data storage and general mechatronic systems. I will continue to learn from him whenever possible.

My profound gratitude also goes to Dr. Guoxiao Guo for his advice, help and encouragement. He has set up an excellent platform for me to conduct research and provided effective project sponsorship in the company. I admire him for his wisdom, values and philosophies. He is a great teacher who has had a huge influence on me in many ways.

I would like to thank my managers Dr. Shuyu Cao, Dr. Jianyi Wang and Mr. Jern Khang Tan for their strong support in the main phases of my project. I am grateful to my manager, Dr. Zhiyong Jia, for his steadfast support and kind understanding during my dissertation period. I am thankful to my colleagues Dr. Hui Li, Dr. Jun Xu, Dr. Young-Hoon Kim and Ms. Wai Ee Wong for many interesting knowledge-sharing sessions. I thank my peers Mr. Kun Ma, Mr. Junpeng Niu and Mr. Chih Wei Ling for their exchanges of feelings. My thanks also go to Mr. Richard Peh, Dr. Xiaoqiong Wang and Mr. Conan Toh for many interesting and informative coffee chats. I wish them all the best in their future endeavours.

I would like to take this opportunity to record my sincere thanks to all the staff in Western Digital Corporation who have helped me in one way or another, especially the intellectual property lawyers Mr. David Chan, Mr. Brendan Hanley and Ms. Tiffany Chang for speedy review and clearance of my papers. My thanks go to my seniors Dr. Yan Zhi Tan, Mr. Hengchao Yan, Mr. Weili Yan, Mr. Haiyue Zhu and my labmate Mr. Tommy Yip at National University of Singapore for their encouragements. I appreciate the work of lab technician, Mdm. Vathi, for arranging all the logistics for my qualifying exams.

I would like to say a heartfelt thank you to my parents, Mr. Guodong Hu and Mrs. Shuhua Li, for their upbringing, love and support. I must thank my wife Ms. Xin Li for her unconditional love and almost unbelievable support. They are the most important people in my world. I dedicate this dissertation to them.

Finally, I gratefully acknowledge NUS for admitting me to the Industrial Postgraduate Program (IPP). This invaluable financial support allows me to concentrate on my research and realign my career goals. I feel fortunate to be selected as an IPP trainee because of the opportunity it has given me to conduct research with a deeper industrial focus.

Nomenclature

AIDSSA	Asymmetrical Indirect-Driven Self-Sensing Actuation
AMD	Active Mode Damping
DAC	Digital-to-Analog Converter
DDSSA	Direct-Driven Self-Sensing Actuation
DMS	Decoupled Master Slave
EIDSSA	Enhanced Indirect-Driven Self-Sensing Actuation
HDD	Hard Disk Drive
HOM	Head-on-Media
HOR	Head-on-Ramp
ID	Inner Disk
IDSSA	Indirect-Driven Self-Sensing Actuation
LTI	Linear Time-Invariant
MD	Middle Disk
NRRO	Non-Repeatable Runout
OD	Outer Disk
ODCS	Outer Disk Crash Stop
PES	Position Error Signal

PPF	Positive Position Feedback
PZT	Pb-Zr-Ti
RRO	Repeatable Runout
SSA	Self-Sensing Actuation
SNR	Signal-to-Noise Ratio
SSD	Solid-State Drive
TRO	Total Runout
VCM	Voice Coil Motor
ZOH	Zero-Order Hold

Contents

Declaration	i
Acknowledgements	ii
Nomenclature	v
Summary	xi
List of Tables	xiii
List of Figures	xiv
1 Introduction	1
1.1 Technological Trend of Data Storage	2
1.2 Dual-Stage Hard Disk Drives	4
1.2.1 Head-Positioning Mechanism	7
1.2.2 Sensor Fusion	9
1.3 Motivation of Dissertation	12
1.4 Contributions and Organization	13
2 Self-Sensing Actuation for Piezoelectric-Actuated Systems	16

2.1	Background	17
2.2	Self-Sensing Circuit Topologies	19
2.2.1	Conventional Indirect-Driven Self-Sensing Actuation	22
2.2.2	Proposed Enhanced Indirect-Driven Self-Sensing Actuation	24
2.2.3	Proposed Asymmetrical Indirect-Driven Self-Sensing Actuation	32
2.3	Sensitivity Analysis in PZT Active Suspensions	37
2.3.1	Actuation Sensitivity	40
2.3.2	Self-Sensing Sensitivity	41
2.3.3	Trade-offs in Physical Dimensions and Properties	42
2.4	Summary	43
3	Earliest Switch-on of Dual-Stage Actuation	44
3.1	Background	44
3.2	State-Space Representation	46
3.2.1	Dynamic Modeling of Dual-Stage Servo Systems	46
3.2.2	Saturation of Secondary Actuators	48
3.2.3	Switch-on Conditions of Secondary Actuators	49
3.3	Proposed Earliest Switch-on Scheme	50
3.3.1	Maximum Output Admissible Set	50
3.3.2	Algorithm to Determine Saturation-Free Region	51
3.3.3	Design Procedures	54
3.4	Simulation Results and Discussions	56

3.5	Summary	63
4	Improved Rejection of Audio-Induced Vibrations	65
4.1	Background	65
4.2	Head Displacement In-situ Estimation	67
4.3	Modified DMS Servo Incorporating EIDSSA	68
4.4	Experimental Results and Discussions	71
4.4.1	Evaluation of EIDSSA	73
4.4.2	Control Performance of DMS Servo Incorporating EIDSSA . .	76
4.5	Summary	85
5	Automatic Head-on-Media Detection	86
5.1	Background	86
5.2	Mechanism of HOM Detection	90
5.2.1	Principles of Operation	90
5.2.2	Relation Between Sensing Voltage and Head Velocity	92
5.3	Proposed HOM Detection Methodology	94
5.3.1	Realization of EIDSSA Circuit	94
5.3.2	Design Procedures	95
5.4	Experimental Results and Discussions	98
5.5	Summary	104
6	Conclusion and Future Work	105

Bibliography	109
List of Publications	129

Summary

With the advancements in magnetic recording technologies, the achievable recording density for perpendicular recording in Hard Disk Drives (HDDs) is reaching the milestone of 1 Tb/in². To support a recording density of more than 10 Tb/in² for the next generation HDDs with specific applications to big data, cloud computing, and data centers, advanced magnetic recording technologies with ultra-high read/write head-positioning accuracies are required. As such, the accuracy of the head-positioning systems needs to be improved and strengthened in the presence of in-drive disturbances and measurement noises, as well as mechanical vibrations in the actuators of dual-stage HDDs. In this dissertation, advanced sensor fusion and vibration control technologies are developed to meet the increasing demand for larger storage capacity by suppressing these vibrations and improving the read/write head-positioning accuracies.

After a brief introduction of technological trend of data storage, literature review on state-of-art head-positioning mechanism, sensor fusion techniques, and motivation of this dissertation will be detailed.

First, the dissertation deals with the circuit topology of self-sensing actuation in piezoelectric-actuated systems. Enhanced Indirect-Driven Self-Sensing Actuation (EIDSSA) is proposed to remove the coupling between actuation and self-sensing func-

tions. Asymmetrical Indirect-Driven Self-Sensing Actuation (AIDSSA) is proposed to extend the self-sensing capability to the entire frequency spectrum with guaranteed actuation performance. In addition, the sensitivity analysis in piezoelectric-actuated systems is performed using the Pb-Zr-Ti (PZT) active suspension in dual-stage HDDs as an example.

Next, the earliest switch-on conditions of secondary actuators are explored in the presence of in-drive disturbances. Using the theory of maximum output admissible set, the saturation boundary of secondary actuators is obtained in terms of Position Error Signal (PES) and Voice Coil Motor (VCM) velocity error. The earliest switch-on scheme is proposed to achieve faster settling with reduced post-seek oscillations.

Then, the dissertation reports the incorporation and integration of advanced self-sensing techniques into practical dual-stage HDDs. The proposed EIDSSA is applied directly to dual-stage HDD servo systems for improved audio-induced vibration rejection capability. Furthermore, a novel method for Head-on-Media (HOM) detection is proposed based on self-sensing techniques. As the method does not require disk spin-up, the risk of data loss due to media scratching can be mitigated significantly.

This dissertation presents original contributions to advanced sensor fusion and vibration control technologies in dual-stage HDDs. As the study is conducted in an industrial environment, the dissertation contains both practical results and in-depth theoretical analysis. These results and analysis may pave the way towards the next generation HDDs with ultra-high head-positioning accuracies.

List of Tables

2.1	Summary of DDSSA, IDSSA, EIDSSA, and AIDSSA	36
2.2	Summary of actuation and self-sensing sensitivity	42
4.1	Values of circuit components for rejection of audio-induced vibrations.	67
4.2	Stability margins and bandwidth with and without EIDSSA.	76
5.1	Values of circuit components for automatic HOM detection.	94
5.2	Statistics of \bar{V}_{HOR} , \bar{V}_{HOM} , and α	103

List of Figures

1.1	HDD technological roadmap showing increasing areal densities [1]. . .	2
1.2	System responsiveness and cost in HDDs and SSDs [2].	3
1.3	Inside view of an HDD [3].	4
1.4	Head suspension assembly in a commercial dual-stage HDD [3]. . .	6
2.1	Direct-Driven SSA bridge circuit.	19
2.2	Conventional Indirect-Driven SSA circuit.	22
2.3	The proposed EIDSSA circuit topology.	25
2.4	A typical realization of EIDSSA for strain sensing.	28
2.5	A typical realization of EIDSSA for strain rate sensing.	29
2.6	A typical realization of EIDSSA for concurrent strain/strain rate sensing.	31
2.7	The proposed AIDSSA circuit topology.	32
2.8	A typical realization of AIDSSA for strain sensing.	34
2.9	Geometric relations in PZT active suspensions.	38
2.10	Off-track displacement due to deformation of PZT elements.	39
3.1	The DMS servo control structure in HDDs.	46
3.2	Switch-on of PZT actuators.	49

3.3	Generation of LUT for the earliest switch-on.	54
3.4	Feasible solution of O_∞ with $u_M \in [-20 \text{ V}, 20 \text{ V}]$	57
3.5	Phase-plane analysis for the earliest switch-on.	58
3.6	PES traces for the earliest switch-on.	59
3.7	Control traces for the earliest switch-on.	60
3.8	PES traces for the earliest switch-on with in-drive disturbances. . . .	61
3.9	Control traces for the earliest switch-on with in-drive disturbances. .	62
3.10	Saturation boundary with $\pm 10\%$ PZT plant gain drift.	63
4.1	Modified DMS servo control structure incorporating EIDSSA.	68
4.2	Frequency response of VCM controller.	70
4.3	Frequency response of PZT controller.	70
4.4	Experimental set-up and system integration.	71
4.5	Time traces of V_s and V_{in}	72
4.6	Frequency responses of PZT active suspension with IDSSA or EIDSSA. .	73
4.7	Frequency response of β in EIDSSA.	74
4.8	High frequency mode detection by EIDSSA.	75
4.9	NRRO during track-following.	77
4.10	RRO during track-following.	77
4.11	Sensitivity transfer function of DMS servos.	78
4.12	NRRO when playing 2.5 kHz sinusoidal by a vibration speaker. . . .	80
4.13	RRO when playing 2.5 kHz sinusoidal by a vibration speaker. . . .	81

4.14	NRRO when playing 3 kHz sinusoidal by a vibration speaker.	82
4.15	RRO when playing 3 kHz sinusoidal by a vibration speaker.	82
4.16	NRRO when playing pink noise by a vibration speaker.	83
4.17	RRO when playing pink noise by a vibration speaker.	84
5.1	A dual-stage HDD with HOM.	87
5.2	Manual HOM detection with X-ray machine.	88
5.3	Damping effect by ODCS structure.	91
5.4	Conventional manual HOM detection method.	96
5.5	Proposed automatic HOM detection method.	97
5.6	HOR detected by the proposed method (Top: sensing voltage V_s ; bot- tom: injection current).	99
5.7	HOM at ID detected by the proposed method (Top: sensing voltage V_s ; bottom: injection signal).	100
5.8	HOM at MD detected by the proposed method (Top: sensing voltage V ; bottom: injection signal).	101
5.9	HOM at OD detected by the proposed method (Top: sensing voltage V ; bottom: injection signal).	102
5.10	\bar{V}_{HOM} and \bar{V}_{HOR} for HOR and HOM at ID, MD, and OD locations. .	103

Chapter 1

Introduction

Due to the spread of big data, cloud computing, and data centers, the global demand for storage devices has continued to grow at an explosive pace. In 2012, the amount of digital data created, replicated, and consumed was 2837 exabytes. It has been forecasted that the data universe will expand to 40000 exabytes by 2020 – 14 times growth in a decade [4]. The unprecedented growing volume of data requires humongous amount of storage spaces to keep it available for as long as it is required, and to archive much of it afterwards. To meet the demand, data storage companies are striving to offer a variety of storage solutions, such as Hard Disk Drives (HDDs), Solid State Drives (SSDs), all-flash array, and hybrid storage. The competition between HDDs and SSDs has driven the technological development to produce storage medium with larger capacity at a cheaper price. As of now, the HDDs remain as the primary repositories for digital contents. The HDDs are expected to keep up their relative advantages over other types of storage medium by steadily improving the recording densities.

1.1 Technological Trend of Data Storage

The first Hard Disk Drive (HDD) was manufactured by International Business Machines (IBM) in 1956 with areal density of only 2000 bits per square inch [5]. With decades of devotion by researchers, the areal density of modern HDDs is reaching the milestone of 1 Terabit per square inch (Tb/in^2). The growth had once been as robust as doubling annually.

The Advanced Storage Technology Consortium (ASTC), an international organization that unites various companies who develop, manufacture, or use HDDs, has unveiled its vision of this marvellous device [6]. The technological roadmap for the areal density of HDDs is presented in Figure 1.1.

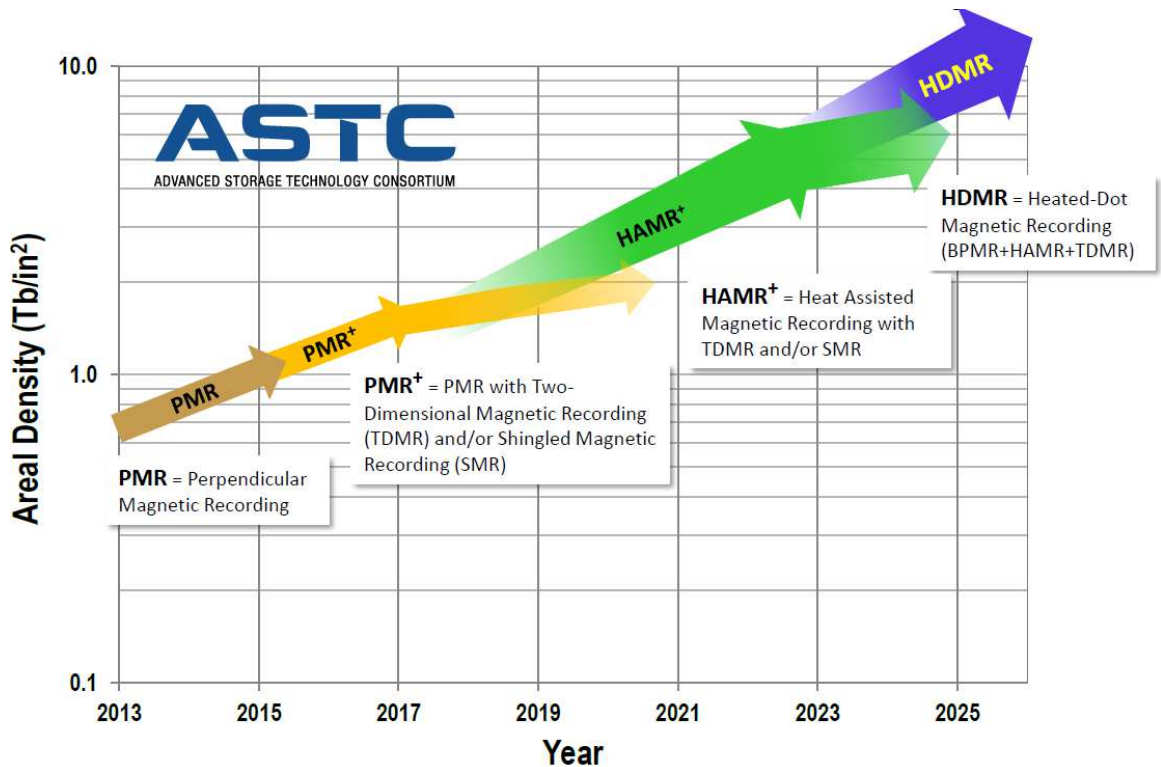


Figure 1.1: HDD technological roadmap showing increasing areal densities [1].

According to the ASTC roadmap, the areal density is expected to rise to 10 Tb/in² in 2025, which translates to HDD capacity of 100 Tb [1]. In the coming years, the HDDs will adopt many new magnetic writing technologies in a bid to bolster the data storage capacity. Heat Assisted Magnetic Recording (HAMR) should be deployed to HDDs by 2017, doubling the average annual growth rate of areal density from the current level of 15% to 30%, followed by the introduction of Heat-Dot Magnetic Recording (HDMR).

Enabled by the leading-edge technologies, the increase in areal density will keep HDDs cost competitive with the SSDs and other alternatives. The approximate costs per Gigabit (Gb) of HDDs and SSDs with consideration of system responsiveness are presented in Figure 1.2.

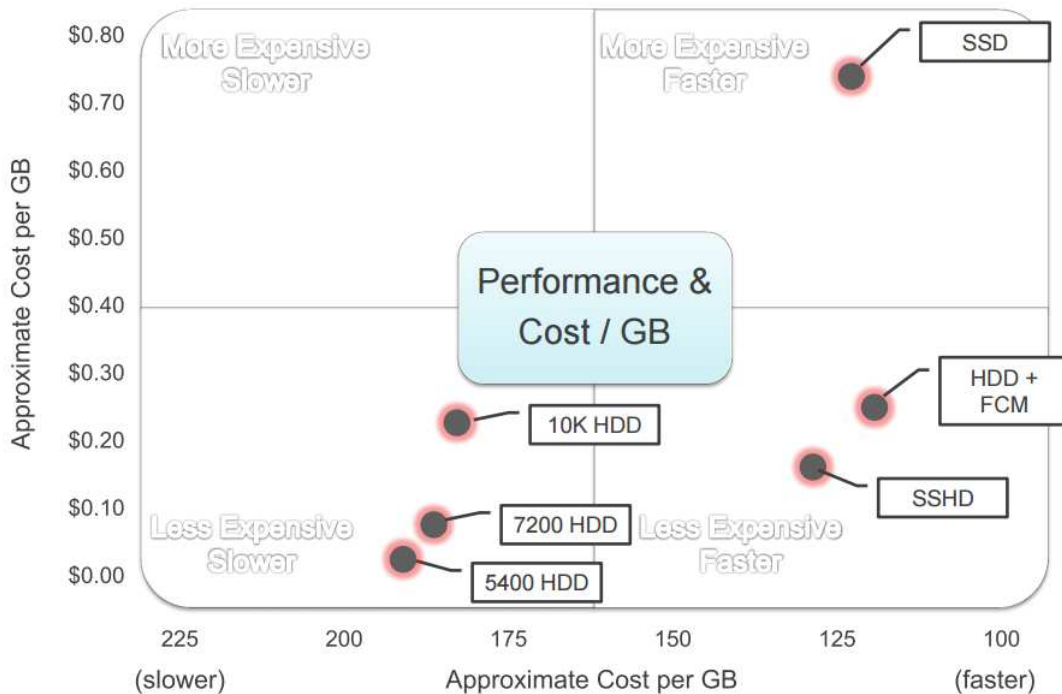


Figure 1.2: System responsiveness and cost in HDDs and SSDs [2].

Flash-based storage products have the upper hand in performance, but HDDs have advantages in terms of cost and capacity. It can be seen from Figure 1.2 that the cost of SSDs in USD/Gb is approximately 5 times higher than that of HDDs. The combination of cost and performance warrants that HDDs will remain relevant as the workhorse storage medium for a long time. Development of HDDs will continue to bring a mixture of increased capacity and improved performance. There are still plenty of opportunities for the amazing technological development to continue.

In view of these trends, this dissertation focuses on the advanced sensor fusion and vibration control technologies to support the future ultra-high density HDDs.

1.2 Dual-Stage Hard Disk Drives

Figure 1.3 shows the inside view of an HDD with the cover removed.

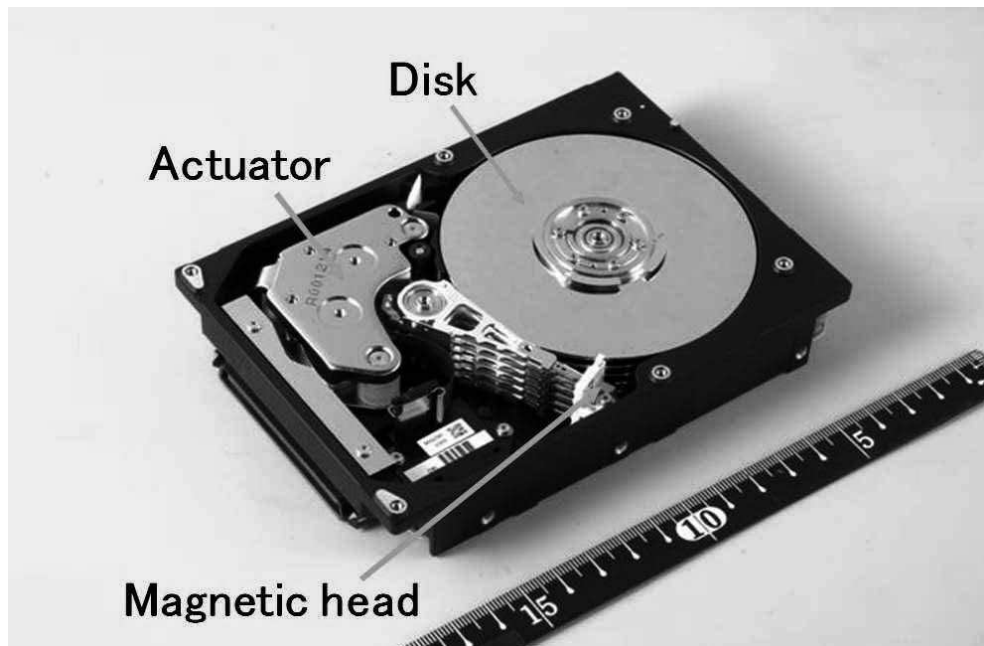


Figure 1.3: Inside view of an HDD [3].

The HDD uses round and flat disks, coated on both sides with a special media material, to store data in the form of magnetic patterns. The disks are mounted with a hole cut in the center and stacked onto a spindle motor shaft. The disks rotate at 15000 Rotation Per Minute (RPM) in high-performance HDDs or 5400 to 7200 RPM in mobile or desktop HDDs. Special electromagnetic read/write heads are mounted onto sliders and employed to write to or read from the disk media. The separation between the head and the disk is maintained by a hydrodynamic bearing, which could be as close as 1 nm. The sliders with heads are mounted onto arms, which are mechanically connected onto a single assembly. The heads are positioned over the disk using an electromagnetic actuator, known as Voice Coil Motor (VCM). A logic board controls the activity of the other components and communicates with the computer.

To improve the head-positioning accuracy, the configuration of dual-stage actuation has been implemented in commercial HDDs. A secondary milli-actuator is placed piggy-back at the arm of primary VCM actuator to displace read/write heads relative to the suspension for fine head-positioning. Depending on where the secondary stage actuator is located, the secondary actuator can be classified into the following categories:

1. the head-based: where the milli-actuator is attached between the slider and the read/write head [7,8];
2. the slider-based: where the milli-actuator is inserted between the suspension and the slider [9–12]; and

3. the suspension-based: where the milli-actuator is placed between the arm of VCM and the suspension [13–16].

The head and slider-based milli-actuators are manufactured by the Microelectromechanical Systems (MEMS) technology, thus also known as MEMS actuators. Nowadays, the companies are shipping mostly suspension-based dual-stage HDDs. In this dissertation, the suspension-based milli-actuator displaced by Pb-Zr-Ti (PZT) elements, or PZT active suspension is used for our study.

A typical 3.5 inch dual-stage HDD with the VCM and PZT active suspension is shown in Figure 1.4.

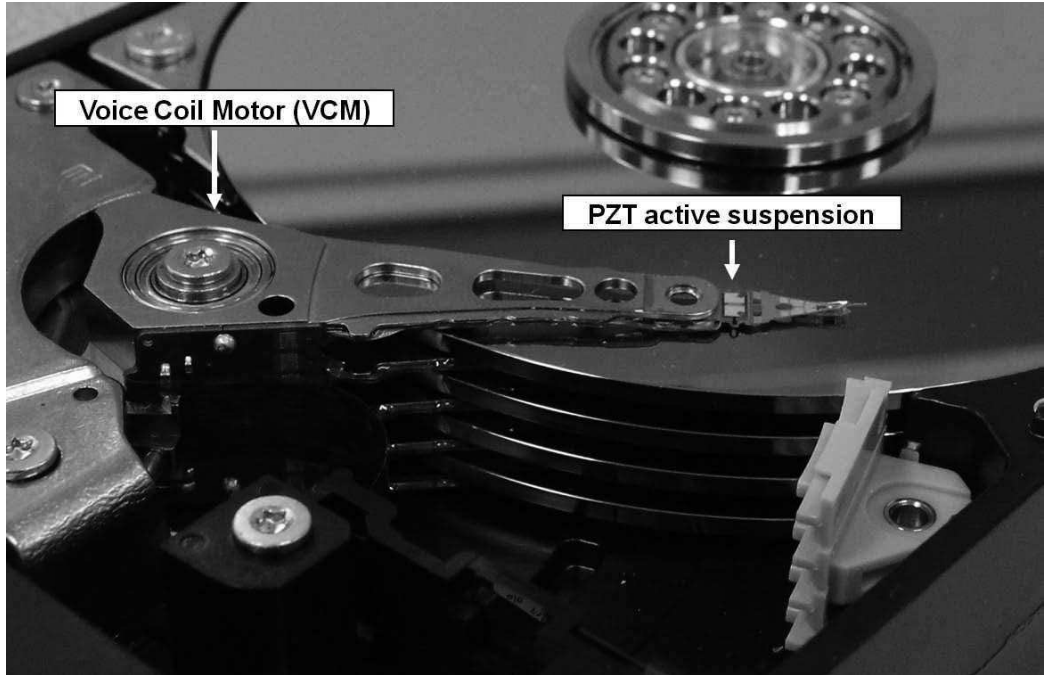


Figure 1.4: Head suspension assembly in a commercial dual-stage HDD [3].

Due to confidentiality, the system identification and plant models are omitted. The VCM is essentially a double integrator with several flexible mechanical resonant

modes of interest. The PZT active suspension can be modeled as a pure gain in a large range of frequencies coupled with several high frequency mechanical resonant modes. Interested readers are referred to [17] on system identification and similar plant models in HDD systems.

1.2.1 Head-Positioning Mechanism

When the HDD is powered up, the disks spin up to a precisely regulated speed and the heads are allowed to move radially over the disk surfaces. Due to the amount of airflow generated by the high speed disk rotation, a very thin air bearing film is generated and hence the heads float on the lubricant of the disks. Accurate and precise control of radial position of the heads is performed by the head-positioning mechanism, a feedback system consisting of heads, VCM and PZT actuators, amplifiers, and controllers.

In HDDs, the Position Error Signal (PES) is the only measurable signal for feedback purpose. During manufacturing, position information is embedded in the servo sectors along the data tracks at equally spaced angles with user data sectors in between [18,19]. The PES is demodulated from the servo sectors by a data channel and obtained in discrete-time format. The sampling rate of PES is $\text{RPM}/60N_s$, where N_s is the number of servo sectors in a track. The frequency of $\text{RPM}/60$ in Hertz is referred to as one harmonic.

During the HDD operation, the head-positioning mechanism moves the read/write heads as fast as possible from one track to another when requested by the host system.

This process is called track-seeking. Once reaching the target track, track-following process will start to regulate the heads precisely over the track in the presence of disturbances and noises. The transition between track-seeking and track-following is called track-settling. It is started when the distance from heads to track is within a pre-defined range of PES.

The track-seeking controller focuses on shortening the seeking time and reducing the seek-induced vibrations [20–25]. The track-settling process is desired to be as fast and smooth as possible [26–32]. Both classical and modern control techniques are widely used for precise track-following [33–39]. The track-following performance is evaluated by the 3σ value of the PES, which can be further classified into Repeatable Runout (RRO) and Non-Repeatable Runout (NRRO) depending on if it is synchronous to disk rotation [17]. The Total Runout (TRO) is the square root sum of the NRRO and RRO values.

A typical job for an HDD can include the following activities:

1. The drive accesses the disk to locate the track, heads, and sector.
2. In most cases the HDD is spinning. If it is not, the spindle motor will be activated to “spin up” the drive to reach the operating speed.
3. The logic board instructs the actuator to seek the heads to the target track.
4. When heads are in the correct positions, the controller activates the specified head to begin reading the track while undergoing track-following.
5. The controller board coordinates the information flow between the HDD and buffer and communicates with the HDD interface.

6. The disk spins down and the actuators retract to ramp. Unsuccessful retraction is disastrous as it may cause heads land on the media surface.

1.2.2 Sensor Fusion

In HDD systems, synergistic use of sensors has been extensively studied to enable advanced features for improved head-positioning accuracies. In combination with PES, the additional sensing signal can be employed to reject vibrations and minimize off-track errors. The VCM butterfly mode has been actively damped by attaching strain sensors at the right locations at the base of VCM coil support [40]. Accelerometers have been mounted on the casing to reject external disturbances [41, 42]. Some researchers have developed feed-forward control schemes to deal with disturbances with extraneous sensors, such as accelerometers, velocity transducers, and shock sensors [43–46]. Other methods have been pursued to minimize off-track errors due to contact-induced vibrations and prevent head crashing during head-positioning activities [47–49]. The above-mentioned approaches require extraneous sensory devices. The overall cost might in turn outweigh the actual benefits obtained.

In dual-stage HDDs, various researches have been conducted to develop the PZT active suspension into a sensor. Bulk PZT active suspensions have been modified to employ one PZT strip as the actuator and the other as the sensor to control the vibration modes of the suspension and the voice coil motor arm [50–52]. This configuration is close to a collocated control, despite that the stroke range is halved as an undesired consequence. It has been found that the sensor output signal is prone to

be corrupted by large unwanted contributions from the out-of-plane bending modes vibrations. The PZT active suspension has also been utilized solely as a position sensor for multi-rate active vibration control [53], but the actuation capability of PZT elements is lost. To overcome these limitations, miniaturized strain gauge sensors have been fabricated onto the suspension. The optimal placement to observe the vibration states has been firstly studied in [54]. In the later development, thin-film ZnO sensors have been demonstrated by direct fabrication and implementation onto a suspension structure [55–57]. The performance analysis of thin-film ZnO sensors has been performed in [58]. Though dedicated miniaturized sensors on instrumented suspensions are cheap, they inevitably alter the suspension dynamics and require complicated fabrication process [59].

Given the reversibility of piezoelectric materials, Self-Sensing Actuation (SSA) allows actuation and sensing to be performed simultaneously. The concept is sprouted concurrently in the works of [60] and [61] twenty-four years ago. It has been shown that by applying the same amount of voltage over the piezoelectric elements and a reference capacitor in a bridge circuit, the strain or strain-rate of piezoelectric elements can be obtained. SSA brings the advantages of sensor-actuator collocation as well as weight and space reduction [62]. Over the years, the HDD community has devoted tremendous research efforts to study the SSA technology using the PZT active suspension in dual-stage HDDs. Active vibration controllers by Positive Position Feedback (PPF) and Direct Velocity Feedback (DVF) have been proposed to control the vibrations in the PZT active suspension [63–66]. An analog implementation of controller using SSA in HDDs is reported in [67]. The first successful demonstration

of SSA in dual-stage HDDs under laboratory set-up is archived in [68, 69], where the critical resonant modes are suppressed by Active Mode Damping (AMD). It is worth noting that the above-mentioned SSA techniques are all developed using the original bridge circuit, although the control algorithms differ from one another. Such SSA techniques are Direct-Driven SSA (DDSSA) because the driving voltage is applied directly to the PZT elements [3]. Recently, Indirect-Driven SSA (IDSSA) is developed to achieve robust vibration control at critical resonant modes [70], and its performance has been enhanced in the work of [71] and [72].

Attributed to its unique advantages, SSA technology has drawn wider interests from the fields in nano-positioning, acoustic control, structural damage diagnosis, and aerospace engineering [73–80]. Various improvements have been made to DDSSA in these industries to improve the system stability and control performance, such as in [81, 82]. To deal with the capacitance matching in DDSSA, adaptive mechanism has been proposed to increase the Signal-to-Noise Ratio (SNR) by reducing unwanted feed-through components [83–87]. Readers are kindly referred to [88] for a tutorial of the effects of capacitance change on the system performance and stability. In literature, some other SSA techniques have been developed based on detection of permittivity change and observers [89–93], however the major drawback is that precise model is a *sine qua non* to be practically used.

In spite of the aforementioned advancements, the SSA technology has not gained traction in the HDD industry owing to various practical concerns over prevailing solutions, such as the SNR, plant gain loss introduced by DDSSA and conventional

IDSSA. Most importantly, there are coupling effects between self-sensing and actuation in these methods. As a result, the designs of actuation and self-sensing are dependent on each other. The sensitivity of SSA in piezoelectric-actuated systems also awaits to be established.

1.3 Motivation of Dissertation

The world's first 10 Tb capacity HDD in a standard 3.5 inch form factor has been unveiled by Hitachi Global Storage Technology (HGST), a Western Digital Company [94]. Harnessing the state-of-art technologies such as HelioSeal and Shingled Magnetic Recording (SMR), the design platform to deliver ultra-high density HDDs has been successfully built. With the extension of SMR to Two Dimensional Magnetic Recording (TDMR) combined with Heat Assisted Magnetic Recording (HAMR) technology, it has been predicted that the areal density will reach 10 Tb/in² in 2025 which translates to the capacity of 100 Tb. The next generation HDDs must meet the needs of enterprise markets and coexist with flash-based products by providing high-performance data storage solutions in larger capacity at lower cost.

The ambitious goal necessitates a technological leap in all of the HDD subsystems including the head-positioning system. Performance improvement and cost reduction in the head-positioning system must be performed. Currently, the secondary actuators are activated very late during track-settling owing to the concerns on actuator saturation. The PES remains as the only available positioning information for feedback purpose, although there are two actuators. There is also lack of effective methods

to automatically detect disastrous failures during head-positioning activities.

In modern mechatronic systems, sensors play a key role in enabling advanced features. Through sensor fusion, the additional sensing signals can be used in combination with PES to improve the performance of dual-stage HDD systems. The benefits are obvious, but the design and integration of sensors present multiple challenges to the HDD industry, such as the alteration of dynamics for miniaturized actuators, optimal location of sensor placement, and the associated cost. With the SSA technology, cheap and non-intrusive collocated sensors in nanometer precision can be incorporated and integrated into dual-stage HDD systems. Together with PES, this newly acquired information will be used to achieve high-performance head-positioning in future HDDs.

1.4 Contributions and Organization

This dissertation concentrates on the study and development of high-performance piezoelectric Self-Sensing Actuation (SSA) technology in ultra-high density Hard Disk Drives (HDDs). We will then focus on the incorporation and integration of SSA mechanism into dual-stage HDD systems for enhanced performance in various head-positioning operations.

The original contributions of this dissertation are as follows:

1. Proposal of Enhanced Indirect-Driven Self-Sensing Actuation (EIDSSA) and Asymmetrical Indirect-Driven Self-Sensing Actuation (AIDSSA) to remove the coupling effect between actuation and self-sensing. As a result, the design of

each function can be carried out independently. Attributed to AIDSSA's unique asymmetrical structure, the self-sensing capability has been extended to the entire frequency spectrum. Furthermore, the sensitivity in piezoelectric-actuated systems is analyzed using the PZT active suspension in commercial dual-stage HDDs as an example. Trade-offs in physical dimensions and properties in PZT active suspension are discussed from a sensitivity viewpoint.

2. Exploration of the earliest switch-on conditions of secondary actuators while ensuring non-saturations during track-settling. Based on the Position Error Signal (PES) and Voice Coil Motor (VCM) velocity error, the earliest switch-on scheme is proposed to achieve faster settling with reduced post-seek oscillations.
3. Incorporation of the proposed EIDSSA into practical dual-stage HDD servo systems for improved audio-induced vibration rejection capability. Nano-scale positioning accuracy and self-sensing sensitivity are achieved with in-situ estimation of relative head displacement.
4. Extension of the proposed EIDSSA to establish a novel methodology for Head-on-Media (HOM) detection in drive-qualification process. As the proposed method does not require disk spin-up, it is able to mitigate the risk of media scratching and data loss due to HOM.

The rest of the dissertation is organized as follows:

- Chapter 2 proposes the EIDSSA and AIDSSA circuit topologies for general piezoelectric-actuated systems. The sensitivity analysis is performed using the PZT active suspension in dual-stage HDDs as an example. Trade-offs in phys-

ical dimensions and properties are discussed from a sensitivity viewpoint.

- Chapter 3 explores earliest switch-on conditions of dual-stage actuation during seek-settling process for shortened settling time and reduced post-seek oscillations. The switch-on conditions with and without SSA are discussed.
- Chapter 4 details the incorporation and integration of EIDSSA in dual-stage HDD servo systems for improved rejection of audio-induced vibrations.
- Chapter 5 shows how the PZT active suspension can be used as an actuator and a sensor simultaneously to filter out HOM drives during internal and customer qualification process.
- Chapter 6 summarizes the findings and results of this dissertation and presents some possible future research directions.

Chapter 2

Self-Sensing Actuation for Piezoelectric-Actuated Systems

Self-Sensing Actuation (SSA) allows a single piezoelectric element to be used as an actuator and a sensor simultaneously. To realize the concept, researchers have developed Direct-Driven SSA (DDSSA) and Indirect-Driven SSA (IDSSA) depending on whether the driving voltage is applied directly to piezoelectric elements. In DDSSA and conventional IDSSA, control efforts cannot be fully delivered to piezoelectric elements. The coupling effect between the actuation and self-sensing results in inevitable design dependencies. In this chapter, by establishing a unified approach to quantify the performance of SSA, we propose Enhanced Indirect-Driven SSA (EIDSSA) circuit topology to remove the coupling effects. As a result, the design of actuation and self-sensing can be carried out independently. Further, we propose Asymmetrical Indirect-Driven SSA (AIDSSA) circuit topology to extend the self-sensing capability to the entire frequency spectrum while ensuring uncompromised actuation performance. For simplicity but without loss of generality, we have investigated the sensitivity in piezoelectric-actuated systems by using the Pb-Zr-Ti (PZT) active suspension in commercial Hard Disk Drives (HDDs) as an example. Trade-offs in terms of physical dimensions and properties are discussed from a sensitivity viewpoint.

2.1 Background

Piezoelectric materials find wide applications as sensors or actuators in mechatronic systems. Piezoelectric elements can be used as sensors attributed to the direct piezoelectric effect, where charges are generated upon deformation. They can also be employed as actuators owing to the converse piezoelectric effect, where deformation occurs with applied electric field [95]. Thanks to the fast response and high resolution, piezoelectric elements have gained huge popularity as actuators in nano-positioning systems, such as the Pb-Zr-Ti (PZT) secondary actuators in Hard Disk Drives (HDDs) and piezoelectric tube scanners in atomic force microscopy, to achieve high servo bandwidth and strong disturbance rejection. As sensors, piezoelectric elements have been utilized to achieve improved damping and precise tracking in high-speed nano-positioners [96, 97].

Harnessing the reversibility of piezoelectric materials, Self-Sensing Actuation (SSA) allows piezoelectric elements to be used as actuators and sensors simultaneously. SSA is naturally collocated and it has been shown that collocated control has a number of advantages relating to system stability. As compared to dedicated sensory devices, SSA brings the benefits of weight and space reduction as well as cost saving. It also does not require complicated fabrication process or alter the suspension dynamics.

Through SSA, the strain or strain-rate of the piezoelectric element can be obtained by applying the same amount of voltage over the element and a reference capacitor. To realize the concept, both Direct-Driven SSA (DDSSA) and Indirect-

Driven SSA (IDSSA) techniques have been developed depending on if the driving voltage is applied directly to piezoelectric elements [3]. Over the years, the research on SSA has been primarily focused on the improvement of DDSSA circuit. For example, additional capacitors are connected in series or in parallel with piezoelectric elements to increase the system stability [81]. Considerable efforts have been spent on the adaptive balancing of capacitance in the bridge circuit. The adaptation is effective in improving the self-sensing Signal-to-Noise Ratio (SNR) by reducing any unwanted feed-through components. According to [84], the error due to mismatching of capacitance can be reduced to as small as 3.7 %. Note that the mismatching is usually a result of varying environmental and operating conditions, such as temperature change. In applications where the environmental conditions are controlled, mismatching is not considered as a show-stopper in furthering the development of SSA technology. The primary hurdle of DDSSA and conventional IDSSA is the coupling effects between actuation and self-sensing, which results in inevitable plant gain loss and design dependencies.

In this chapter, Enhanced Indirect-Driven SSA (EIDSSSA) is proposed to remove the coupling effects between actuation and self-sensing [71]. Further, Asymmetrical Indirect-Driven SSA (AIDSSA) is proposed to extend the self-sensing capability to the entire frequency range while guaranteeing uncompromised actuation performance. For both circuits, nanometer-scale positioning accuracy and self-sensing sensitivity can be achieved. Using the PZT active suspension in commercial HDDs as an example, we have derived the sensitivity from self-sensing signal to head displacement for the special sensors.

2.2 Self-Sensing Circuit Topologies

To realize the concept of SSA, it is essential to decouple the effect due to the applied control voltage from the output signal of the piezoelectric elements, leaving only the signal resulting from the deformation. The decoupling operation is performed by a bridge circuit. The Direct-Driven SSA (DDSSA) bridge circuit is shown in Figure 2.1, where the input signal V_{in} is applied across the entire bridge circuit [3].

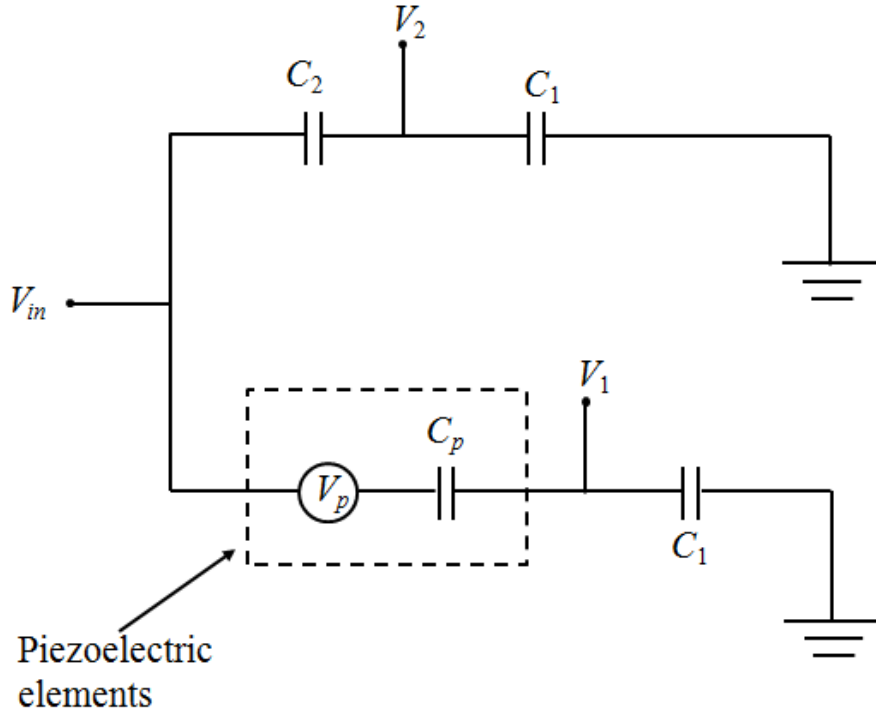


Figure 2.1: Direct-Driven SSA bridge circuit.

In Figure 2.1, piezoelectric elements are modeled as a self-sensing voltage source V_p in series with an equivalent capacitor C_p . The circuit can be analyzed by deriving

the Laplace transform of V_1 and V_2 as follows:

$$V_1(s) = \frac{C_1}{C_1 + C_p} [V_{in}(s) - V_p(s)], \quad (2.1)$$

$$V_2(s) = \frac{C_1}{C_1 + C_2} V_{in}(s). \quad (2.2)$$

The output voltage $V_s(s)$ is obtained as

$$\begin{aligned} V_s(s) &= V_2(s) - V_1(s) \\ &= \left(\frac{C_1}{C_1 + C_2} - \frac{C_1}{C_1 + C_p} \right) V_{in}(s) + \frac{C_1}{C_1 + C_p} V_p(s). \end{aligned} \quad (2.3)$$

Denote the voltage across the piezoelectric elements as V_a . The performance of the DDSSA bridge circuit in terms of actuation and self-sensing can be analyzed by the following pair of equations as

$$\begin{cases} V_a(s) = \frac{C_p}{C_1 + C_p} V_{in}(s), \\ V_s(s) = \left(\frac{C_1}{C_1 + C_2} - \frac{C_1}{C_1 + C_p} \right) V_{in} + \frac{C_1}{C_1 + C_p} V_p(s). \end{cases} \quad (2.4)$$

From (2.4), it can be seen that the actuation efforts as represented by $V_{in}(s)$ are not fully delivered to the piezoelectric elements but by a factor of $\frac{C_p}{C_1 + C_p}$. Moreover, the effects of actuation and self-sensing are coupled together due to the common terms C_1 and C_p appearing in both equations. Even if the feed-through components from $V_{in}(s)$ are perfectly eliminated in $V_s(s)$ by choosing $C_2 = C_p$, $V_s(s)$ still cannot represent $V_p(s)$ well because $V_p(s)$ is attenuated by a factor of $\frac{C_1}{C_1 + C_p}$ in the entire frequency spectrum. Considering that the magnitude of $V_p(s)$ is already very small, the attenuating effect leads to further degraded Signal-to-Noise Ratio (SNR). It is worth noting that these limitations exist in general DDSSA circuits.

The afore-going approach can be generalized and applied to analyze any SSA circuit by formulating a pair of unified equations:

$$\begin{cases} V_a(s) = \gamma V_{in}(s), \\ V_s(s) = [\alpha V_{in}(s) + \beta V_p(s)] \kappa, \end{cases} \quad (2.5)$$

where the coefficients of α , β , γ , and κ describe decoupling, self-sensing, actuation, and amplification, respectively. The first equation in (2.5) is referred to as actuation performance equation, and the second to as self-sensing performance equation. Throughout the dissertation, the performance of SSA circuits is specified and evaluated using the proposed pair of unified equations.

Correspondingly, the design requirements can be specified by the set $P = \{\alpha, \beta, \gamma, \kappa\}$, where each element in P carries an explicit physical meaning. In general, a high-performance SSA circuit should possess the following properties:

1. α should be close to zero to ensure minimal feed-through component in $V_s(s)$;
2. β should be close to 100% in the frequency range of interest so that $V_s(s)$ can sufficiently represent and resemble $V_p(s)$;
3. γ must be 100% to ensure that $V_{in}(s)$ is fully delivered to piezoelectric elements.
As $\gamma = 100\%$, the designs of actuation and self-sensing become independent;
and
4. κ should be in a proper range to meet both SNR and sampling resolution requirements, if any.

2.2.1 Conventional Indirect-Driven Self-Sensing Actuation

Figure 2.2 presents the conventional Indirect-Driven SSA (IDSSA) circuit. In IDSSA, active components, such as operational amplifiers, are used to drive the piezoelectric elements indirectly [70]. With additional capacitors and resistors placed in the feedback loop of operational amplifiers, the circuit acts as a high-pass filter after differential amplification. The design is able to improve the self-sensing performance by providing higher SNR measurement and wider self-sensing bandwidth.

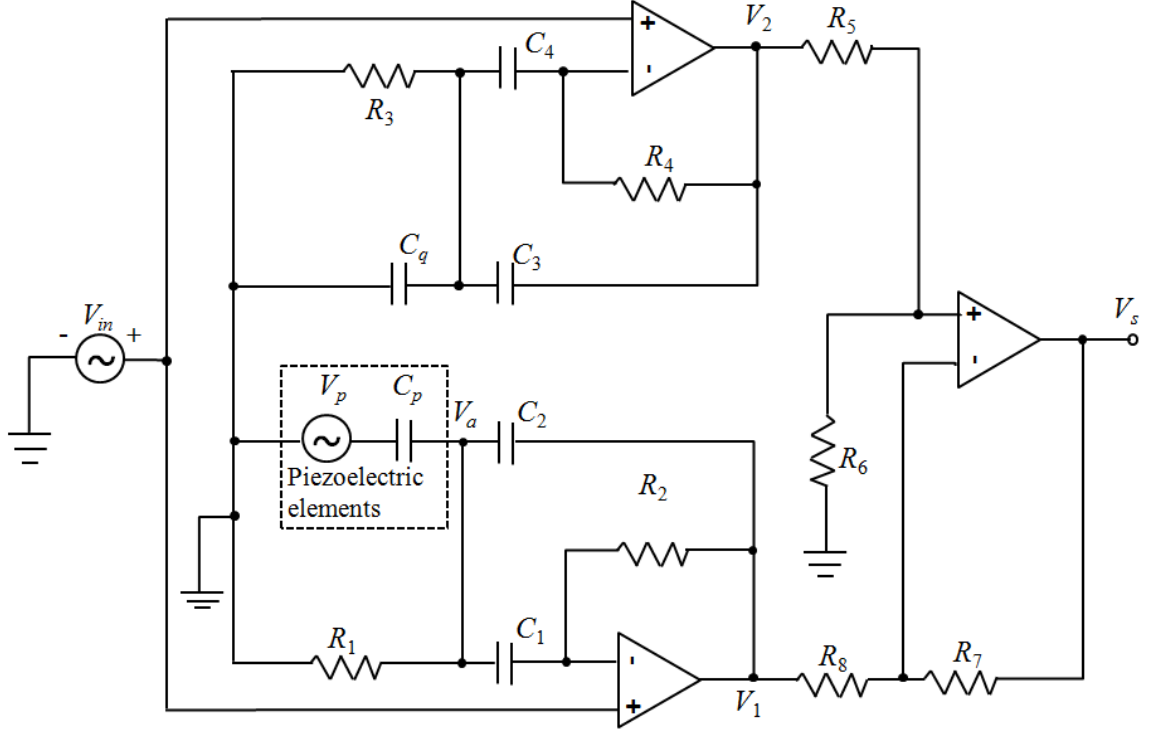


Figure 2.2: Conventional Indirect-Driven SSA circuit.

The self-sensing voltage V_p generated from the strain of piezoelectric elements can be decoupled from V_{in} as shown in the following derivations. The Laplace transform

of V_1 and V_2 can be derived as

$$\begin{aligned} V_1(s) &= \left[1 + \frac{s^2 C_1 C_p R_1 R_2}{s^2 C_1 C_2 R_1 R_2 + s(C_p + C_1 + C_2)R_1 + 1} \right] V_{in} \\ &\quad - \frac{s^2 C_p / C_2}{s^2 + s(C_p + C_1 + C_2)/(C_1 C_2 R_2) + 1/(C_1 C_2 R_1 R_2)} V_p(s), \\ V_2(s) &= \left[1 + \frac{s^2 C_3 C_q R_3 R_4 + s C_3 R_4}{s^2 C_3 C_4 R_3 R_4 + s(C_q + C_3 + C_4)R_1 + 1} \right] V_{in}, \end{aligned}$$

and the output of the IDSSA circuit $V_s(s)$ is obtained as

$$V_s(s) = \frac{R_6}{R_5 + R_6} \frac{R_7 + R_8}{R_8} V_2(s) - \frac{R_7}{R_8} V_1(s). \quad (2.6)$$

If the components in Figure 2.2 are chosen such that $C_1 = C_2 = C_3 = C_4 = C_p = C_q$, $R_1 = R_2 = R_3 = R_4$, $R_5 = R_8$, and $R_6 = R_7 = gR_5$, where g is the gain of the differential amplifier, the bridge circuit is balanced and $V_p(s)$ is decoupled from $V_{in}(s)$.

The expressions of γ and β for IDSSA can be obtained as

$$\gamma = \frac{s R_1 C_7}{s R_1 (C_7 + C_p) + 1}, \quad (2.7)$$

$$\beta = \frac{s^2 k}{s^2 + s(C_1 + C_2 + C_p)/(C_1 C_2 R_2) + 1/(C_1 C_2 R_1 R_2)}. \quad (2.8)$$

Based on (2.7) and (2.8), we find that the conventional IDSSA circuit has the following fundamental limitations:

1. significant gain loss and phase distortion in the whole frequency range by the transfer function of γ in the actuation path;
2. inevitably reduced stroke yielding degraded actuation capability; and
3. coupled actuation and self-sensing performances resulting in design dependency.

These limitations are the obstacles to the development of IDSSA in practical systems. Usually, new features are patched to systems in an ‘add-on’ manner where regression of baseline performance, such as reduced stroke, is intolerable, not to mention the unwanted coupling effect.

The conventional IDSSA circuit is required to be enhanced to remove the coupling effect in γ and β , so that the designs of actuation and self-sensing can be carried out independently. In addition, β should be easily tunable for optimized performance. If possible, β should have the self-sensing capability in the entire frequency spectrum.

2.2.2 Proposed Enhanced Indirect-Driven Self-Sensing Actuation

Figure 2.3 presents the proposed Enhanced Indirect-Driven SSA (EIDSSA) circuit topology. Z_1 to Z_6 denote impedances of particular nodes. Piezoelectric elements, represented by V_p in series with C_p , are indirectly driven by V_{in} . I_q , I_3 , and I_5 denote the electric currents. The impedances Z_1 and Z_2 are placed into the network aiming primarily to prevent the DC-drift phenomenon. V_a is the voltage delivered to piezoelectric elements. V_1 and V_2 are fed into a cascading system which consists of a differential amplifier and its related electronics to produce the output signal V_s . No electrical networks exist in the path between the negative terminals of operational amplifiers and the driving point.

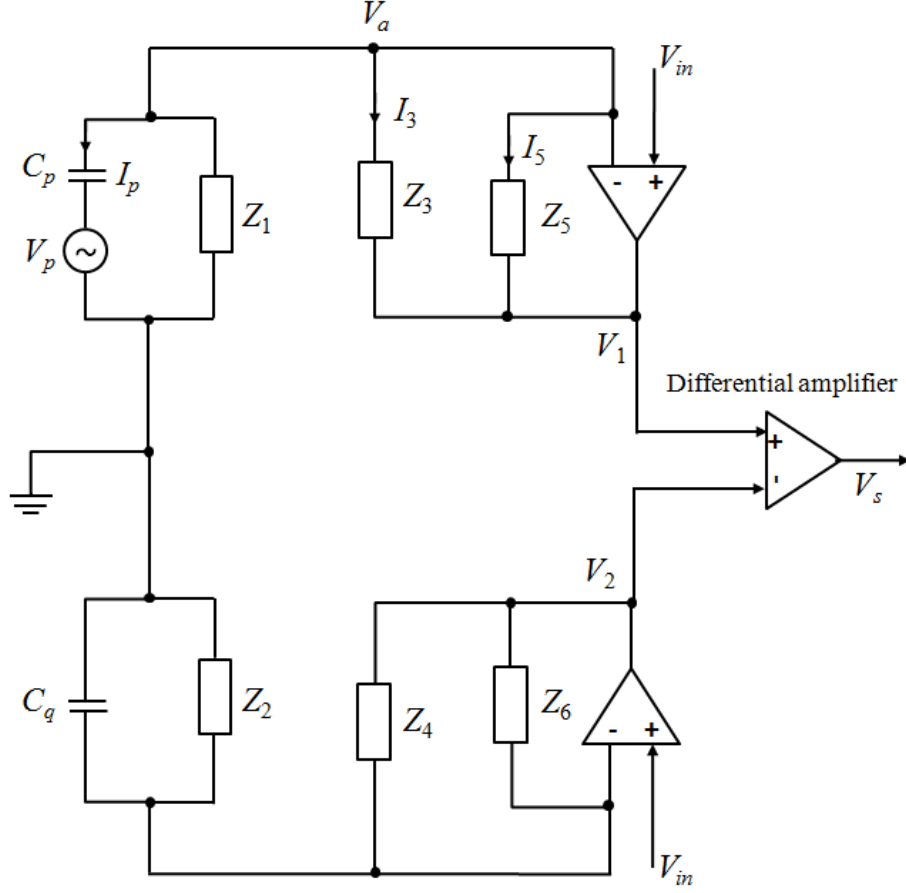


Figure 2.3: The proposed EIDSSA circuit topology.

Referring to Figure 2.3, according to Kirchoff's voltage law, we have

$$I_3 = \frac{Z_5}{Z_3} I_5. \quad (2.9)$$

Since the positive and negative terminals of operational amplifiers are virtually shorted, it holds that

$$I_p = s(V_{in} - V_p)C_p, \quad (2.10)$$

where s denotes the Laplace operator.

By Kirchoff's current law, we have

$$I_p + \frac{V_{in}}{Z_1} = I_3 + I_5. \quad (2.11)$$

It follows that

$$I_5 = \frac{Z_3}{Z_3 + Z_5} \left[\frac{sZ_1C_p + 1}{Z_1} V_{in} - sV_pC_p \right]. \quad (2.12)$$

As $V_1 - V_{in} = Z_5I_5$,

$$V_1 = \left[1 + \frac{Z_3Z_5(sZ_1C_p + 1)}{Z_1(Z_3 + Z_5)} \right] V_{in} - \frac{sZ_3Z_5C_p}{Z_3 + Z_5} V_p. \quad (2.13)$$

Similarly, it can be derived that

$$V_2 = \left[1 + \frac{Z_4Z_6(sZ_2C_q + 1)}{Z_2(Z_4 + Z_6)} \right] V_{in}. \quad (2.14)$$

Let the gain of the differential amplifier be unity, or $\kappa = 1$, it satisfies that

$$V_s = V_2 - V_1. \quad (2.15)$$

Substitution of (2.13) and (2.14) into (2.15) yields

$$V_s = \left[\frac{Z_4Z_6(sZ_2C_q + 1)}{Z_2(Z_4 + Z_6)} - \frac{Z_3Z_5(sZ_1C_p + 1)}{Z_1(Z_3 + Z_5)} \right] V_{in} + \frac{sZ_3Z_5C_p}{Z_3 + Z_5} V_p. \quad (2.16)$$

If the components in Figure 2.3 are chosen such that $Z_1 = Z_2$, $Z_3 = Z_4$, $Z_5 = Z_6$, and $C_p = C_q$, the bridge circuit is balanced and $V_p(s)$ is decoupled from $V_{in}(s)$.

The expressions of γ and β for EIDSSA circuit can be obtained as

$$\gamma = 100\%, \quad (2.17)$$

$$\beta = \frac{sZ_3Z_5C_p}{Z_3 + Z_5}. \quad (2.18)$$

Since $\gamma = 100\%$, the actuation by EIDSSA is gain-lossless. The coupling effect between actuation and self-sensing is elegantly removed in totality. As a result, the design of self-sensing can be carried out independently from actuation.

The expression of β is made up of impedances Z_3 , Z_5 , and capacitance C_p . The impedances Z_1 and Z_2 do not contribute to the self-sensing performance. This is attributed to fact that Z_1 and Z_2 are placed in the network aiming primarily to prevent the DC-drift phenomenon.

Impedances Z_1 to Z_6 in the proposed EIDSSA can be realized differently for desired characteristics. For example, Z_1 to Z_6 can be chosen to be capacitors, resistors, short circuits, open circuits or even more complex electrical networks.

Figure 2.4 presents a typical realization of EIDSSA circuit for strain sensing in piezoelectric elements.

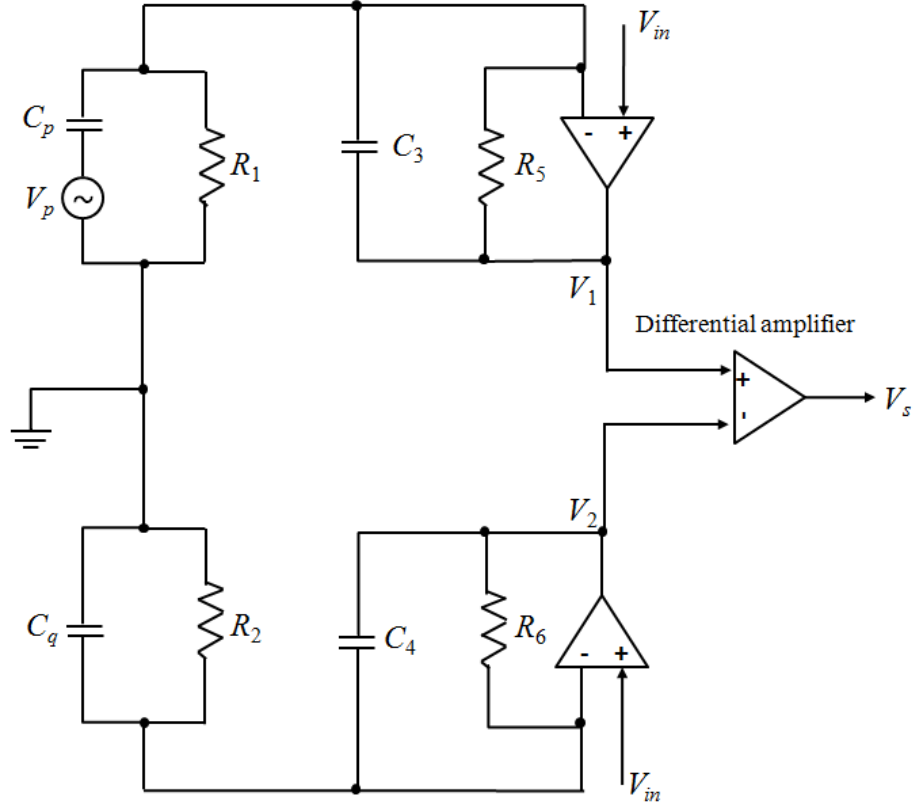


Figure 2.4: A typical realization of EIDSSA for strain sensing.

In Figure 2.4, the impedances Z_1 to Z_6 are realized into resistors R_1 , R_2 , R_5 , R_6 and capacitors C_3 and C_4 , respectively. If we choose $R_1 = R_2$, $C_3 = C_4$, and $R_5 = R_6$, $V_p(s)$ can be decoupled from $V_{in}(s)$. The corresponding expressions of γ and β can be derived as

$$\gamma = 100\%, \quad (2.19)$$

$$\beta = \frac{sR_5C_p}{sR_5C_3 + 1}. \quad (2.20)$$

Similar to conventional IDSSA, the β coefficient as shown in (2.20) exhibits high-pass characteristics in the frequency domain. The component values of R_5 and C_3 should be designed properly to push the corner frequency of β towards lower frequen-

cies for wider sensing bandwidth.

Figure 2.5 presents a typical realization of EIDSSA circuit for strain rate sensing in piezoelectric elements.

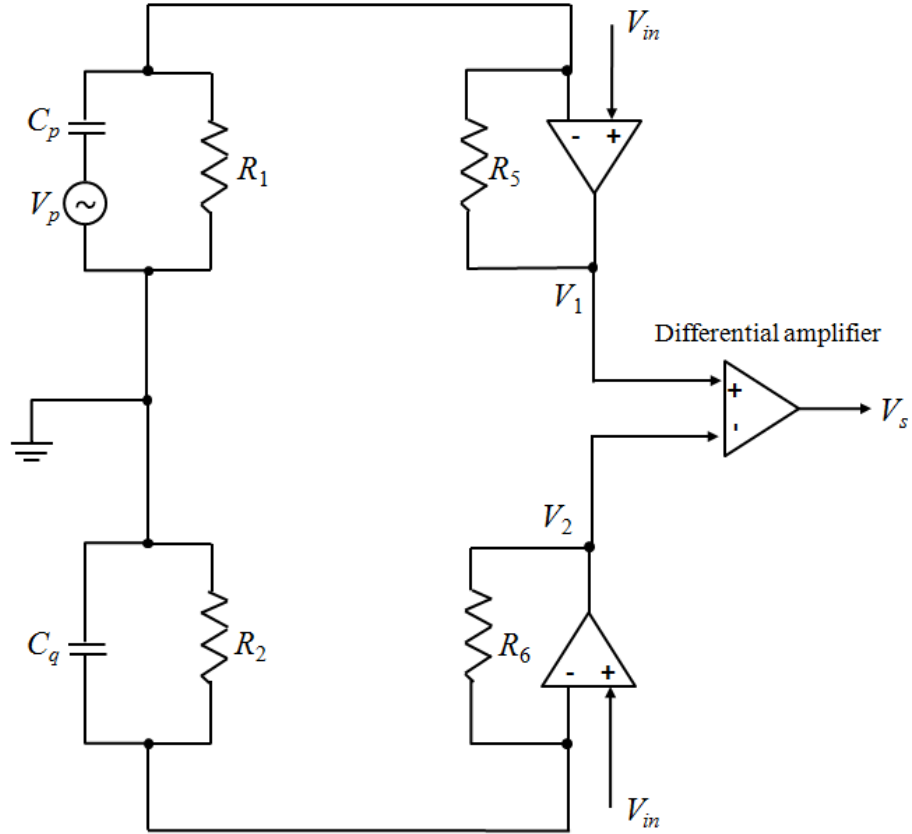


Figure 2.5: A typical realization of EIDSSA for strain rate sensing.

In Figure 2.5, the impedances Z_1 , Z_2 , Z_5 , and Z_6 are realized into resistors R_1 , R_2 , R_5 , and R_6 , respectively. Z_3 and Z_4 are set to open circuits. If we choose $R_1 = R_2$, $R_5 = R_6$, and $C_q = C_p$, then $V_p(s)$ can be decoupled from $V_{in}(s)$. The corresponding expressions of γ and β can be derived as

$$\gamma = 100\%, \quad (2.21)$$

$$\beta = sR_5C_p. \quad (2.22)$$

Based on (2.22), it can be seen that the β coefficient performs first-order derivation. Thus, V_s represents and resembles the strain rate of piezoelectric elements. The gain of β can be easily adjusted using a single resistor R_5 . Note that a cascading low pass filter may be required to prevent undesirable amplification of high frequency noises.

Figure 2.6 presents a realization of EIDSSA for concurrent sensing of the strain and strain rate of piezoelectric elements. In certain mechatronic systems, there may exist two sets of drivers for actuating multiple piezoelectric elements. In Figure 2.6, Driver1 and Driver2 are responsible to actuate the odd and even PZT banks, respectively. In this configuration, V_{s1} and V_{s2} represent the strain rate and strain of piezoelectric elements, respectively.

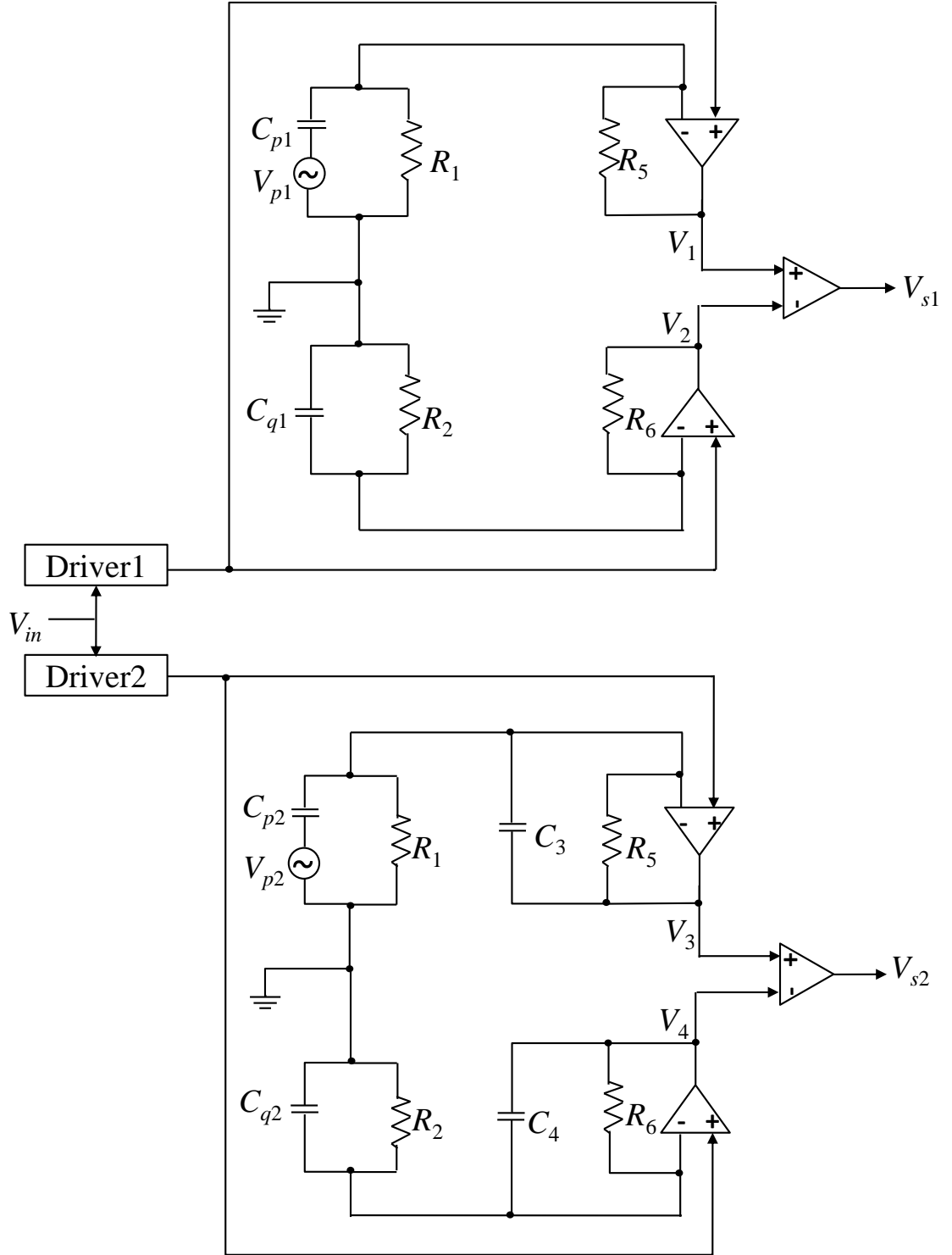


Figure 2.6: A typical realization of EIDSSA for concurrent strain/strain rate sensing.

2.2.3 Proposed Asymmetrical Indirect-Driven Self-Sensing Actuation

In addition to the requirement of $\gamma = 100\%$, the SSA circuit topology is desirable to achieve $\beta = 100\%$ with simplified decoupling conditions. If $\beta = 100\%$, the self-sensing capability can be extended to the entire frequency spectrum. Simplified decoupling conditions will improve the SNR of self-sensing by providing more effective elimination of feed-through components. Figure 2.7 presents the proposed Asymmetrical Indirect-Driven SSA (AIDSSA) circuit topology.

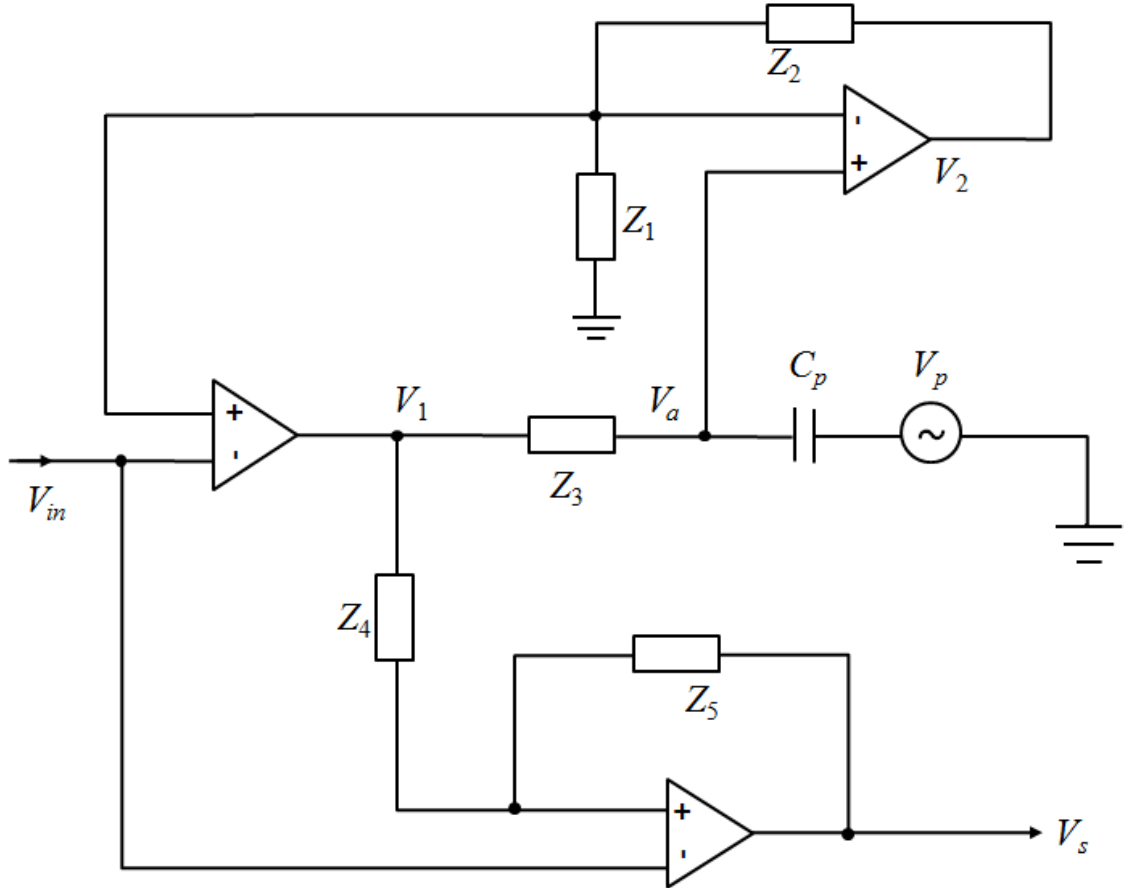


Figure 2.7: The proposed AIDSSA circuit topology.

In Figure 2.7, Z_1 to Z_5 denote the impedances of particular nodes. The piezoelectric elements are represented by an electrically equivalent model with capacitor C_p in series with voltage source V_p . The voltage V_{in} is delivered to piezoelectric elements via the positive and negative terminals of operational amplifiers. The phase loss introduced by the middle operational amplifier can be compensated by using the active feedback in the upper operational amplifier. The phase error can be reduced to almost zero at lower frequencies with dual-matched operational amplifiers.

With reference to Figure 2.7, according to Kirchoff's current law, we have

$$\frac{V_{in} - V_s}{Z_5} = \frac{V_{in} - V_1}{Z_4}, \quad (2.23)$$

and

$$s(V_{in} - V_p)C_p = \frac{V_{in} - V_1}{Z_3}. \quad (2.24)$$

From (2.24),

$$V_1 = (1 - Z_3)V_{in} + sZ_3C_pV_p. \quad (2.25)$$

Substituting (2.25) into (2.23) yields

$$V_s = \left(1 - \frac{sZ_3Z_5C_p}{Z_4}\right)V_{in} + \frac{sZ_3Z_5C_p}{Z_4}V_p. \quad (2.26)$$

If the component values in Figure 2.7 are chosen such that $sZ_3Z_5C_p/Z_4 = 1$, V_p can be decoupled from V_{in} . The expressions of γ and β for AIDSSA are obtained as

$$\gamma = 100\%, \quad (2.27)$$

$$\beta = 100\%. \quad (2.28)$$

Equations (2.27) and (2.28) reveal that the proposed AIDSSA circuit elegantly achieves $\gamma = 100\%$ and $\beta = 100\%$ simultaneously. This is attributed to AIDSSA's unique asymmetrical structure, which is a very significant departure from prior arts. To the best knowledge of the authors, AIDSSA is the first non-bridge type SSA circuit topology, which is able to achieve gain lossless actuation with simplified decoupling conditions.

Figure 2.8 presents a typical realization of AIDSSA circuit for strain sensing in piezoelectric elements.

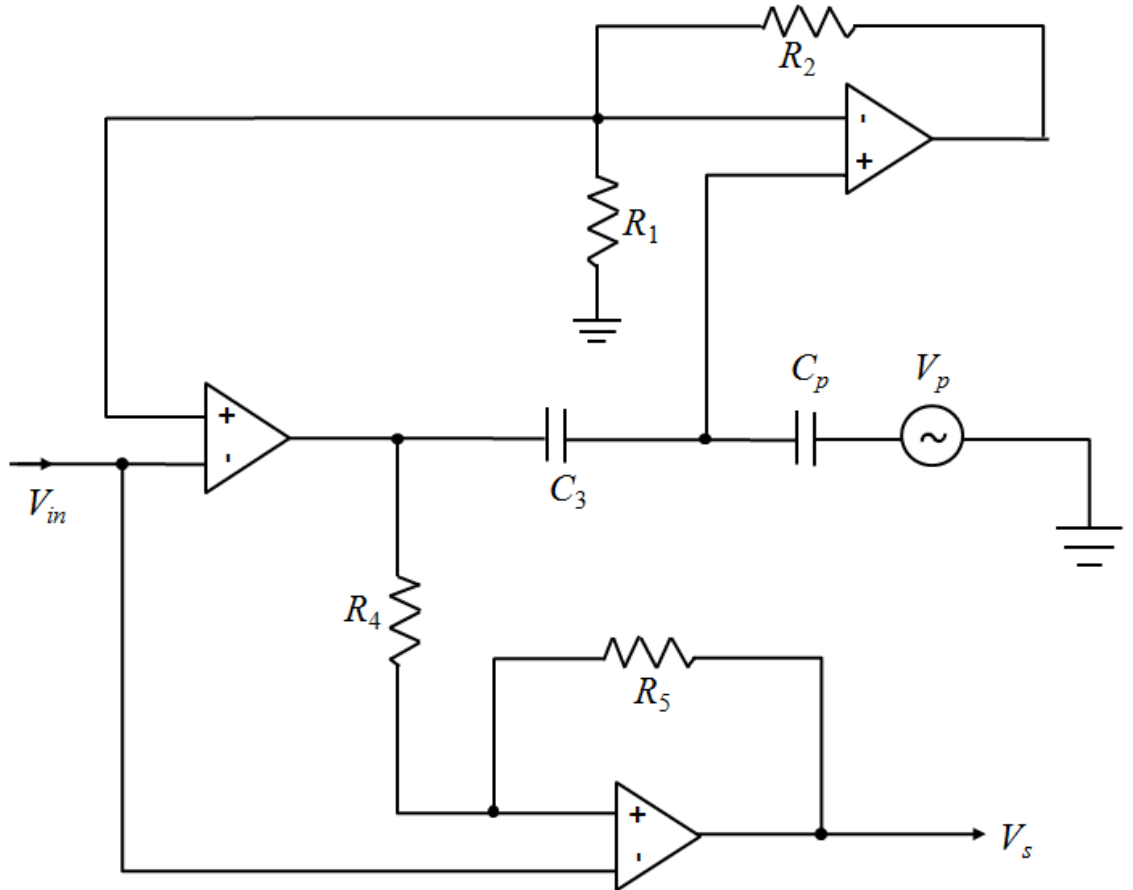


Figure 2.8: A typical realization of AIDSSA for strain sensing.

In Figure 2.8, impedances Z_1 , Z_2 , Z_4 , and Z_5 are realized into resistor R_1 , R_2 , R_4 , and R_5 , respectively. Impedance Z_3 is chosen to be a capacitor C_3 . Resistors R_1 and R_2 do not contribute to self-sensing performance as they are placed into the network primarily to match the phase dynamics. The values of R_1 and R_2 can be arbitrarily chosen as long as the upper operational amplifier is not saturated.

If we choose $C_3 = C_p$ and $R_4 = R_5$, it can be derived that

$$\alpha = 0, \tag{2.29}$$

$$\beta = 100\%, \tag{2.30}$$

$$\gamma = 100\%, \tag{2.31}$$

$$\kappa = 100\%. \tag{2.32}$$

The AIDSSA realization in Figure 2.8 is an all-pass filter and it extends the self-sensing capability in the entire frequency spectrum. A variable gain amplifier can be cascaded to the output of AIDSSA realization for adjusting the overall gain to meet sampling resolution requirements. Should a particular frequency range is of interest, digital or analog filters can be added in series accordingly.

Table 2.1 summarizes the key advantages of the proposed EIDSSA and AIDSSA as compared to the DDSSA and conventional IDSSA.

Table 2.1: Summary of DDSSA, IDSSA, EIDSSA, and AIDSSA

	DDSSA	IDSSA	EIDSSA	AIDSSA
γ	fractional	fractional	100%	100%
β	attenuated	high-pass	high-pass	100%
Coupling effect	coupled	coupled	decoupled	decoupled
Structure	symmetrical	symmetrical	symmetrical	asymmetrical

With reference to Table 2.1, it can be seen that $\gamma = 100\%$ in both EIDSSA and AIDSSA. This means the coupling effect between actuation and self-sensing is removed in totality. As a result, independent design of each function can be carried out and self-sensing related new features can be switched on and off seamlessly without affecting the baseline control loops.

The β coefficient of EIDSSA exhibits high-pass characteristics in the frequency domain. It is preferred to use EIDSSA when the application focuses on high frequency dynamics. If wider sensing bandwidth is needed, the circuit components can be designed to push the corner frequency towards the lower end of frequency spectrum. On the other hand, as $\beta = 100\%$ in AIDSSA, the self-sensing capability is extended into the entire frequency range. In real-world applications, EIDSSA and AIDSSA can be configured into multiple realizations to meet different performance specifications. As compared to conventional IDSSA, the matching conditions have also been significantly simplified in EIDSSA and AIDSSA .

From a circuit topology viewpoint, the proposed EIDSSA is a symmetrical struc-

ture, while AIDSSA is an asymmetrical structure. The unique asymmetrical structure of AIDSSA differs greatly from prior arts. Thus far, AIDSSA is the only non-bridge type SSA solution that is able to achieve $\gamma = 100\%$ and $\beta = 100\%$ simultaneously.

2.3 Sensitivity Analysis in PZT Active Suspensions

In addition to SSA circuit topologies, the design of SSA requires considerations of the mechanical properties of piezoelectric-actuated systems. As an actuator, the primary design objective is to generate large stroke. As a sensor, it is required to be sensitive to structural deformation and produce high SNR sensing signals. Using the PZT active suspension in commercial dual-stage HDDs as an example, the sensitivity in piezoelectric-actuated systems is discussed.

The PZT active suspension can be approximated as a mass-spring damper system. The suspension stiffness is represented by two spring systems with stiffness k . The base plate is fixed and its movable mass including PZT elements and stiffener has an equivalent moment of inertia J . The geometric relations in PZT active suspensions are defined in Figure 2.9.

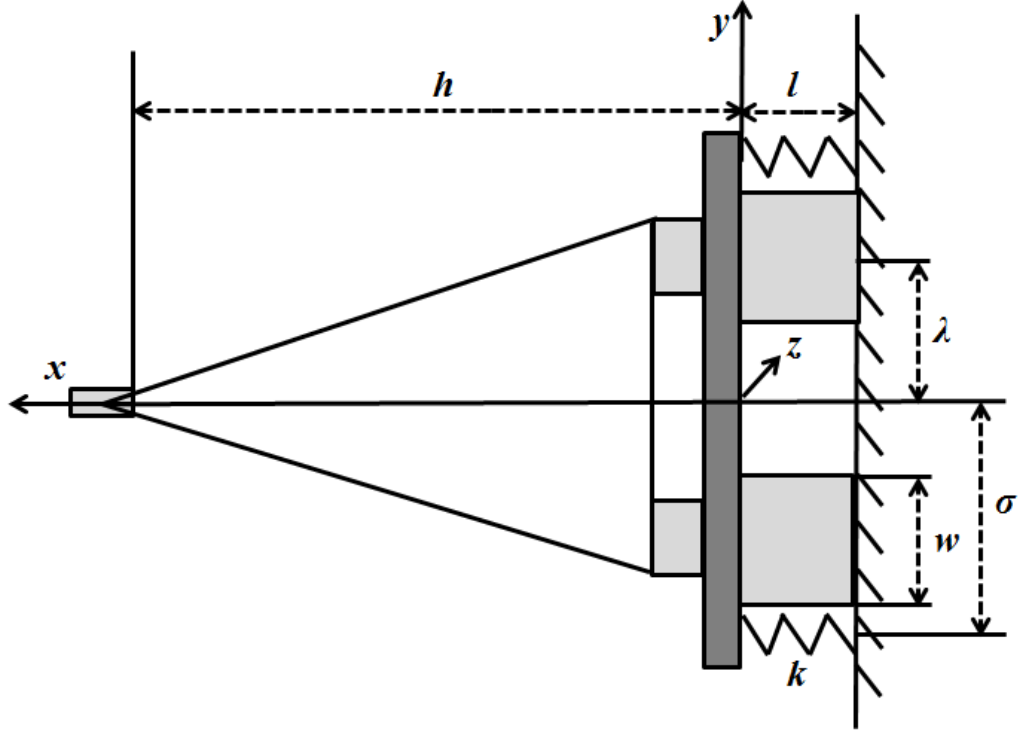


Figure 2.9: Geometric relations in PZT active suspensions.

In Figure 2.9, w , l , and ρ are the width, length, and thickness of the PZT elements, respectively. λ , σ , and h are the distances from x -axis to the middle width of the PZT elements, from x -axis to the springs, and from y -axis to the head, respectively. During the manufacturing process, the two PZT strips are polarized in opposite directions. When the electric field is applied, one strip shrinks in length and the other expands. Consequently, the PZT active suspension rotates by angle θ for the head displacement of δ by reaction forces F from the springs, as illustrated in Figure 2.10.

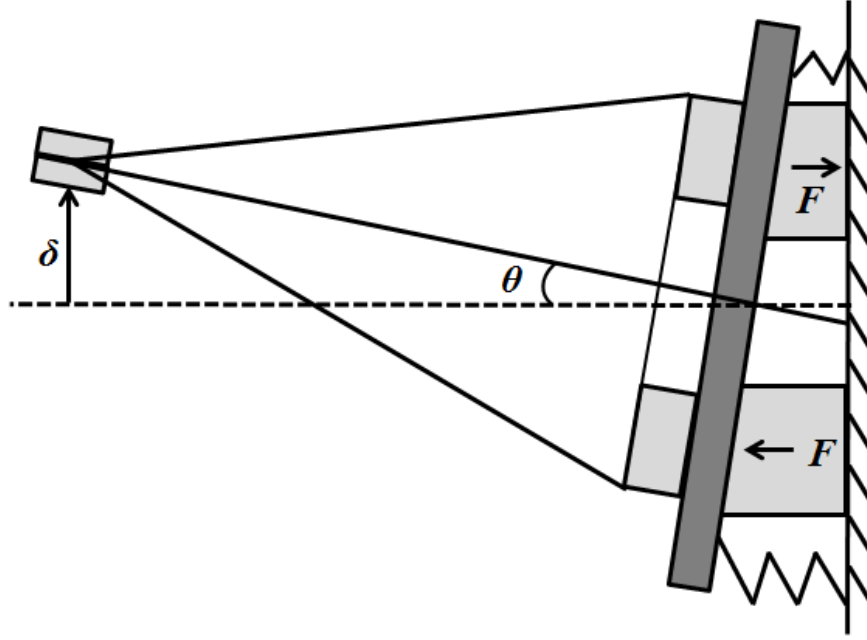


Figure 2.10: Off-track displacement due to deformation of PZT elements.

With reference to Figure 2.10, the dynamics of the suspension can be approximately described as

$$J\ddot{\theta} + 2k\sigma^2\theta = 2\lambda F. \quad (2.33)$$

In our applications, the PZT elements operate in one dimensional d_{31} mode. The piezoelectric constitutive relations are given according to [95] as

$$S_1 = s_{11}^E T_1 + d_{31} E_3, \quad (2.34)$$

$$D_3 = d_{31} T_1 + \varepsilon_{33}^T E_3, \quad (2.35)$$

where D_3 , d_{31} , T_1 , ε_{33}^T , and E_3 are the electric displacement, piezoelectric charge constant, stress, relative permittivity, and applied electric field, respectively. Note that axes are identified by numerals rather than letters in piezoelectric relations. The subscripts 1, 2, and 3 correspond to x , y , and z axes herein.

2.3.1 Actuation Sensitivity

Referring to Figures 2.9 and 2.10, it has been derived that [98]

$$\ddot{\delta} + \left(\frac{2k\sigma^2}{J} + \frac{2w\rho\lambda^2}{Js_{11}^E l} \right) \delta = -\frac{2h\lambda wd_{31}}{Js_{11}^E} V_{in}. \quad (2.36)$$

In steady-state, the relationship from δ to V_{in} is given as follows:

$$\frac{\delta}{V_{in}} = -\frac{h\lambda wd_{31}}{s_{11}^E k\sigma^2 l + w\rho\lambda^2}. \quad (2.37)$$

When $V_{in} = 0$, (2.36) can be simplified into

$$\ddot{\delta} + (\omega_p^2 + \omega_a^2) \delta = 0, \quad (2.38)$$

where $\omega_p^2 = \frac{2k\sigma^2}{J}$ and $\omega_a^2 = \frac{2w\rho\lambda^2}{Js_{11}^E l}$. ω_p and ω_a are the passive suspension frequency and active suspension sway frequency, respectively.

The suspension sway frequency ω_n satisfies that $\omega_n^2 = \omega_p^2 + \omega_a^2$. It follows that

$$J = \frac{2w\rho\lambda^2}{s_{11}^E l(\omega_n^2 - \omega_p^2)}, \quad (2.39)$$

$$k = \frac{J\omega_p^2}{2\sigma^2}. \quad (2.40)$$

We describe the actuation sensitivity S_a from δ to V_{in} in lumped parameters as

$$S_a = -\frac{hl}{\rho\lambda} d_{31} \left(1 - \frac{\omega_p^2}{\omega_n^2} \right), \quad (2.41)$$

where the unit of S_a is nm/V and the frequencies of ω_n and ω_p are obtained from finite element analysis.

Physically, S_a describes the stroke capacity of the PZT active suspension. From (2.41), it can be seen that S_a is a function of the geometric amplification, PZT material properties, and suspension dynamics.

2.3.2 Self-Sensing Sensitivity

The mechanical stress and electric field can be obtained from $T_1 = F/w\rho$ and $E_3 = V_{in}/\rho$, respectively. It follows that

$$D_3 = \frac{d_{31}}{w\rho} \left(\frac{J\ddot{\delta}}{2\lambda h} + \frac{k\sigma^2\delta}{\lambda h} \right) + \varepsilon_{33}^T \frac{V_{in}}{\rho}. \quad (2.42)$$

Electric charge across PZT elements can be obtained by calculating the surface integral of the function D_3 defined on a bounded surface as

$$Q = \iint_{\Phi} D_3 d\Phi = \frac{d_{31}l}{\rho} \left(\frac{J\ddot{\delta}}{2\lambda h} + \frac{k\sigma^2\delta}{\lambda h} \right) + \varepsilon_{33}^T \frac{wl}{\rho} V_{in}, \quad (2.43)$$

where Φ is the surface perpendicular to E_3 and the area of $\Phi = wl$.

Since the two faces of PZT elements are coated with thin electrode layers, the capacitance can be determined from $C_p = \varepsilon_{33}^T wl/\rho$ [99].

The voltage V_p as the difference between the measure voltage and V_{in} can be derived as

$$V_p = \frac{d_{31}J}{2\lambda h\varepsilon_{33}^T w} \left(\ddot{\delta} + \frac{2k\sigma^2}{J}\delta \right). \quad (2.44)$$

In steady-state, the relationship from V_p to δ is given as

$$\frac{V_p}{\delta} = \frac{d_{31}k\sigma^2}{\lambda h\varepsilon_{33}^T w}. \quad (2.45)$$

We describe the self-sensing sensitivity S_s from V_p to δ in lumped parameters as

$$S_s = \frac{\rho\lambda}{hl} \frac{d_{31}}{\varepsilon_{11}^E \varepsilon_{33}^T} \left(\frac{\omega_p^2}{\omega_n^2 - \omega_p^2} \right), \quad (2.46)$$

where the unit of S_s is mV/nm.

Remark 2.1 *It is worth noting that the concepts of S_a and S_s apply to general piezoelectric-actuated systems. The expressions can be similarly derived with the results in (2.41) and (2.46) modified accordingly.*

Remark 2.2 *The expressions of (2.33) can include first order damping term, which is generally quantified from experimental data.*

2.3.3 Trade-offs in Physical Dimensions and Properties

To reveal the trade-offs between S_a and S_s , the results of sensitivity in PZT active suspension are summarized in Table 2.2.

Table 2.2: Summary of actuation and self-sensing sensitivity

	S_a	S_s
Lumped	$-\frac{hl}{\rho\lambda}d_{31}\left(1 - \frac{\omega_p^2}{\omega_n^2}\right)$	$\frac{\rho\lambda}{hl}\frac{d_{31}}{s_{11}^E\varepsilon_{33}^T}\left(\frac{\omega_p^2}{\omega_n^2 - \omega_p^2}\right)$
Modeled	$\frac{-h\lambda w d_{31}}{s_{11}^E k b^2 l + w\rho\lambda^2}$	$\frac{d_{31} k b^2}{\lambda h \varepsilon_{33}^T w}$

Based on Table 2.2, we can reach the following design considerations of PZT active suspensions:

- S_a increases while S_s decreases with greater geometric amplification factor as described by $hl/\rho\lambda$.
- Both S_a and S_s increase with larger d_{31} . S_s increases but S_a decreases with smaller ε_{33}^T .
- Larger S_a or stroke is achieved with smaller ratio of ω_p over ω_n . When $\omega_p \ll$

ω_n , S_a is obtained close to its maximum value at $-d_{31}hl/\rho\lambda$. In this case, V_p is insensible as $S_s \approx 0$.

Remark 2.3 *When the maximum value of S_a is reached, the PZT active suspension will be broken into two parts at where PZT elements sit. In manufacturing process, S_s can serve as a diagnosis tool for this type of manufacturing failure.*

2.4 Summary

In this chapter, two high-performance SSA circuit topologies, *i.e.*, EIDSSA and AIDSSA, are proposed. Both circuit topologies are able to remove the coupling effect between actuation and self-sensing for independent design of each function. The AIDSSA circuit topology further extends the self-sensing capability to the entire frequency spectrum and simplifies the decoupling conditions. Sensitivity analysis in piezoelectric-actuated systems is performed using an example of the PZT active suspension in commercial dual-stage HDDs. The sensitivity reveals the design trade-offs in terms of physical dimensions and properties.

The next chapter reports a scheme of earliest switch-on of dual-stage actuation during track-settling, in which saturation boundary of secondary actuators are calculated. The switch-on conditions with and without SSA will be briefly discussed. The incorporation and integration of the proposed circuits are presented and evaluated in Chapter 4 and Chapter 5.

Chapter 3

Earliest Switch-on of Dual-Stage Actuation

In conventional track-settling process, Pb-Zr-Ti (PZT) actuators are not activated until the read/write heads are in close proximity to the target track so that chances of saturation are reduced. In this chapter, we propose the earliest switch-on scheme based on the calculation of exact saturation boundary, considering both Position Error Signal (PES) and Voice Coil Motor (VCM) velocity error. With the proposed scheme, the PZT control loop can be switched on earlier than current practices with secondary actuators unsaturated. Simulations on a 2.5 inch commercially available Hard Disk Drive (HDD) show that the proposed scheme can reduce the post-seek oscillations and shorten the 5%-track settling time by more than 16% in the presence of in-drive disturbances and measurement noises.

3.1 Background

In Hard Disk Drives (HDDs), the head-positioning system is required to achieve rapid head movement from one track to another in track-seeking, swift transition with less post-seek oscillations in track-settling, and accurate regulation to target track center

in track-following. Higher servo bandwidth is identified as the most direct solution to meet the requirements [100] and it is realized by using the configuration of dual-stage actuation for fine head-positioning.

From a track-following viewpoint, dual-stage servo can significantly improve the head-positioning performance and research efforts have been devoted to study the control structure and controller synthesis [101–105]. As for the track-seeking operation, it is predominately performed in single-stage actuation by Voice Coil Motor (VCM) actuator with Proximate Time Optimal Servomechanism (PTOS) [21]. Pb-Zr-Ti (PZT) control loop is deactivated during the track-seeking, because large Position Error Signal (PES) and velocity tend to saturate the secondary actuators. With regard to the track-settling operation, the PZT control loop is conventionally switched on only when the read/write head is in close proximity to the target track [23]. In practice, servo engineers will choose a late enough switch-on point to guarantee an unsaturated PZT loop based on solely PES information. This conservative approach will inevitably result in an excessive settling time due to PZT control loop being underutilized. On the other hand, if saturation occurs, anti-windup schemes [106, 107] will be activated to retain stability and performance in the track-settling.

Concerning the switch-on strategy of dual-stage actuation, no optimal switch-on conditions have been studied for improved settling time and unsaturated secondary actuators in public literature to the best knowledge of the authors. To this end, the earliest switch-on scheme is proposed in this chapter for smooth and fast track-settling in dual-stage HDDs [108]. Unlike the conventional PES-based method, the proposed

scheme determines the switch-on points based on both PES and VCM velocity error using maximal output admissible set theory. An implementable algorithm is also presented followed by the design procedures. The proposed scheme has been evaluated and emulated in a simulation environment, where realistic plant models, operational conditions, and disturbances are used.

3.2 State-Space Representation

In this section, we present the dynamic modeling of the dual-stage servo system under the saturation constraint. The problem of finding the optimal switch-on conditions in the track-settling process is formulated in state-space representation.

3.2.1 Dynamic Modeling of Dual-Stage Servo Systems

A block diagram of a dual-stage servo system is presented in Figure 3.1.

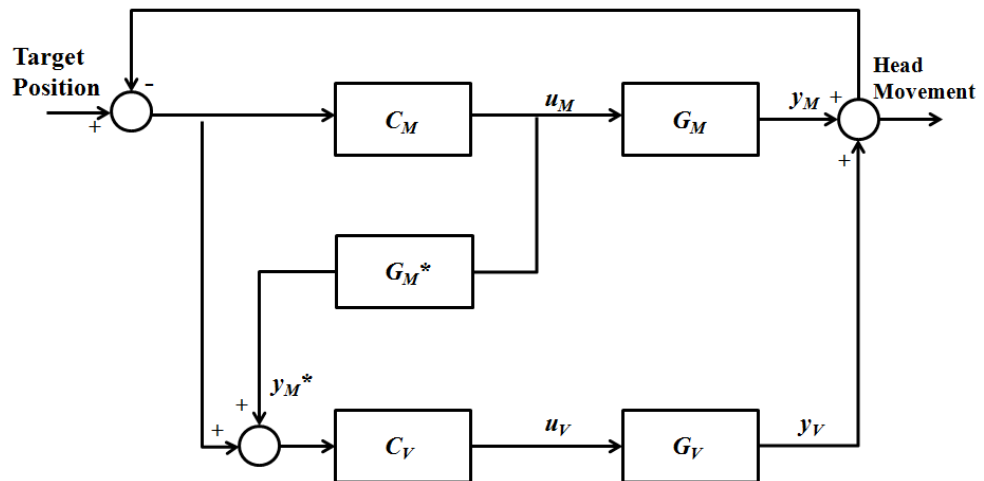


Figure 3.1: The DMS servo control structure in HDDs.

In this work, the Decoupled Master Slave (DMS) servo is chosen to study the switch-on conditions of secondary actuators under saturation constraint as it is widely used in commercial HDD products.

Denote VCM actuator as $G_V(z) : \{A_{PV}, B_{PV}, C_{PV}, D_{PV}, D_{PV} = 0\}$, VCM controller as $C_V(z) : \{A_{CV}, B_{CV}, C_{CV}, D_{CV}\}$ with the state vectors x_{PV} , and x_{CV} , respectively. Denote PZT actuators as $G_M(z) : \{A_{PM}, B_{PM}, C_{PM}, D_{PM}, D_{PM} = 0\}$ and PZT controller as $C_M(z) : \{A_{CM}, B_{CM}, C_{CM}, D_{CM}\}$ with the state vectors x_{PM} and x_{CM} , respectively. A_{PV} , B_{PV} , C_{PV} , D_{PV} , A_{CV} , B_{CV} , C_{CV} , D_{CV} , A_{PM} , B_{PM} , C_{PM} , D_{PM} , A_{CM} , B_{CM} , C_{CM} , and D_{CM} are real matrices in appropriate dimensions.

Referring to Figure 3.1, the DMS servo can be modeled as a discrete-time LTI autonomous system through Zero-Order Hold (ZOH) as described in (3.1), if a matching of PZT predictor $G_M^*(z)$ to the actual plant $G_M(z)$ in frequency domain is assumed.

$$\begin{cases} x(k+1) = Ax(k) \\ y(k) = Cx(k), \end{cases} \quad (3.1)$$

where

$$\begin{aligned} x(k) &= \begin{bmatrix} x_{PV}^T(k) & x_{CV}^T(k) & x_{PM}^T(k) & x_{CM}^T(k) \end{bmatrix}^T, \\ y(k) &= \begin{bmatrix} y_V(k) & u_V(k) & y_M(k) & u_M(k) \end{bmatrix}^T, \\ A &= \begin{bmatrix} A_{PV} - B_{PV}D_{CV}C_{PV} & B_{PV}C_{CV} & 0 & 0 \\ -B_{CV}C_{PV} & A_{CV} & 0 & 0 \\ -B_{PM}D_{CM}C_{PV} & 0 & A_{PM} - B_{PM}D_{CM}C_{PM} & B_{PM}C_{CM} \\ -B_{CM}C_{PV} & 0 & -B_{CM}C_{PM} & A_{CM} \end{bmatrix}, \end{aligned}$$

and

$$C = \begin{bmatrix} C_{PV} & 0 & 0 & 0 \\ -D_{CV}C_{PV} & C_{PV} & 0 & 0 \\ 0 & 0 & C_{PM} & 0 \\ -D_{CM}C_{PV} & 0 & -D_{CM}C_{PM} & C_{CM} \end{bmatrix}.$$

In real-world situations, the mismatch between the PZT predictor $G_M^*(z)$ and the actual plant $G_M(z)$ is inevitable, though perfectly decoupled sensitivity exists in theory. However, it can be verified easily that even for reduced-order PZT actuated suspension with parameter uncertainty, y_M^* is still a close estimation of y_M [104]. Note that the VCM actuator is required to be realized in controllable canonical form so that the physical meaning of closed-loop states such as position and velocity can be assigned properly.

3.2.2 Saturation of Secondary Actuators

The saturation of PZT actuators $G_M(z)$ is essentially a constraint existing in dual-stage controller design. Consider the output vector $y(k) \in \mathbb{R}^4$ as the signal to be constrained. With unsaturated secondary actuators, the control signal u_M is required to satisfy $u_M(k) \in [-\delta, \delta]$, where $\delta \in \mathbb{R}^+$. Let Y be a convex polyhedral set containing the constrained signals as follows:

$$Y = \{y(k) \mid Qy(k) \leq q\delta, y(k) = CA^k x(0)\}, \quad (3.2)$$

$$\text{where } Q = \begin{bmatrix} 0 & 0 & 0 & -1 \\ 0 & 0 & 0 & 1 \end{bmatrix} \text{ and } q = [1 \ 1]^T.$$

3.2.3 Switch-on Conditions of Secondary Actuators

Referring to Figure 3.2, *premature* switch-on happens if the PZT control loop is activated too early during the track-settling, where the initial position and velocity of VCM actuator cause large transient that saturates secondary actuators. The conventional approach dealing with the situation is to enable secondary actuators only when the position error is confined to a very small range. *Late* switch-on is in place to reduce chances of saturation. However, it prolongs the settling time unnecessarily. According to our data on a commercial 2.5 inch HDD, only half range of PZT control signal is utilized during the track-settling. Excessive headroom to saturation means that the configuration of dual-stage actuation is not employed efficiently. As such, *earliest* switch-on is desired for faster and smoother track-settling while secondary actuators remain unsaturated.

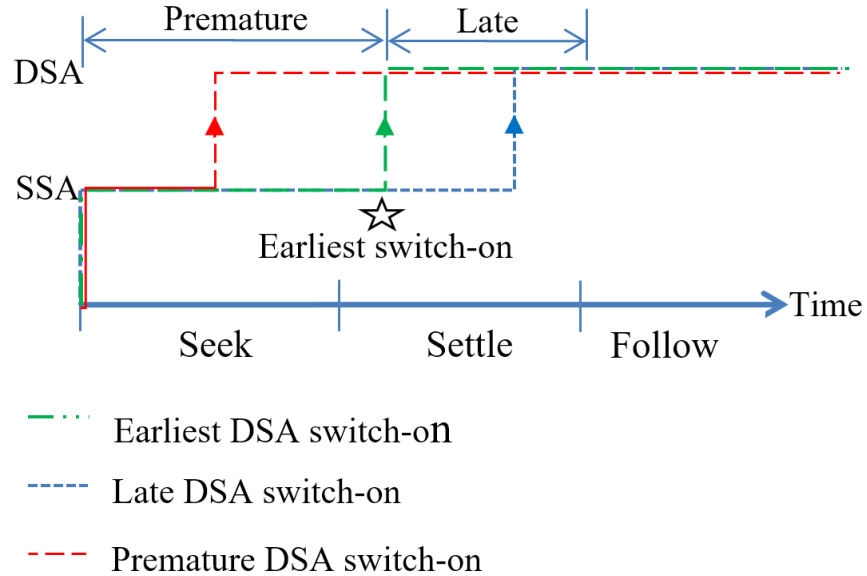


Figure 3.2: Switch-on of PZT actuators.

3.3 Proposed Earliest Switch-on Scheme

In this section, we propose the earliest switch-on scheme in the track-settling process. Based on the theory of maximum output admissible set, an implementable *algorithm* is designed to calculate the feasible region O_∞ under the saturation constraint. Design procedures to apply the earliest switch-on scheme are detailed.

3.3.1 Maximum Output Admissible Set

The theory of maximum output admissible set is a useful tool in handling state and control constraints in linear and non-linear systems. A maximum output admissible set consists of all closed-loop initial states that satisfy the system constraints, such as the one described in (3.2) in our application.

Let O_m be the output admissible set up to step m , that is $O_m = \{x(0) \mid y(k) = CA^k x(0) \in Y, \forall k \leq m\}$. It holds that $O_m = X_1 \cap X_2 \cap \dots \cap X_m$, where X_i is the output admissible set at discrete step i . It follows that $O_{m+1} = O_m \cap X_{m+1}$. The maximum output admissible set O_∞ is defined as,

$$O_\infty = \{x(0) \mid y(k) = CA^k x(0) \in Y, \forall k \in \mathbb{Z}^+\}. \quad (3.3)$$

It is notable that,

1. for discrete time step $m_1, m_2 \in \mathbb{Z}^+$, and $m_1 \leq m_2$, we have $O_\infty \subseteq O_{m_2} \subseteq O_{m_1}$;
2. if O_∞ is finitely determined and p_0 is the smallest p such that $O_p = O_{p+1}$, then $O_\infty = O_{p_0} = O_p$, for any $p \geq p_0$;
3. O_∞ is a convex polyhedral set.

To facilitate the design of earliest switch-on scheme, the following results of O_∞ are introduced [109].

Property 1 O_∞ is finitely determined if there exists an integer $p \in \mathbb{Z}^+$, such that $O_p = O_{p+1}$ and O_p is non-empty.

Property 2 For a discrete-time Linear Time-Invariant (LTI) system characterized by (A, C) , O_∞ can be finitely determined under the constraint Y if below conditions are met:

1. Eigenvalues of A are within a unit circle with center at the origin on z -plane,
2. Y is bounded and $0 \in \text{interior}(Y)$,
3. $\Omega^T = [C^T, A^T C^T, \dots, (A^T)^{n-1} C^T]$ is full rank.

Finite determinability of O_∞ is evaluated to ensure that O_∞ is feasible. The feasible region of O_∞ represents the conditions that secondary actuators can be switched on without violating the saturation constraint as described in (3.2). *Property 1* renders a termination criteria for algorithmic calculation of O_∞ .

Next, we propose an implementable *algorithm* to calculate the feasible region O_∞ under the saturation constraint. The saturation boundary is delineated on the phase-plane with its coordinates representing PES and VCM velocity error.

3.3.2 Algorithm to Determine Saturation-Free Region

According to *Property 1*, the algorithm to determine saturation free region O_∞ can be immediately designed based on the termination criteria $O_p = O_{p+1}$. However, it is

impractical to compare the sets O_p and O_{p+1} in our applications. An implementable algorithm for indirectly evaluating the termination criteria is required. This can be achieved by introducing an equivalent form of the saturation constraint as presented in (3.2). The equivalent form is defined as

$$Y = \{y(k) \mid \mu(CA^k x(0)) \leq 0\}, \quad (3.4)$$

where $\mu : \mathbb{R}^4 \rightarrow \mathbb{R}^2$ is a given vector function. It is notable that the selection of $\mu(\cdot)$ is not unique. For our application, we have chosen $\mu(CA^k x(0))$ to be $QCA^k x(0) - q\delta$, where Q , q and δ follow the definitions in (3.2).

The set O_m is defined equivalently as

$$O_m = \{x(0) \mid \mu(CA^k x(0)) \leq 0, \forall k \leq m\}. \quad (3.5)$$

Further,

$$O_{m+1} = \{x(0) \in O_m \mid \mu(CA^{m+1} x(0)) \leq 0\}. \quad (3.6)$$

Since $O_{m+1} \subseteq O_m$, the criteria $O_p = O_{p+1}$ is equivalent to

$$\begin{aligned} x(0) \in O_p \text{ and } \mu(CA^{p+1} x(0)) &\leq 0 \\ \Leftrightarrow \sup_{x(0) \in O_p} \mu(CA^{p+1} x(0)) &\leq 0. \end{aligned}$$

As O_∞ is a convex polyhedral set, mathematical programming techniques, such as corner-point method [110], can be applied to determine the maximum value of $\mu(CA^{k+1} x(0))$.

The algorithm to determine the saturation-free region O_∞ is presented in *Algorithm 1*. The algorithm determines the saturation-free region O_∞ recursively

in lieu of direct evaluation of $O_p = O_{p+1}$. The program will terminate when the maximum value of J , namely J^* , becomes non-positive.

Algorithm 1

Require: $\text{eig}(A) \leq 1$ AND $\text{length}(A) - \text{rank}(\text{obsv}(A, C)) = 0$.

```

1: Set  $k = 1$ 

2: while  $J^* \geq 0$  do

3:   for do  $i = 1, 2, \dots, k$ 

4:     Calculate output admissible set at step  $i$ ,  $X_i$ 

5:   end for

6:   Determine  $O_k = X_1 \cap X_2 \cap \dots \cap X_k$ 

7:   Create a set of corners  $V_k$ 

8:   for all corners in  $V_k$  do

9:      $J = \mu(CA^{k+1}x(0))$ 

10:  end for

11:  Set  $J^* = \max_{x(0) \in O_k} \mu(CA^{k+1}x(0))$ 

12:   $k++$ 

13: end while

14: return  $O_k = O_\infty$ .
```

Ensure: O_∞ is non-empty.

3.3.3 Design Procedures

The steps to apply the proposed earliest switch-on scheme are presented in Figure 3.3.

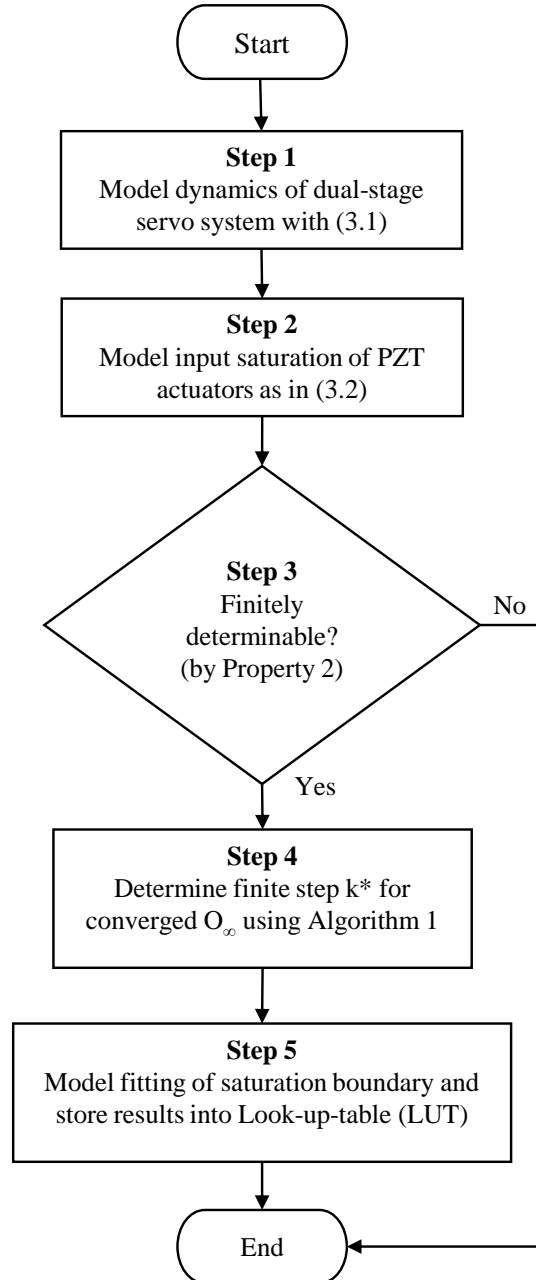


Figure 3.3: Generation of LUT for the earliest switch-on.

With reference to Figure 3.3, the steps to apply the proposed earliest switch-on scheme are as follows:

Step 1: Design controllers $C_V(z)$ and $C_M(z)$ for the dual-stage servo control system using decoupled design or any other prevalent method. Notch filters could be applied to handling the important resonances. For a DMS servo, dynamics of overall dual-stage control system can be modeled in state space with (3.1). It is notable that the VCM actuator is required to be realized in controllable canonical form.

Step 2: Consider the input saturation constraint for the secondary actuators as $u_M(k) \in [-\delta, \delta]$. Model the saturation constraint of secondary actuators with (3.2).

Step 3: Evaluate the finite determinability by *Property 2*. If it is finitely determinable, proceed to the next step; else, earliest switch-on is infeasible.

Step 4: Determine the finite step $k^* = p_0$ for a converged result O_∞ by *Algorithm 1*. Mathematical programming technique is applied in this step to evaluate the termination condition.

Step 5: Perform model fitting of the saturation boundary and store the results into a Look-Up-Table (LUT). To reduce the computational load, LUT can be generated by off-line processing.

When the track-settling process starts, PES and VCM velocity error from the state observer are validated against the generated LUT in real-time. The PZT control loop is activated when the earliest switch-on conditions defined in LUT are satisfied.

3.4 Simulation Results and Discussions

In this section, the effectiveness of the earliest switch-on scheme is validated with simulations. Suppose that the VCM actuator is compensated with notch filters and the compensated model $G_V(z)$ is approximated by a double integrator at frequencies of interest. Secondary actuators $G_M(z)$ are modeled as pure gain coupled with several compensated mechanical modes. The discretization of plant model is done by ZOH at the sampling frequency of 25 kHz. The VCM controller $C_V(z)$ is designed as a standard lead-lag controller in series with an integrator,

$$C_V(z) = \frac{0.2731(z - 0.994)(z - 0.9927)}{(z - 1)(z - 0.7778)(z - 0.6605)}. \quad (3.7)$$

The PZT controller $C_M(z)$ is a lag compensator as follows,

$$C_M(z) = \frac{0.7231z + 0.5898}{z - 0.9274}. \quad (3.8)$$

All transfer functions are realized in state space models. The overall dual-stage servo system is an autonomous system as described in (3.1). Transfer functions of plant models $G_V(z)$ and $G_M(z)$ are omitted here due to confidentiality but without loss of generality. Disturbances and noises in the simulations are obtained from industrial data in order to ensure the practicality of the simulation results.

For the purpose of simulation, the earliest switch-on scheme is tested as compared to premature and late switch-on schemes. In the simulations, other advanced servo features affecting the settling performance is disabled to study the effectiveness of the proposed scheme. Let $u_M \in [-20 \text{ V}, 20 \text{ V}]$ be the permissible range of the input signal to secondary actuators $G_M(z)$. *Property 2* is evaluated to ensure that the dual-

stage servo system is asymptotically stable and observable. *Algorithm 1* is applied to converge the O_∞ at finite step $k^* = 61$. The feasible solution of O_∞ , saturation-free region, is delineated in Figure 3.4.

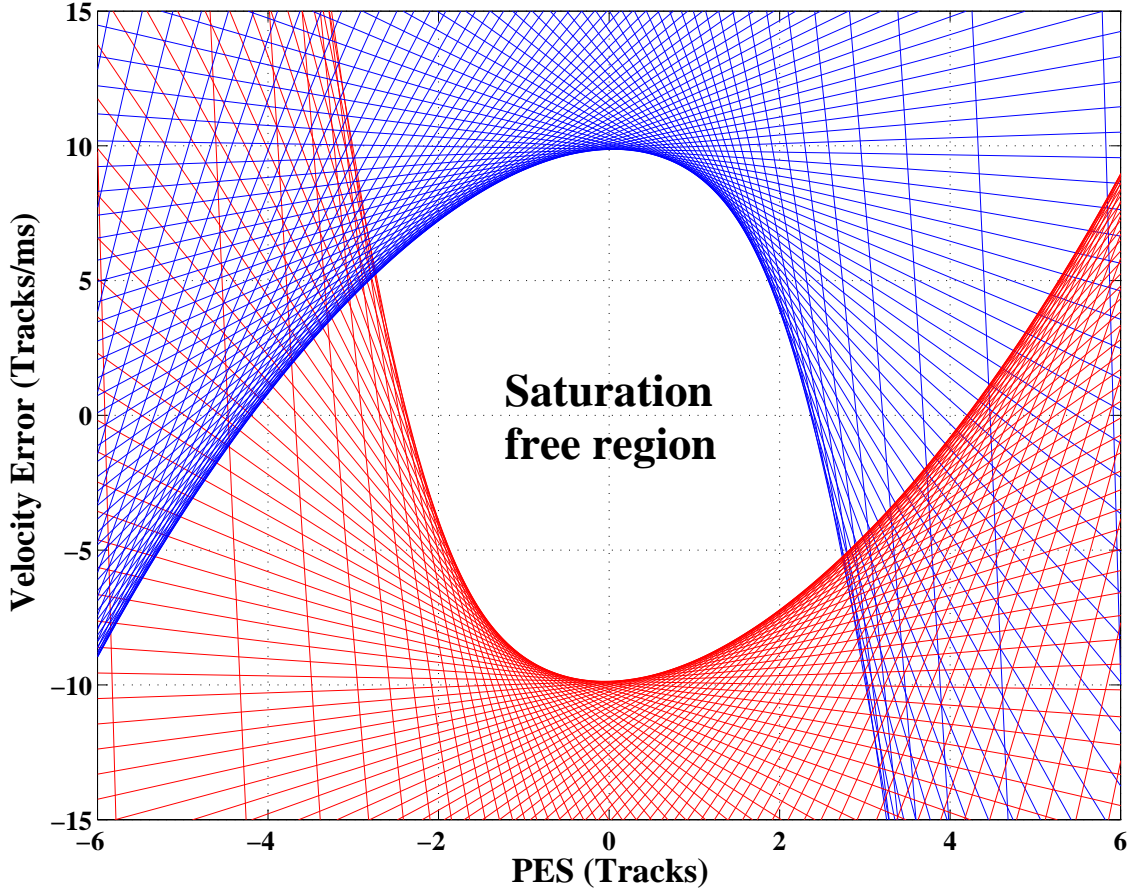


Figure 3.4: Feasible solution of O_∞ with $u_M \in [-20 \text{ V}, 20 \text{ V}]$.

In Figure 3.4, the saturation boundary constitutes the set of earliest switch-on conditions. Activation of PZT control loop inside the boundary prolongs the settling unnecessarily, whereas activation outside the boundary saturates the secondary actuators $G_M(z)$.

Phase-plane analysis of different switch-on conditions is shown in Figure 3.5.

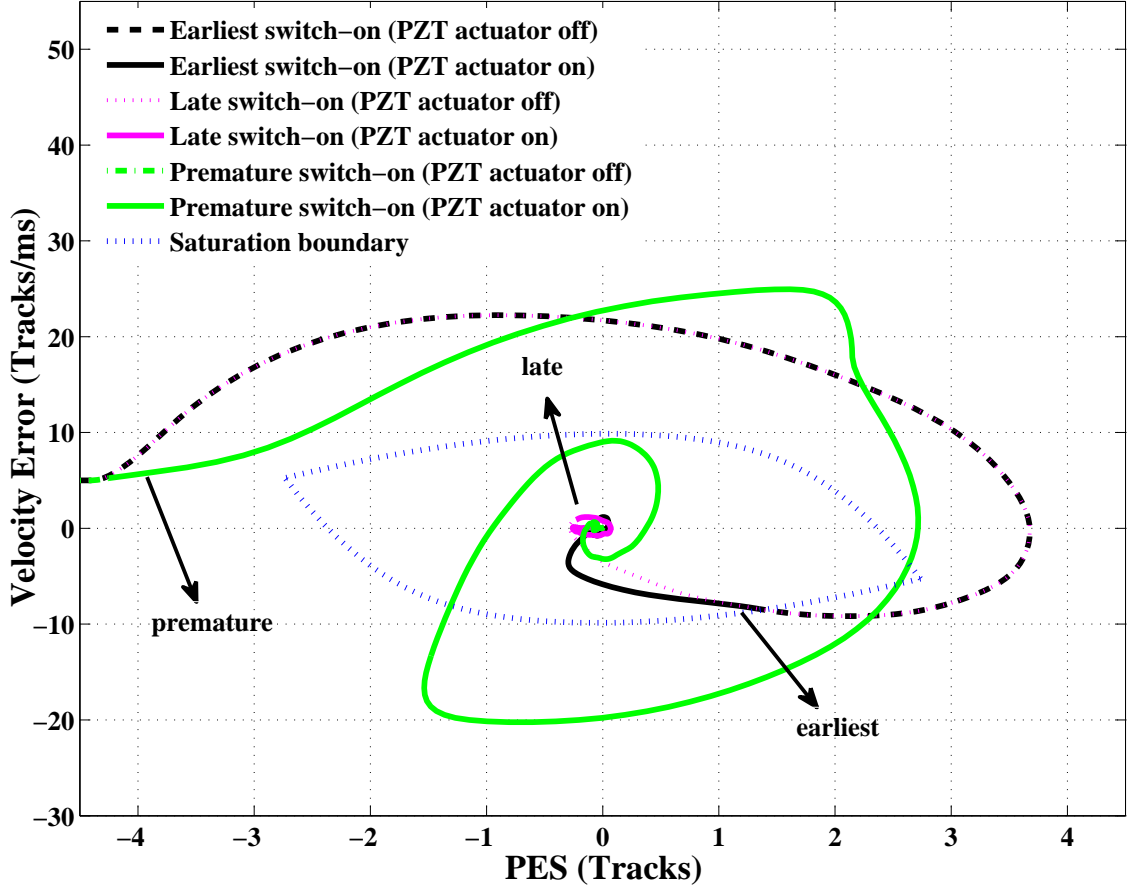


Figure 3.5: Phase-plane analysis for the earliest switch-on.

Based on Figure 3.5, when the secondary actuators are prematurely activated with the initial PES and VCM velocity error outside the calculated saturation boundary, there are obvious oscillations shown on the phase-plane with large overshoot. Should the switch-on occurs earlier, the dual-stage servo could even become unstable. Although the late switch-on does not cause oscillations, it settles slower with larger overshoot. In the time domain, it can be seen from Figure 3.6 that the proposed scheme improves the 5%-track settling time by more than 16%.

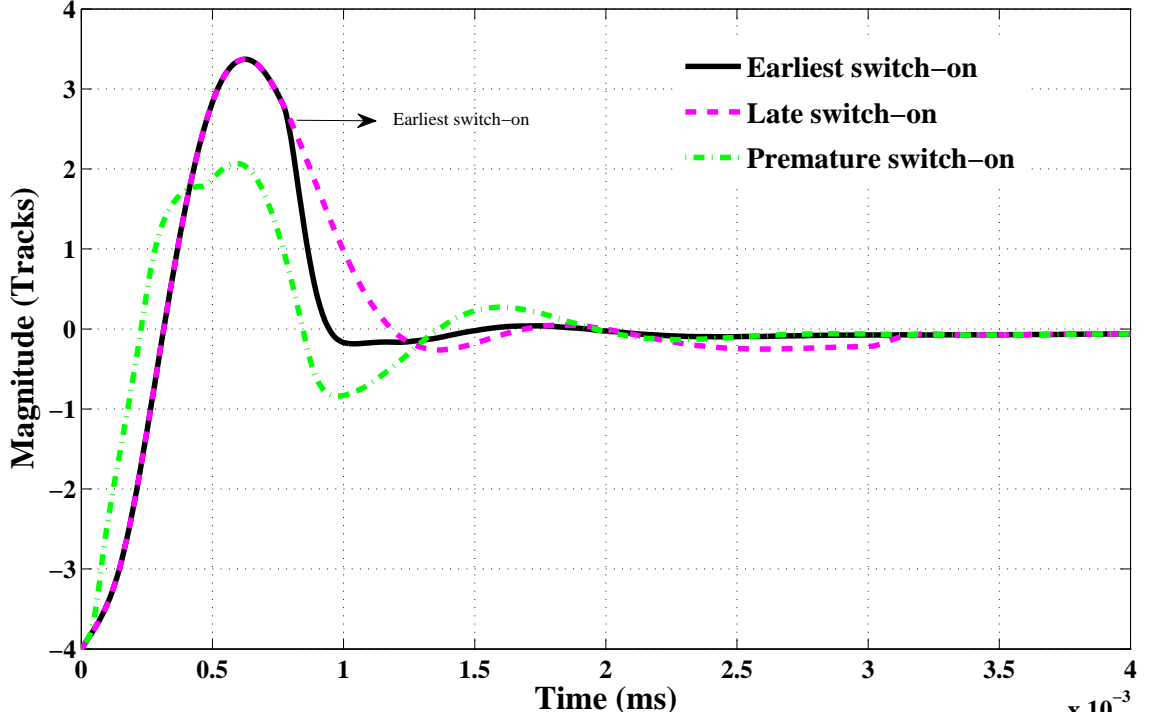


Figure 3.6: PES traces for the earliest switch-on.

The proposed earliest switch-on scheme utilizes the actuation limit more efficiently for faster tracking convergence without saturation via combining the best aspects of the VCM and PZT control loops, as shown by Figure 3.7.

The secondary actuators are activated when the switch-on conditions are met by evaluating the current values of the closed loop states. After the switch-on, the PZT controller $C_M(z)$ effectively utilizes the secondary actuators in unison with the VCM actuator for shorter settling time and lower overshoot than the conventional late switch-on. Furthermore, the premature switch-on causes saturation of secondary actuators during the track-settling, but the earliest switch-on employs more than 80% of the input control signal range. Saturation of secondary actuators caused by the premature switch-on explains the severe oscillations as observed in Figure 3.5.

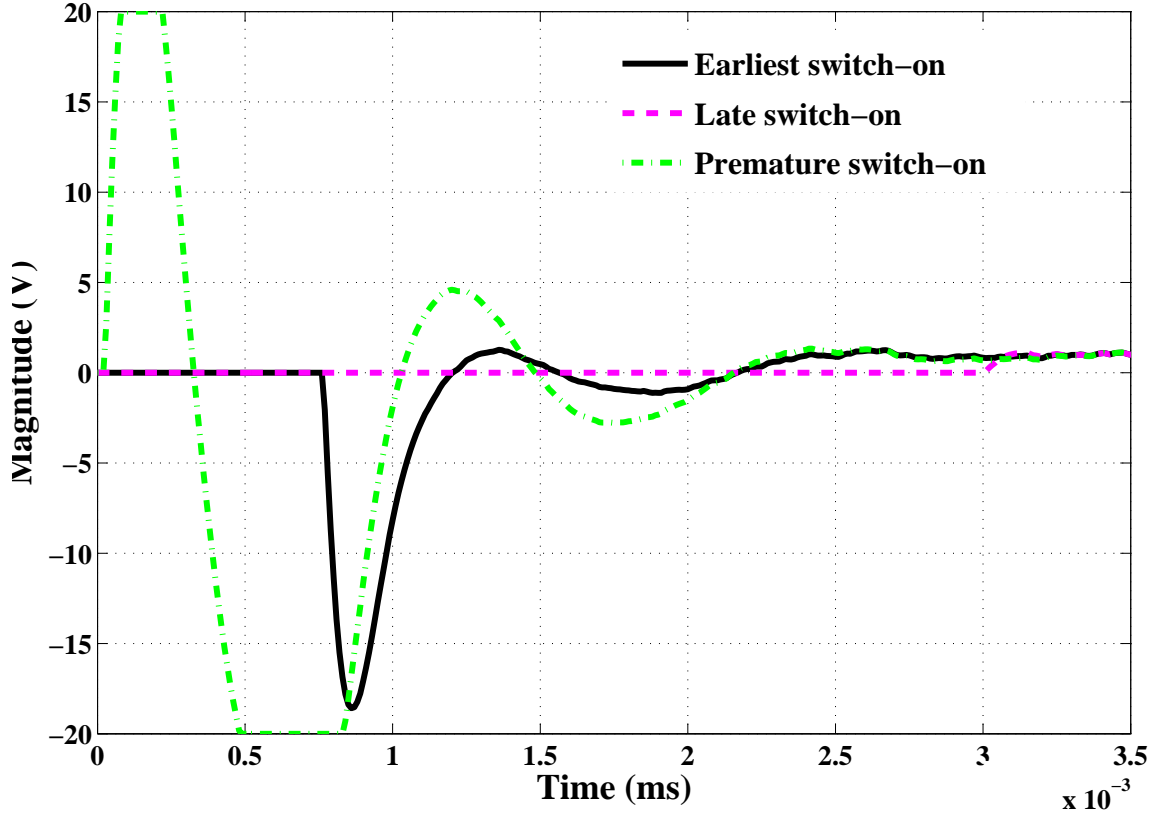


Figure 3.7: Control traces for the earliest switch-on.

Obviously, the late switch-on could have benefited more from the PZT control loop as the PZT control signal has ample headroom to saturation available. The proposed switch-on is earliest while the secondary actuators remain unsaturated. It achieves optimal distribution of control efforts between the VCM and PZT control loops during the track-settling process, with saturation avoided and control objectives achieved.

The benefits of earliest switch-on include not only faster and smoother settling, but also stronger disturbance rejection. According to Figure 3.8, in the presence of in-drive disturbances, such as uncompensated flex cable bias, windage and friction, the proposed scheme achieves superior settling performance. Late switch-on cause large overshoot when in-drive disturbances are applied. Attributed to the extended

bandwidth by the PZT control loop, earliest switch-on attains a lower overshoot and fastest settling.

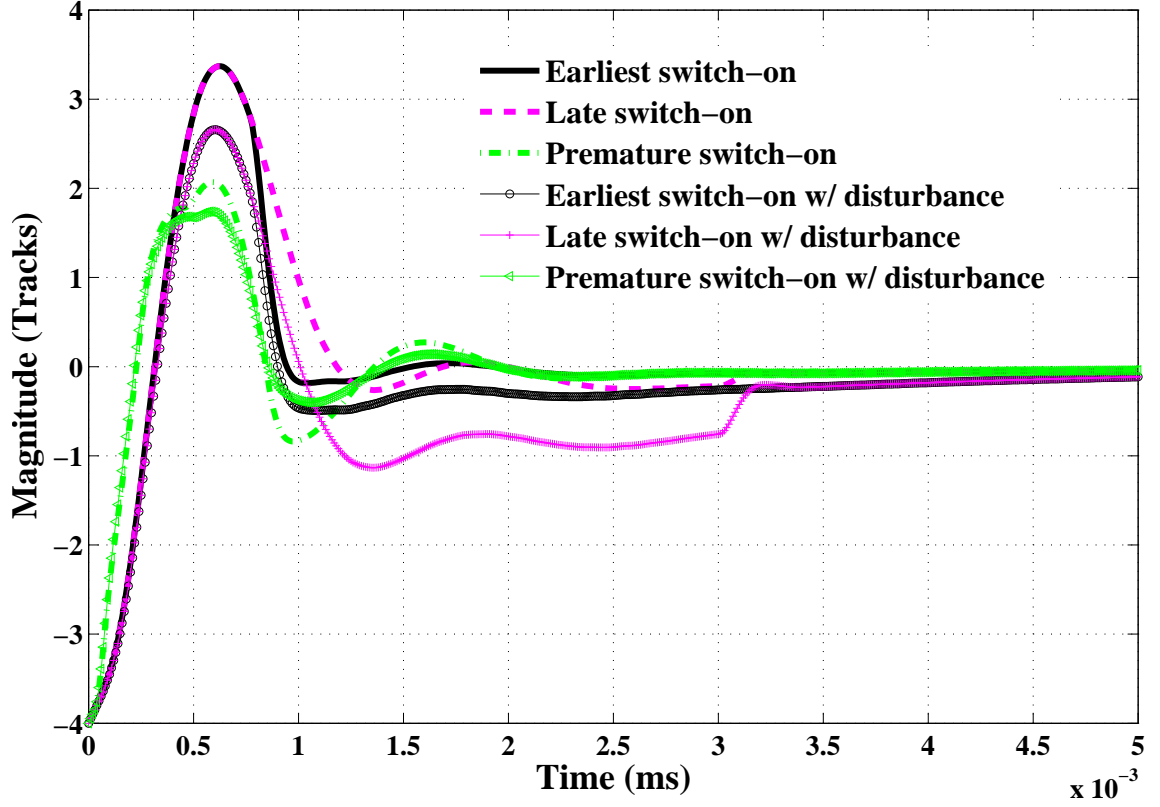


Figure 3.8: PES traces for the earliest switch-on with in-drive disturbances.

It is shown in Figure 3.9 that secondary actuators remain unsaturated. The earliest switch-on achieves less oscillation during settling in the presence of various in-drive disturbances.

It is well-known that changes in environmental factors could affect the modeling accuracy, thus the exactitude of the saturation boundary. In this study, the plant gain drift due to temperature change is considered with the open loop gain maintained. Figure 3.10 illustrates the boundary shift with changed gains.

As presented in Figure 3.10, the saturation boundary will be enlarged/shrunk by

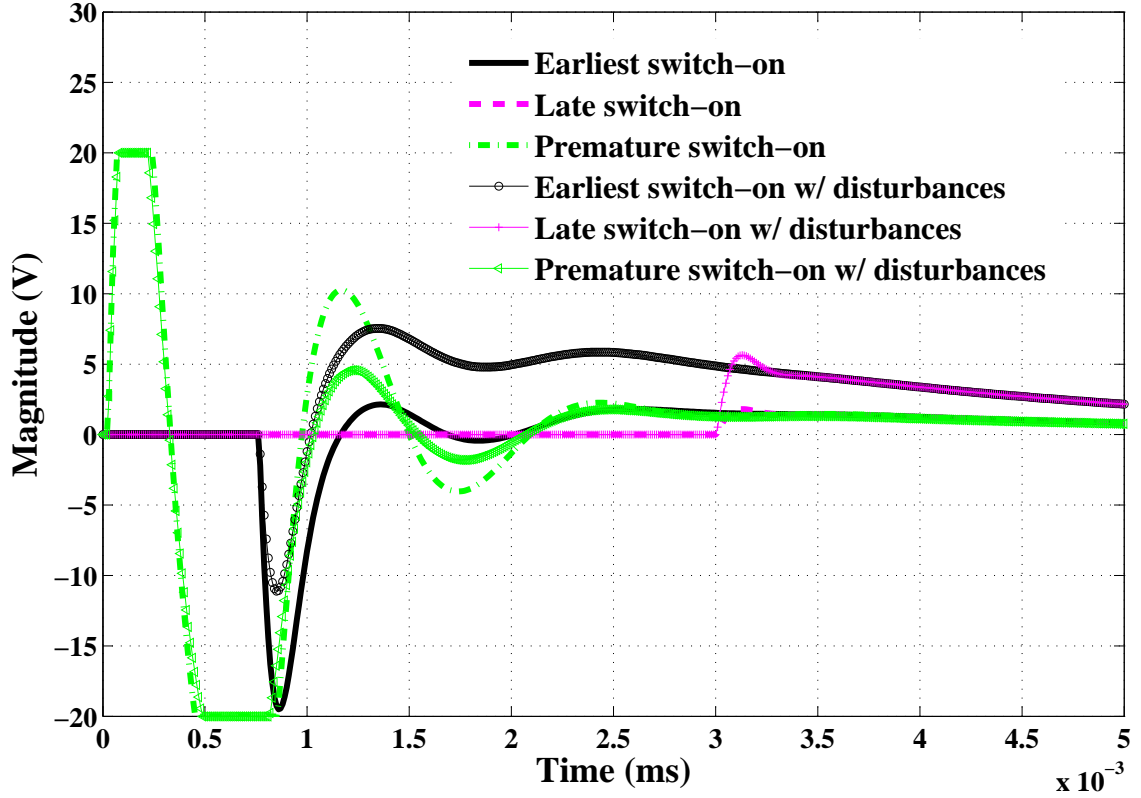


Figure 3.9: Control traces for the earliest switch-on with in-drive disturbances.

a positive/negative gain drift. During implementation, such gain drift effects could be parametrized so that multiple LUTs are stored at firmware level. An LUT is selected automatically in real time to determine the switch-on conditions during the track-settling.

It is worth noting that if self-sensing actuation (SSA) is employed in the dual-stage servo, further improvement of 5–% settling time can be expected. This is attributed to the higher servo bandwidth achievable by controller synthesis using the additional feedback signal from SSA.

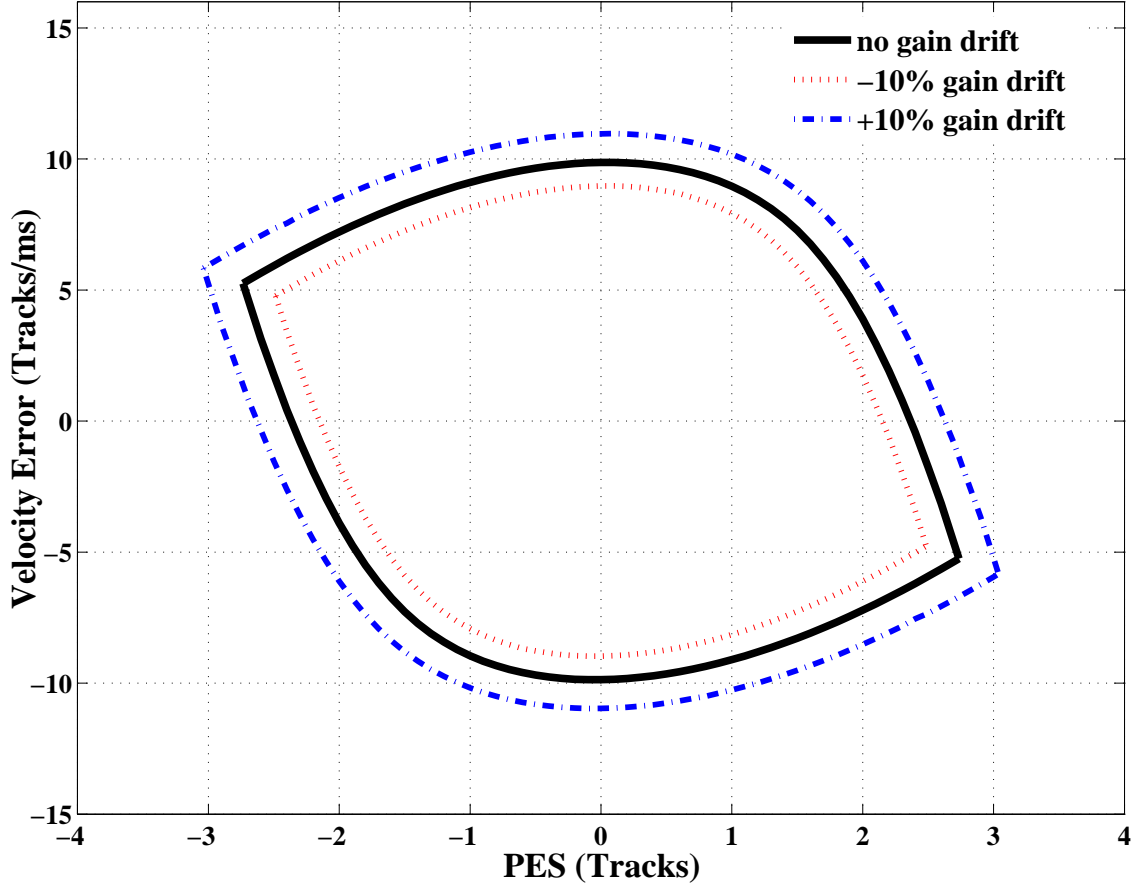


Figure 3.10: Saturation boundary with $\pm 10\%$ PZT plant gain drift.

3.5 Summary

In this chapter, the earliest switch-on scheme of dual-stage actuation during track-settling in HDDs is proposed. Detailed methodology based on maximum output admissible set theory is presented to calculate the saturation boundary of the secondary actuators. Simulation results show that the proposed scheme benefits more from the dual-stage servo and utilizes the range of the control signal more efficiently as compared to conventional methods. The overshoot is lowered with less post-seeking oscillations. The 5%–track settling time is reduced by more than 16%.

In the next chapter, we will detail the incorporation and integration of SSA mechanisms to dual-stage HDD servo systems for higher bandwidth and stronger vibration rejection capability.

Chapter 4

Improved Rejection of Audio-Induced Vibrations

In this chapter, the proposed Enhanced Indirect-Driven Self-Sensing Actuation (EIDSSA) is realized and incorporated into commercial dual-stage Hard Disk Drives (HDDs) to improve the rejection of audio-induced vibrations. Experimental results show that the on-track Total Runout (TRO) has been reduced by 8.89% in pink noise audio-induced vibration and more than 16% in single tone audio-induced vibrations without additional loop tuning efforts.

4.1 Background

In Hard Disk Drives (HDDs), audio-induced vibration is a typical type of external disturbance with strong and wide frequency spectrum. The frequencies of such vibrations could range from a few hundred hertz to several thousand hertz. They are induced by audio sounds from the speakers in personal computers as well as loud noises in data centers. These audio-induced vibrations significantly increase the Position Error Signal (PES), thus contaminate the head-positioning accuracy. Although the high bandwidth provided by dual-stage HDD servos is effective to suppress the

disturbances, but those frequency components in audio-induced vibrations within the sensitivity hump (typically from 2 kHz to 3.5 kHz) are usually amplified. Today, audio-induced vibrations have become one of the most critical challenges for servo control engineers.

Currently, the techniques to deal with audio-induced vibrations include shaping of sensitivity transfer function by adding peak filters [39, 111, 112]. However, peak filters are not very effective to reject vibrations with wide frequency spectrum. In frequency range with significant dynamics, the controller design must be carried out carefully to retain stability. Another technique is to use adaptive compensation to reject multiple narrow-band disturbances [113, 114]. However, adaptive control is relatively complicated to be realized in practical systems, and the rate of convergence must be tuned during implementation. Moreover, the frequency spectrum of audio-induced vibrations differs in products and is time-varying. It is difficult for adaptive algorithm to deal with such dynamic vibrations. There are also many estimation and filtering approaches to deal with vibrations in existing literature [115–117]. Some researchers have developed feed-forward control schemes with extraneous sensors, such as accelerometers, velocity transducers, or shock sensors [44, 45, 118]. Unfortunately, additional sensory devices require extra cost, which is a major concern in the industry. The sensor fusion in HDDs is generally complicated in terms of system development and integration.

In this chapter, the proposed Enhanced Indirect-Driven Self-Sensing Actuation (EIDSSA) is realized and incorporated into a commercially available dual-stage HDD

to improve the rejection of audio-induced vibrations [71]. The conventional Decoupled Master Slave (DMS) servo control structure is modified to include head displacement in-situ estimation by self-sensing mechanism. The implementation is very simple, straightforward and cost-saving. Experimental results show that the proposed method is effective in handling vibration with a wide frequency spectrum.

4.2 Head Displacement In-situ Estimation

The in-situ estimation of head displacement can be achieved by using self-sensing actuation techniques as described in Chapter 2. It should be noted that any high performance self-sensing solutions can be employed, regardless EIDSSA or Asymmetrical Indirect-Driven SSA (AIDSSA). As an example, we use the realization of EIDSSA presented in Figure 2.4 to estimate the in-situ head displacement.

With reference to Figure 2.4, the values of circuit components are tabulated in Table 4.1.

Table 4.1: Values of circuit components for rejection of audio-induced vibrations.

Component	Values
$R_1 = R_2$	1.0 M Ω
$C_3 = C_4$	1.25 nF
$R_5 = R_6$	560 k Ω
$C_p = C_q$	4.7 nF

As $\gamma = 100\%$ for EIDSSA, the actuation is gain lossless with control efforts fully

delivered to Pb-Zr-Ti (PZT) actuators. In the presented EIDSSA realization, β is a transfer function exhibiting high-pass characteristics in the frequency domain. It holds that $\beta = \frac{sR_5C_p}{sR_5C_3 + 1} = \frac{2632s}{700s + 1}$.

4.3 Modified DMS Servo Incorporating EIDSSA

The block diagram of our proposed modified DMS servo incorporating EIDSSA circuit is shown in Figure 4.1.

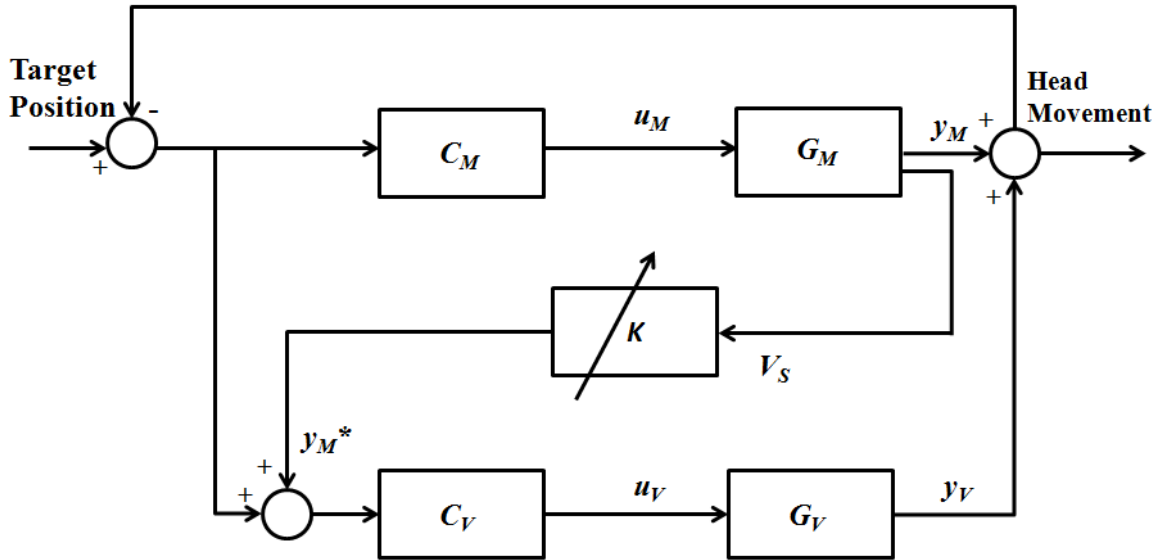


Figure 4.1: Modified DMS servo control structure incorporating EIDSSA.

In Figure 4.1, we denote Voice Coil Motor (VCM) actuator as G_V , VCM controller as C_V , PZT actuator with the proposed EIDSSA circuit as G_M , and PZT controller as C_M . u_M and u_V are PZT and VCM control signals, respectively. y_M and y_V are the head displacements due to deformation of PZT elements and VCM motion,

respectively. Output V_s from EIDSSA circuit is transferred to y_M^* via a gain K which is obtained iteratively by an optimization-based algorithm implemented in firmware. The algorithm to obtain K is not elaborated in this dissertation due to confidentiality. As y_M^* actively decouples servo loops, standard controller design and loop shaping based on decoupled sensitivity can be performed [104].

As compared to the DMS servo in [69], our proposed control structure does not require additional filters $H_B(s)$. The elimination of $H_B(s)$ is because of the excellent common mode rejection of EIDSSA. With in-situ measurement of y_M^* , the loop decoupling in DMS servo can be improved. This is impossible if y_M^* arises from a conventional low-order PZT predictor where high frequency dynamics are ignored.

G_V is compensated by notch filters and approximated by a double integrator at frequencies of our interest. G_M is a pure gain coupled with several compensated mechanical modes at higher frequencies. The transfer functions of G_V and G_M are not presented due to confidentiality. The discretization of G_V and G_M is performed by Zero-Order Hold (ZOH) at the sampling frequency of 40.32 kHz.

The VCM controller $C_V(z)$ is designed as a fourth-order lead-lag controller with an integrator,

$$C_V(z) = \frac{(z - 0.06777)(z + 0.05616)(z^2 - 1.888z + 0.8909)}{(z - 1)(z + 0.065)(z^2 - 0.6085z + 0.2506)}. \quad (4.1)$$

The PZT controller $C_M(z)$ is a lag compensator that can be described as

$$C_M(z) = 0.3813 \frac{(z - 0.4588)(z - 0.5835)}{(z - 0.2204)(z - 0.9324)}. \quad (4.2)$$

The frequency responses of $C_V(z)$ and $C_M(z)$ are depicted in Figures 4.2 and 4.3, respectively.

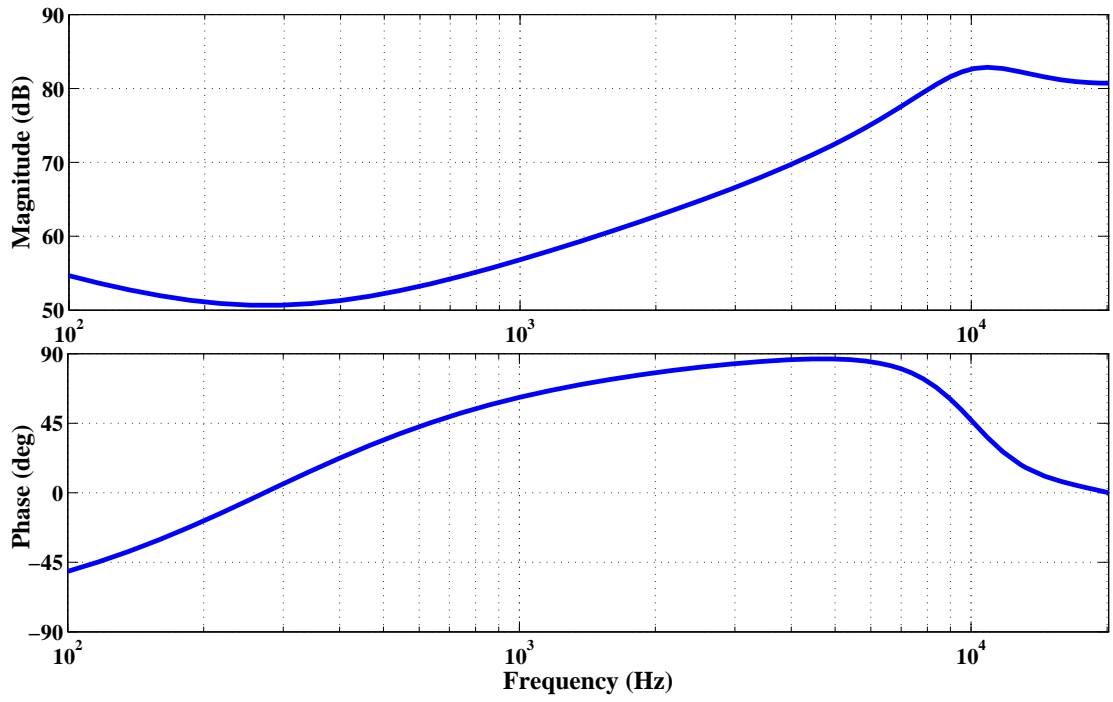


Figure 4.2: Frequency response of VCM controller.

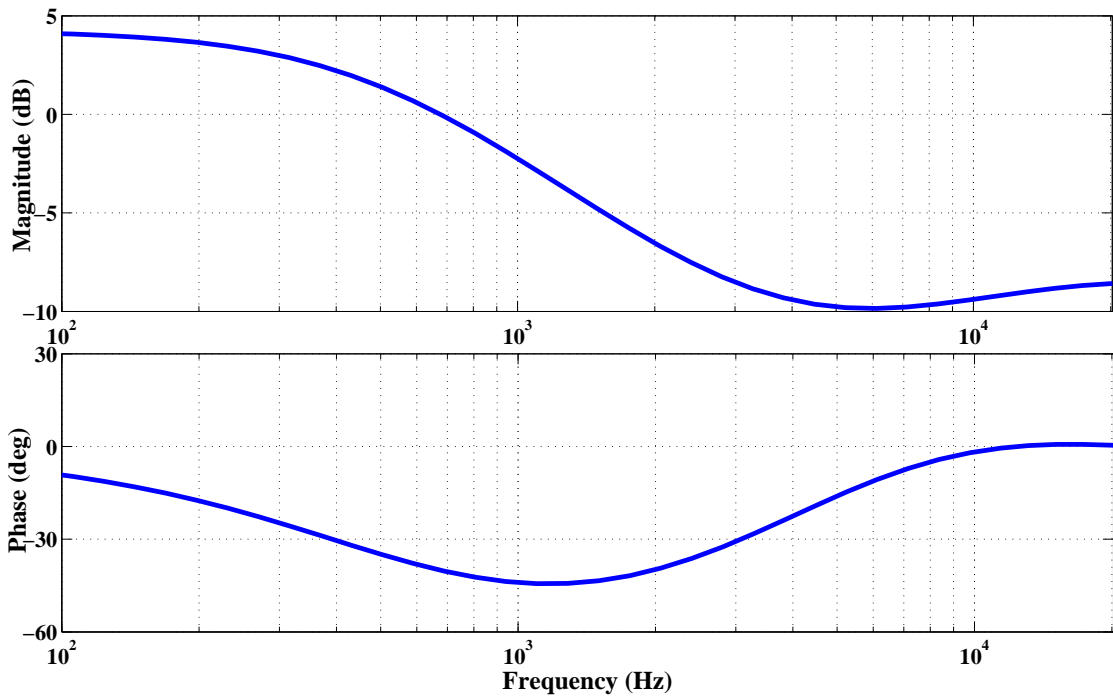


Figure 4.3: Frequency response of PZT controller.

4.4 Experimental Results and Discussions

For demonstration purpose, a commercially available 3.5 inch dual-stage HDD with PZT active suspension is modified to integrate the proposed EIDSSA circuit as shown in Figure 4.4.

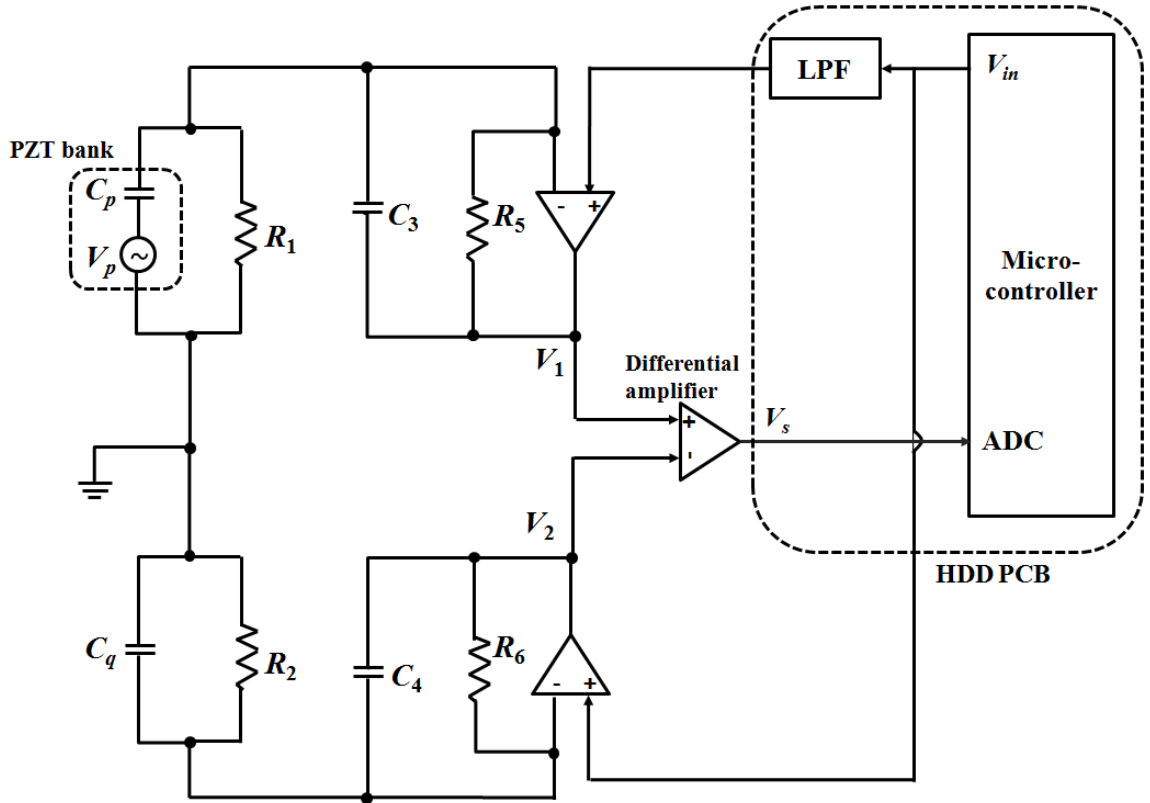


Figure 4.4: Experimental set-up and system integration.

With reference to Figure 4.4, output voltage V_s is routed to the Analog-to-Digital-Converter(ADC) port of micro-controller for sampling. Low-Pass-Filter (LPF) represents a ferrite bead in the Printed Circuit Board (PCB) to suppress unwanted noises at higher frequencies due to electrical circuits. Bank-driving PZT actuators are connected in the upper arm of the proposed EIDSSA to achieve indirect actuation. No

plural of circuits is required for each head.

Actuation sensitivity S_a can be obtained from the slope of PZT stroke measurement. According to our experiments, $S_a = 13.7 \text{ nm/V}$ as V_{in} varies from 1 V to 10 V. The time traces of V_s and V_{in} are plotted in Figure 4.5.

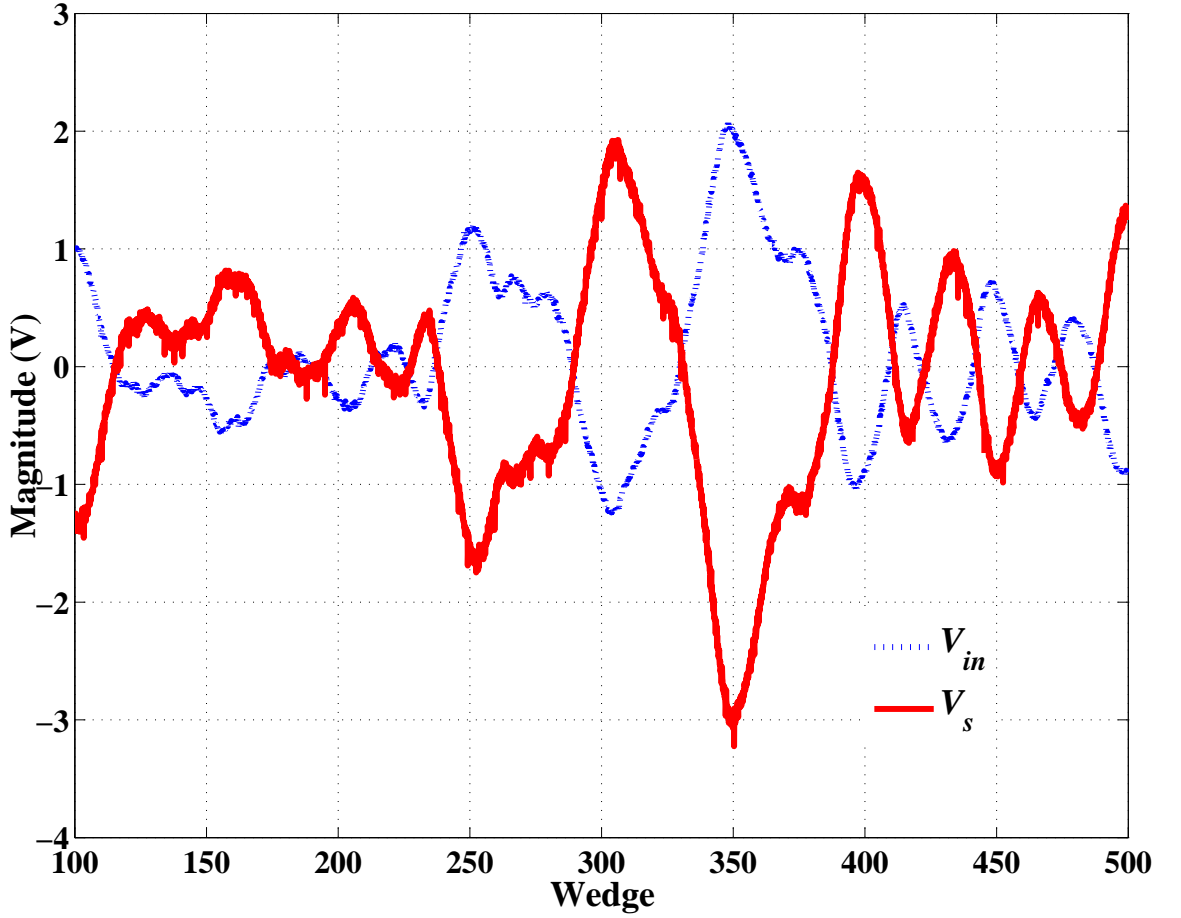


Figure 4.5: Time traces of V_s and V_{in} .

Referring to Figure 4.5, when V_{in} changes from -1.23 V to 2.08 V, the head is displaced by $\delta = 13.7 \times [2.08 - (-1.23)] = 45.35 \text{ nm}$. Corresponding to this displacement, V_s has changed from 1.91 V to -3.04 V. With $\kappa = 30$ in our design, we obtain that $V_p = V_s/\kappa = (|-3.04 - 1.91|)/30 = 165 \text{ mV}$. Hence, we have $S_s =$

$V_p/\delta = 3.64$ mV/nm. Our estimated S_a and S_s are consistent with the calculated values using (2.41) and (2.46). Due to confidentiality of the material properties, the detailed calculation using first principles are not presented.

4.4.1 Evaluation of EIDSSA

For comparison purpose, bode diagrams of PZT actuator with EIDSSA and the conventional IDSSA are presented in Figure 4.6.

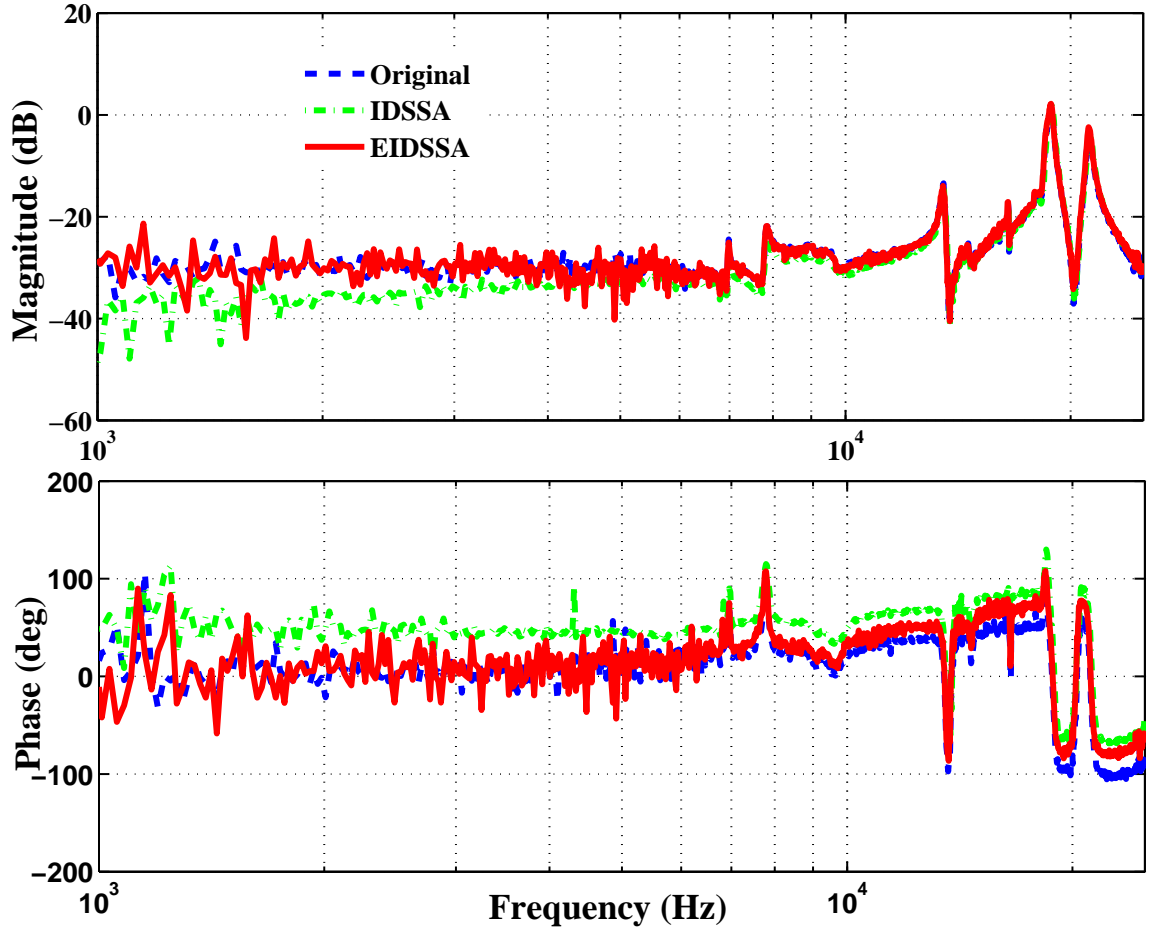


Figure 4.6: Frequency responses of PZT active suspension with IDSSA or EIDSSA.

In Figure 4.6, the bode diagram of PZT actuator with EIDSSA shows no gain

loss and almost zero phase shift due to $\gamma = 100\%$. In comparison, the bode diagram of PZT actuator with conventional IDSSA shows gain reduction up to 6 dB below 10 kHz, and significant phase distortions at all frequencies. According to our experiments, when EIDSSA is directly applied for actuation, the Total Runout (TRO) is slightly improved by 0.8%. TRO is doubled with IDSSA because of the gain loss and phase shift introduced by additional dynamics in the actuation path.

The frequency response of β coefficient in experiments matches with that in simulations, as shown in Figure 4.7.

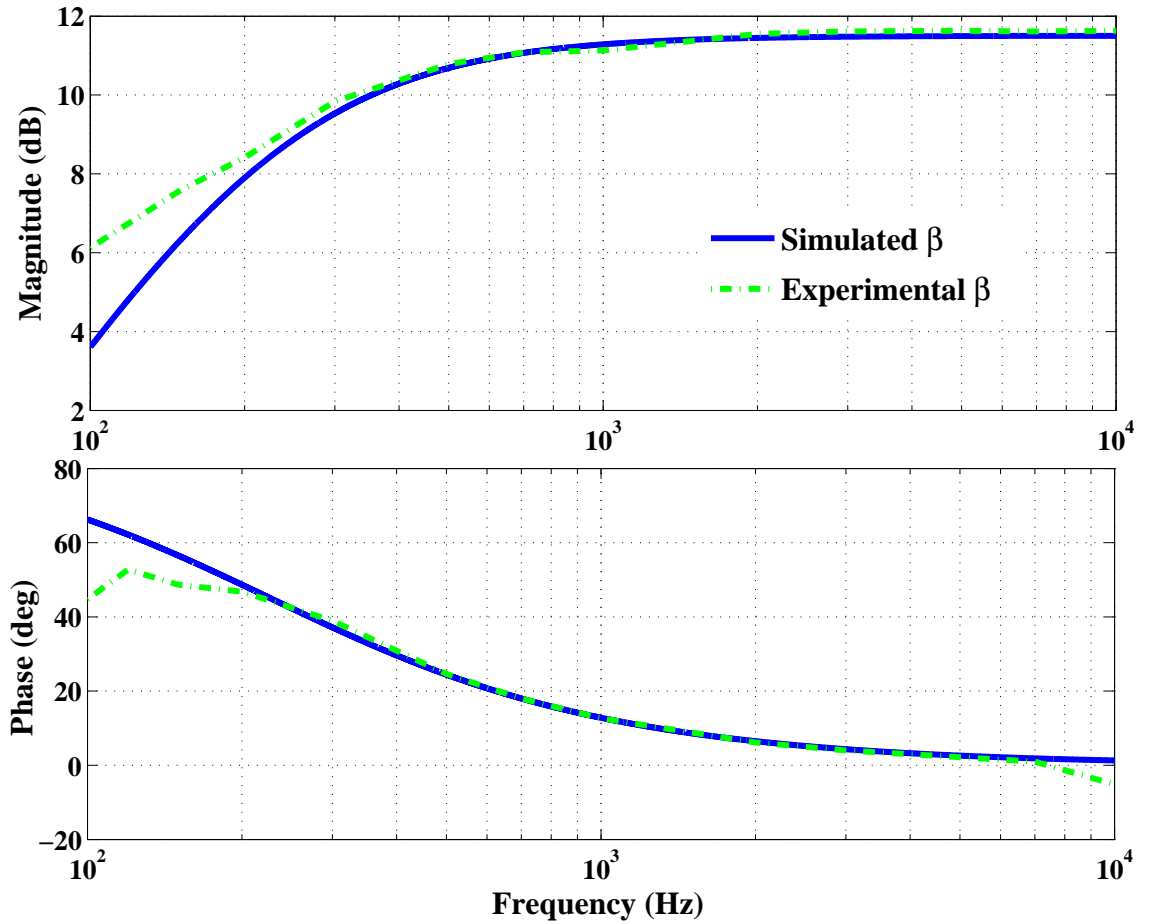


Figure 4.7: Frequency response of β in EIDSSA.

Figure 4.7 confirms our analysis that β is a high-pass filter. The sensing bandwidth is increased by pushing the cut-off frequency towards the lower end of the frequency range at around 300 Hz. The β performance ensures that the output V_s from EIDSSA sufficiently represents and resembles the head-displacement due to the deformation of PZT elements.

As presented in Figure 4.8, V_s contains rich signal contents in the frequency domain.

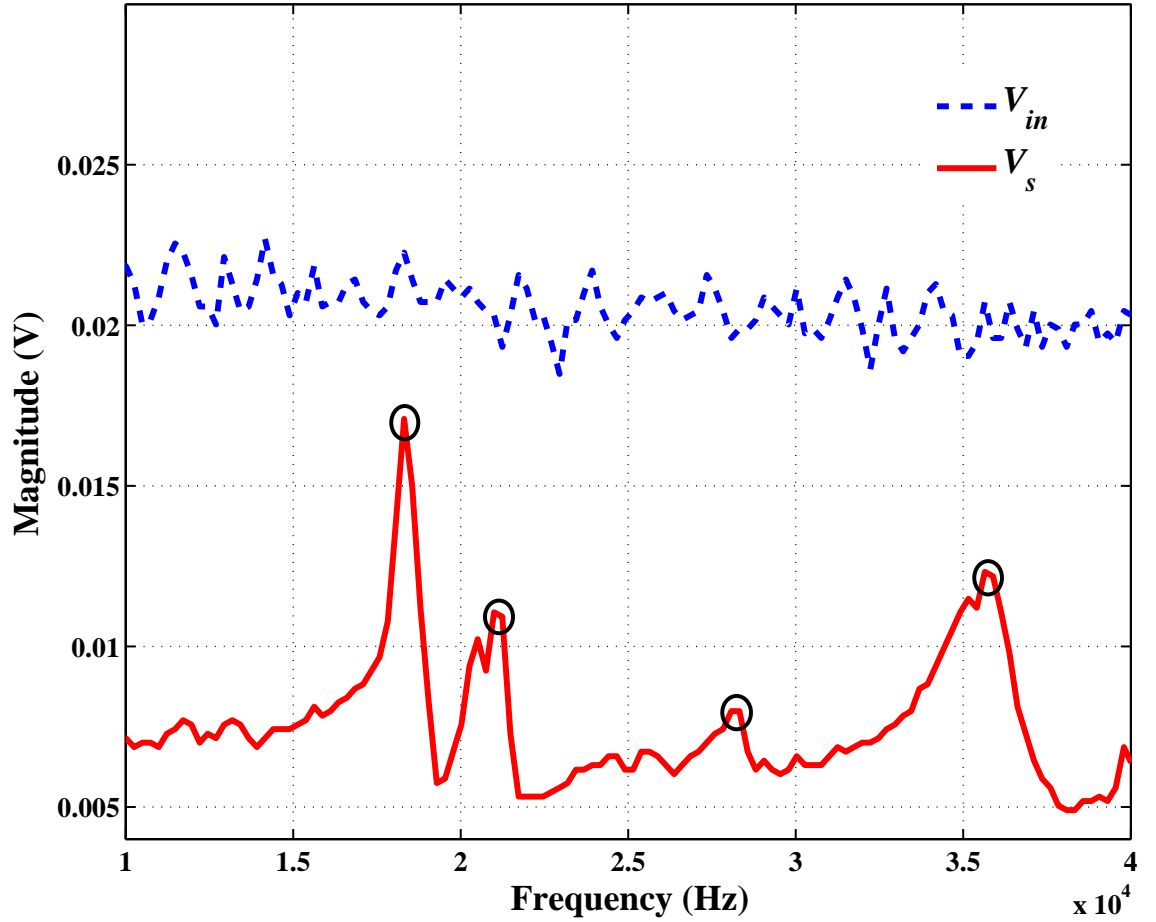


Figure 4.8: High frequency mode detection by EIDSSA.

In Figure 4.8, major off-track resonant modes at 18 kHz, 21 kHz, and 36 kHz can

be detected from V_s . The magnitude peaks correspond to resonant modes of the PZT active suspension. These modes are not excited by the input signal V_{in} but activated by in-drive disturbances such as airflow caused by disk rotations.

4.4.2 Control Performance of DMS Servo Incorporating EIDSSA

The bandwidth and stability margins of the modified DMS servo incorporating EIDSSA are presented in Table 4.2.

Table 4.2: Stability margins and bandwidth with and without EIDSSA.

	Without EIDSSA	With EIDSSA
Gain margin	7.7 dB	7.8 dB
Phase margin	24°	36°
Bandwidth	2465 Hz	2765 Hz

From Table 4.2, the phase margin of the new system has increased from 24° to 36° with slightly improved gain margin. At the same time, the servo bandwidth is extended by 300 Hz to 2765 Hz in the modified DMS servo with EIDSSA. The increased phase margin can be utilized to achieve even higher servo bandwidth. As shown in Figures 4.9 and 4.10, the TRO, Repeatable Runout (RRO), and Non-Repeatable Runout (NRRO) during track-following have been reduced by 3.84%, 4.07%, and 2.97%, respectively.

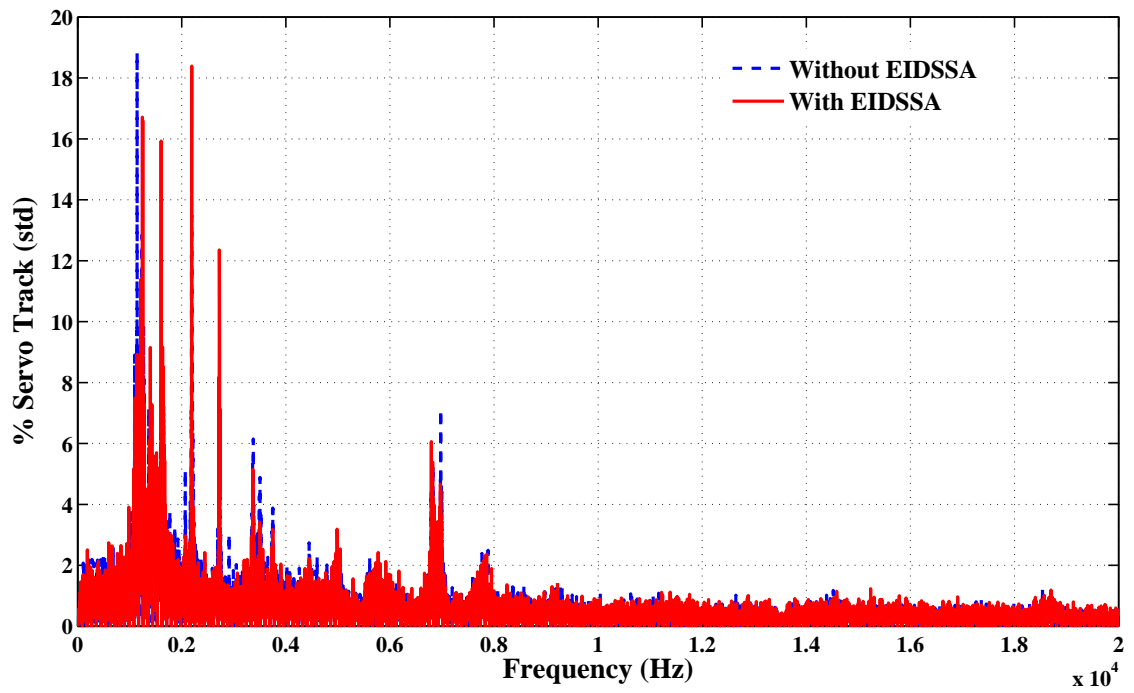


Figure 4.9: NRRO during track-following.

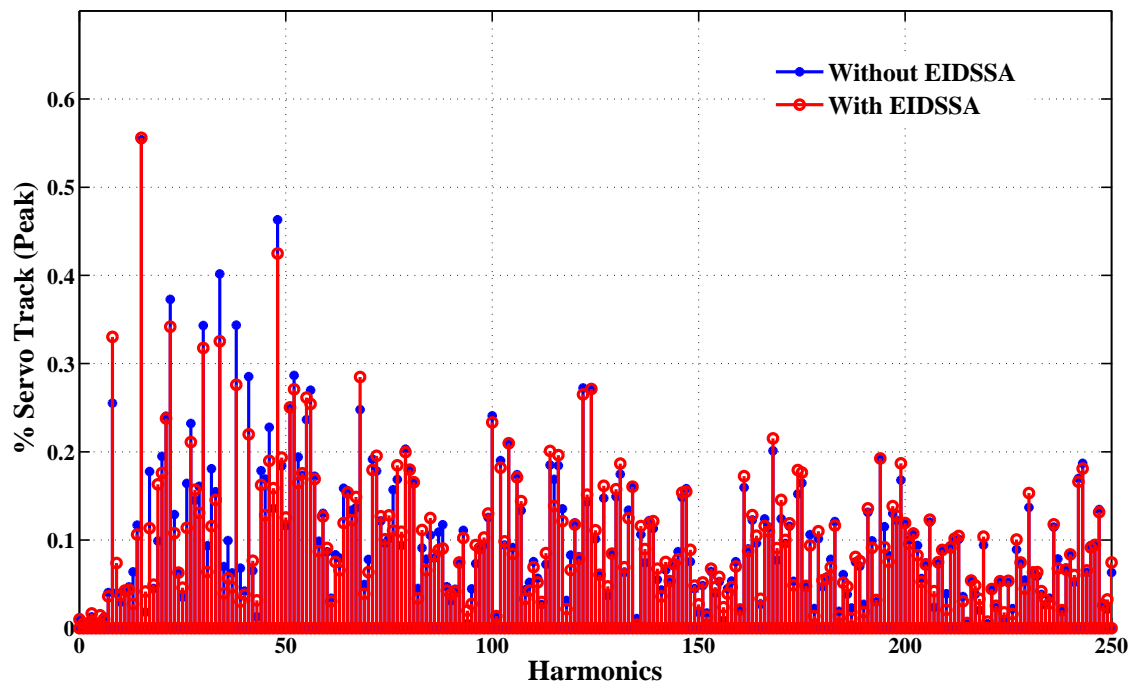


Figure 4.10: RRO during track-following.

The disturbance rejection capability is analyzed by the sensitivity transfer function $1/[(1 + C_M G_M)(1 + C_V G_V)]$. The frequency response of sensitivity transfer function is presented in Figure 4.11.

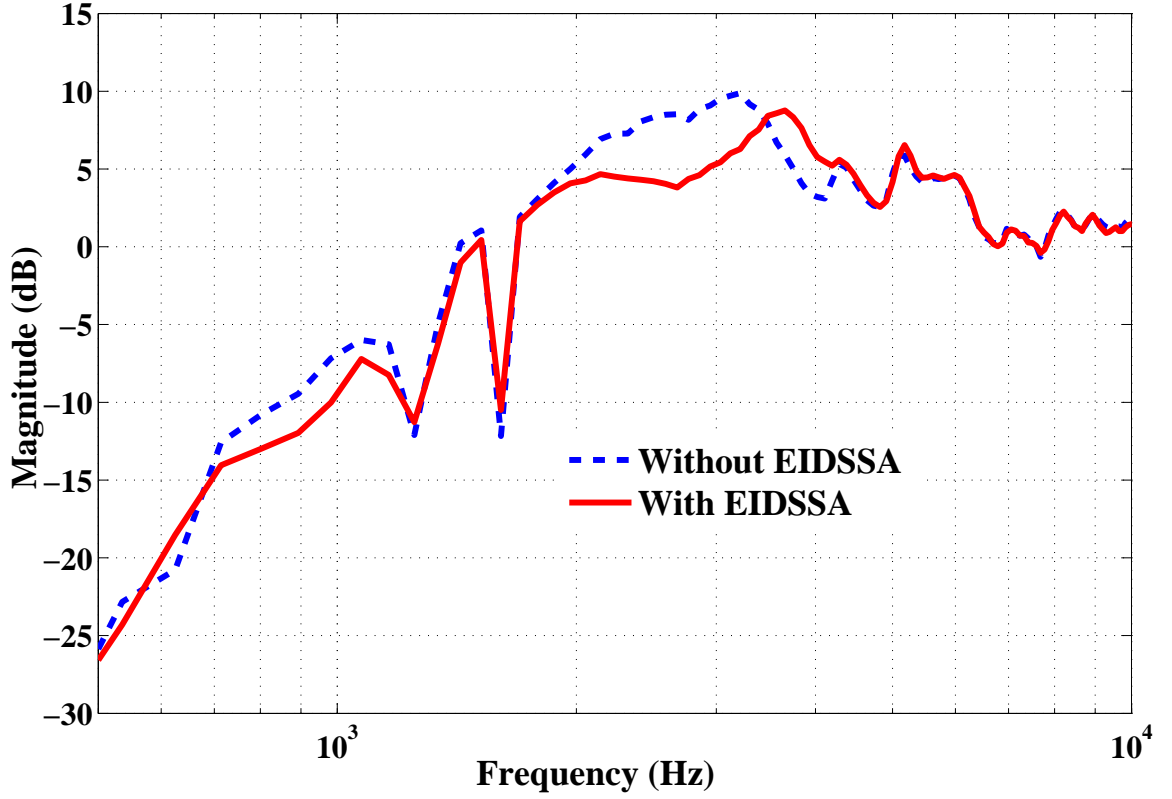


Figure 4.11: Sensitivity transfer function of DMS servos.

It is well known that linear systems are constrained by the famous waterbed effect. It is impossible to achieve arbitrary sensitivity reduction at all points on the imaginary axis. From Figure 4.11, the 0 dB crossover frequency is around 1.8 kHz, beyond which the sensitivity hump can be observed in the new system. It can be seen that the gain of sensitivity transfer function has been reduced by up to 5 dB from 2 to 3.5 kHz, while it increases from 3.5 to 4 kHz. There are also slight increases at higher frequencies which appear not obvious on the log-scale. Nevertheless, the peak

value of the gain of sensitivity transfer function is still lower in the new system. In our experiments, the dual-stage loop is closed after a calibration step to ensure the PZT loop gain remain the same with EIDSSA. As the phase margin is increased by 10 degrees, the gain crossover frequency is pushed higher, resulting in suppression of the gain of sensitivity transfer function from 2 to 3.5 kHz.

The results are highly desirable in real-world applications, because 2 to 3.5 kHz is the typical frequency range where audio-induced vibrations are introduced. In high-end HDD products, expensive vibrational sensors are often dedicatedly employed to improve the vibration rejection capability at these frequencies. With in-situ measurement of y_M^* by the proposed EIDSSA, such desirable performance can be readily achieved with a few additional cheap electronics.

In our experiments, single tone sinusoidal signal at 2.5 kHz is firstly applied to the base of HDD by a vibration speaker. The NRRO and RRO performances are presented in Figures 4.12 and 4.13, respectively.

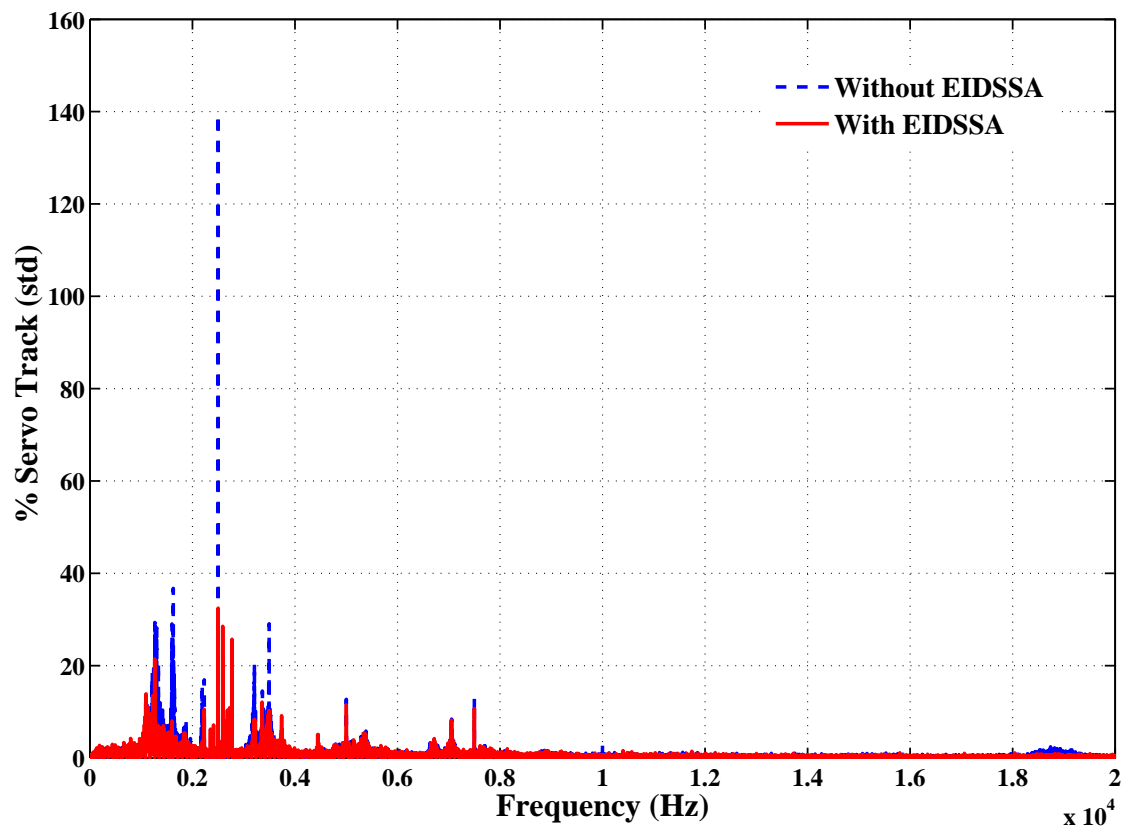


Figure 4.12: NRRO when playing 2.5 kHz sinusoidal by a vibration speaker.

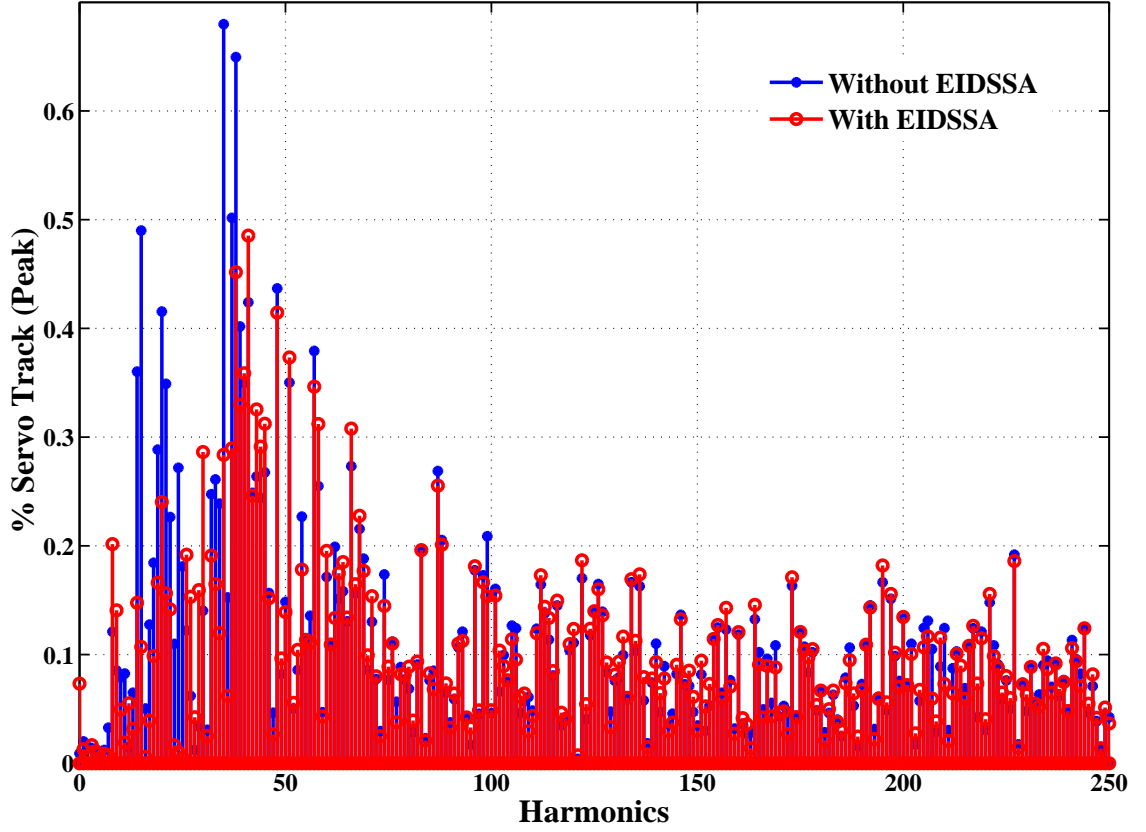


Figure 4.13: RRO when playing 2.5 kHz sinusoidal by a vibration speaker.

From Figures 4.12 and 4.13, the 2.5 kHz single tone sinusoidal disturbance is suppressed significantly owing to lowered gain in the sensitivity transfer function. The corresponding NRRO and RRO performances have been improved by 29.9% and 13.2%, respectively. The TRO has been reduced by 25.2% as compared to the baseline DMS servo without EIDSSA.

The NRRO and RRO performances with 3 kHz single tone sinusoidal disturbance applied are presented in Figures 4.14 and 4.15, respectively.

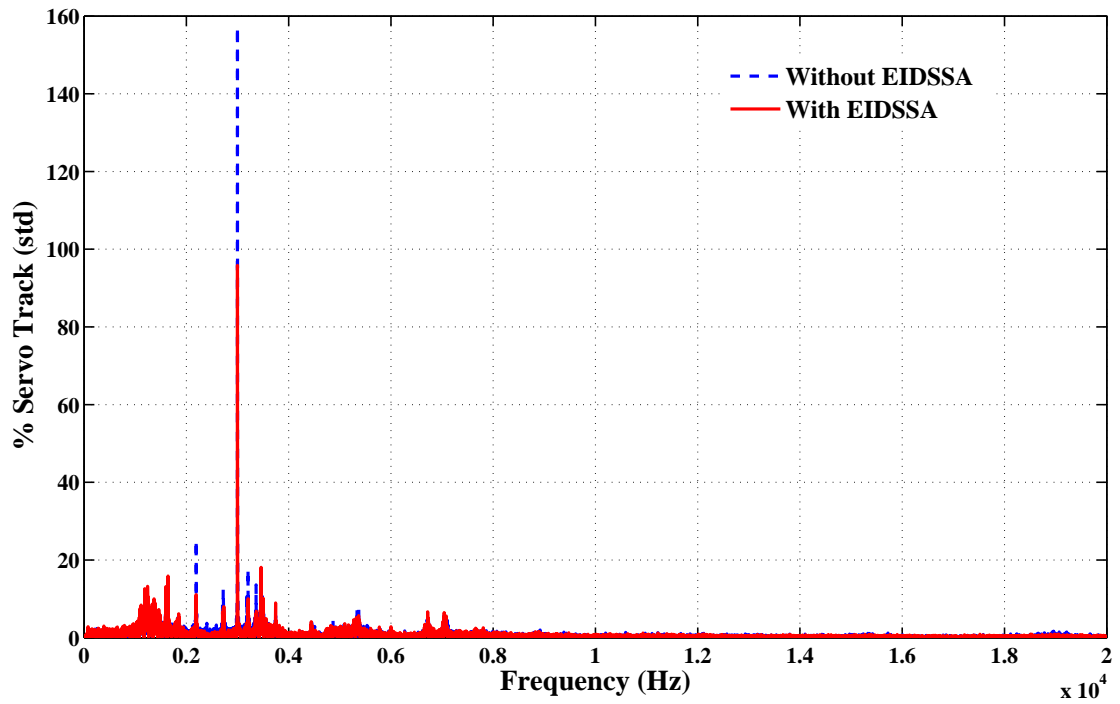


Figure 4.14: NRRO when playing 3 kHz sinusoidal by a vibration speaker.

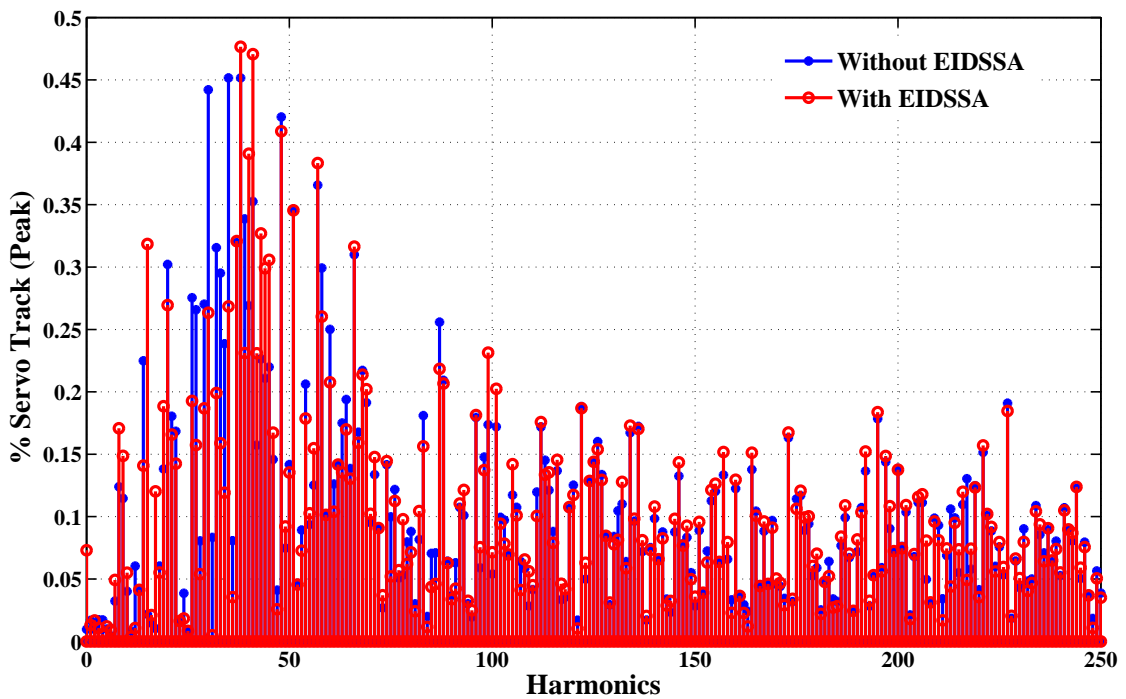


Figure 4.15: RRO when playing 3 kHz sinusoidal by a vibration speaker.

As shown in Figures 4.14 and 4.15, the NRRO, RRO, and TRO under 3 kHz vibrations are improved by 23.5 %, 5.8 %, and 16.5 %, respectively. The frequencies of 2.5 kHz and 3 kHz are chosen because they fall into the typical frequency range where audio-induced vibrations are introduced. Two frequencies are experimented to validate the vibration rejection capability for multiple frequencies of disturbances.

Then, pink noise containing all frequencies from 20 Hz to 20 kHz is applied to the base of HDD by a vibration speaker to evaluate the audio-induced vibration rejection capability in wider frequency spectrum. The results of NRRO and RRO are presented in Figures 4.16 and 4.17.

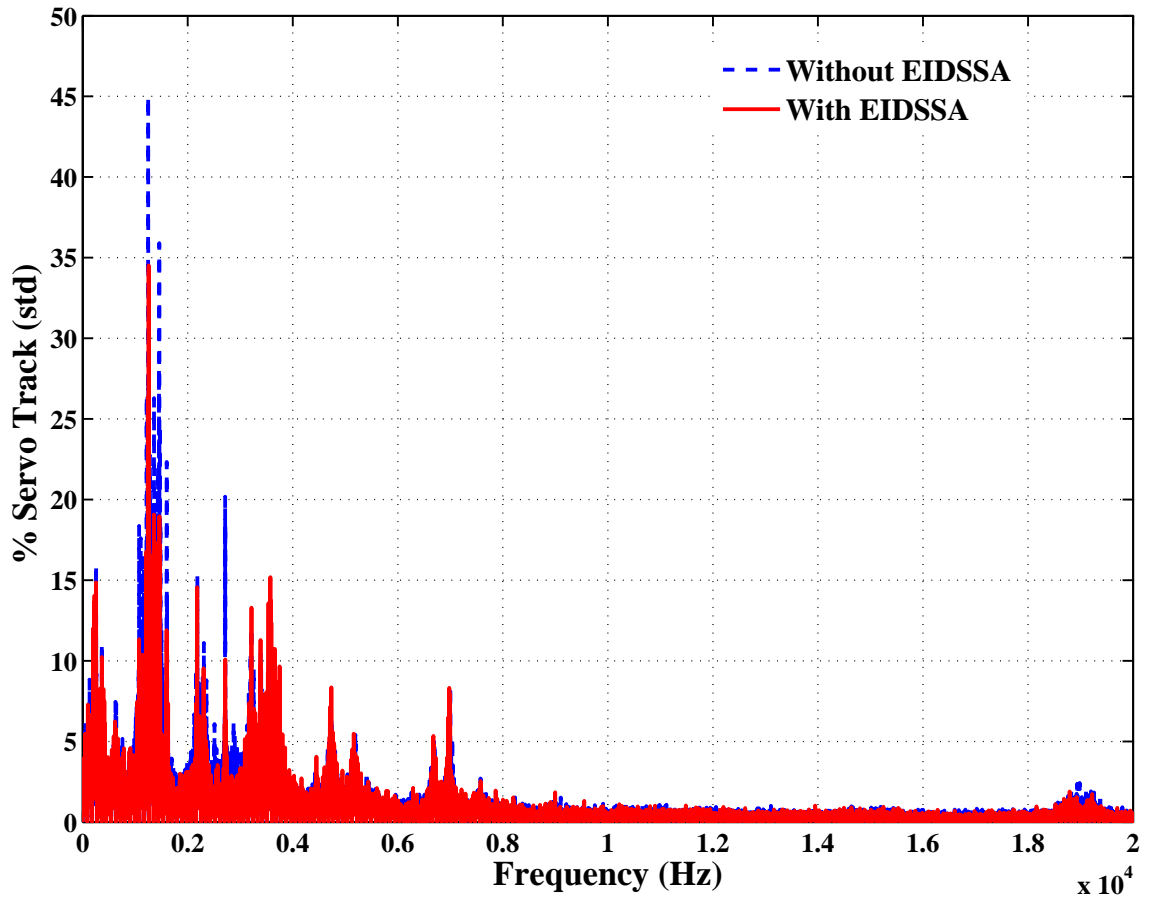


Figure 4.16: NRRO when playing pink noise by a vibration speaker.

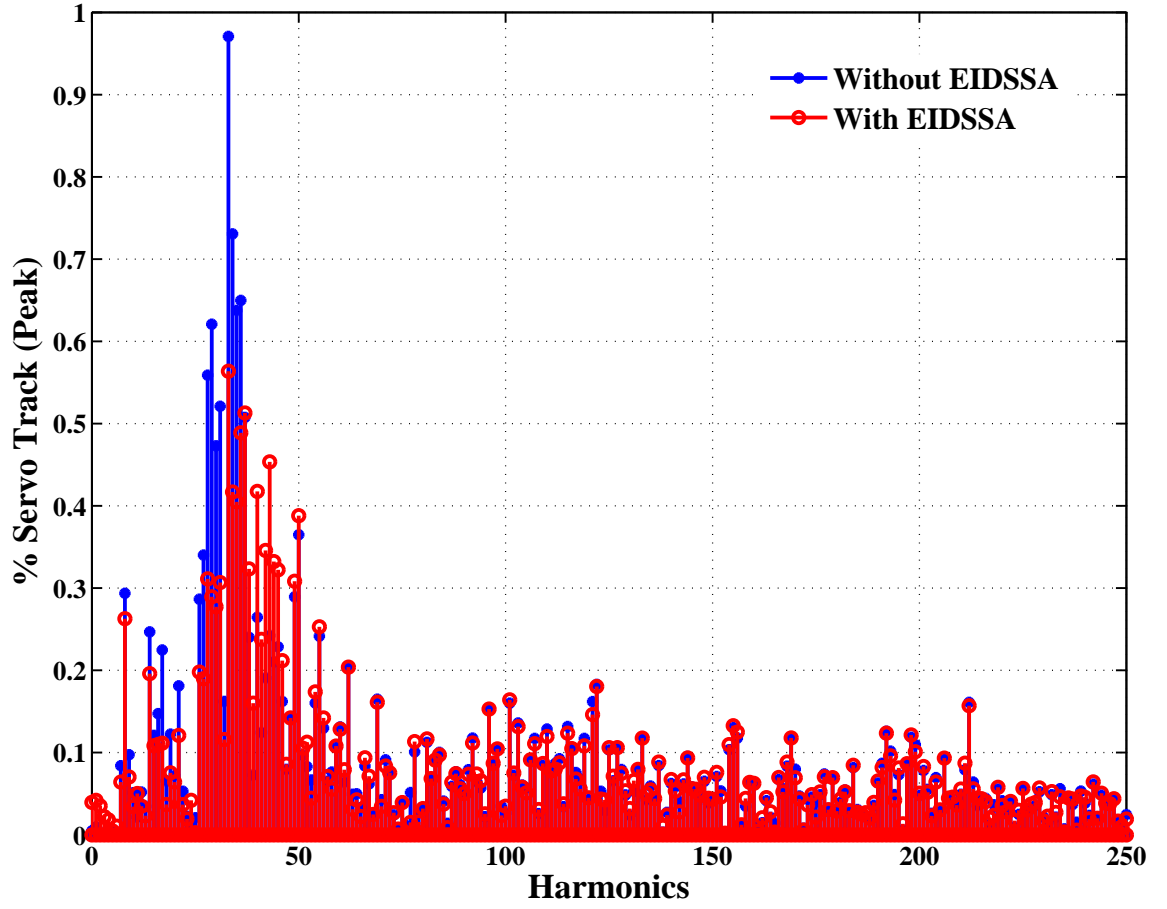


Figure 4.17: RRO when playing pink noise by a vibration speaker.

Based on Figures 4.16 and 4.17, the NRRO, RRO and TRO have been reduced by 7.92%, 9.35%, and 8.89%, respectively. Note that the same source of audio and sound level have been used for all testing in our experiments. Experimental results have confirmed that the modified DMS servo with the EIDSSA has stronger capability to reject audio-induced vibrations.

4.5 Summary

In this chapter, EIDSSA is realized and incorporated into commercially available HDDs for improved rejection of audio-induced vibrations. With EIDSSA, in-situ estimation of the relative head displacement decouples the VCM and PZT loops. The gain of sensitivity transfer function is significantly suppressed between 2 kHz and 3.5 kHz. Experimental results show that on-track TRO is reduced by 8.89% under pink noise audio vibrations and more than 16% under single tone sinusoidal audio-induced vibrations without additional loop tuning efforts.

In the next chapter, we will extend the self-sensing actuation to failure diagnosis in HDD systems. A method for automatic Head-on-Media (HOM) detection is established with incorporation of the proposed EIDSSA.

Chapter 5

Automatic Head-on-Media Detection

This chapter presents a novel method of Head-on-Media (HOM) detection with Pb-Zr-Ti (PZT) self-sensing actuation (SSA). Dissimilar to conventional approaches based on X-ray scanning, the proposed method is able to detect HOM drives automatically prior to spin-up activities. As spin-up retries are avoided, the drives can be preserved for failure analysis or data recovery. The mechanism of HOM detection using SSA technique is discussed by deriving the analytical model of PZT active suspension. The HOM detection methodology is established incorporating Enhanced Indirect-Driven Self-Sensing Actuation (EIDSSA) circuit. Experiments have been carried out to evaluate the effectiveness and consistency of the proposed method.

5.1 Background

Head-on-Media (HOM), also referred to as head-land-on-media, is a type of catastrophic failure in Hard Disk Drives (HDDs), which leaves read/write heads on disk media after spinning down. HOM has certain physical symptoms, including spindle motor failing to start and spin-up coupled with harsh sounds due to frictions between read/write heads and disk media when spindle motor is initiated. Figure 5.1 shows a typical HOM drive with heads stuck on the media surface when the disks have

come to completely stop. HOM could permanently damage read/write heads and disk media, therefore it should be prevented from happening by design. However, HOM still occurs in both manufacturing stage and field applications in real-world situations. There are many contributors to this class of failure, including firmware issues such as logic loop holes, hardware malfunctioning such as Voice Coil Motor (VCM) driver shorting to ground during normal operation, and large shocks due to free fall or mishandling [119,120]. Although the failure rate is considered to be low, the absolute number of occurrences can be very high in mass production.

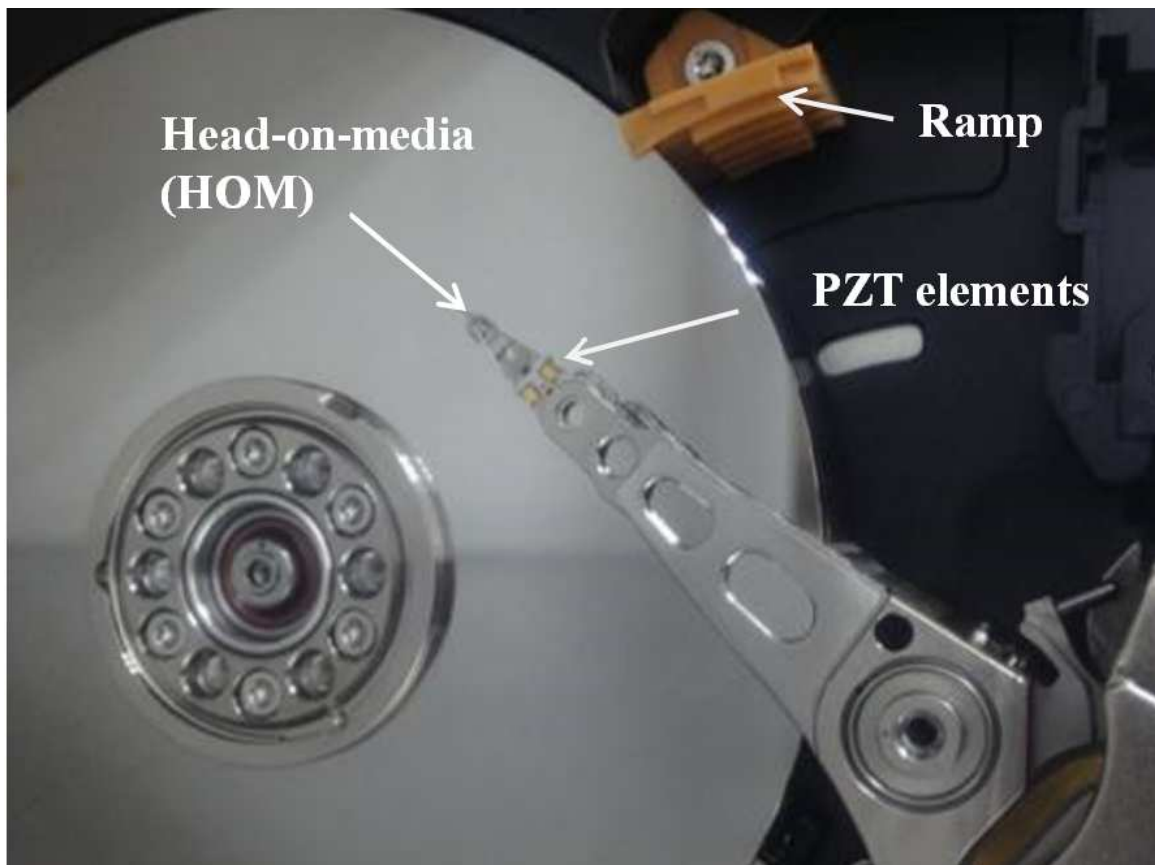


Figure 5.1: A dual-stage HDD with HOM.

Over the years, the HDD community has devoted tremendous efforts to under-

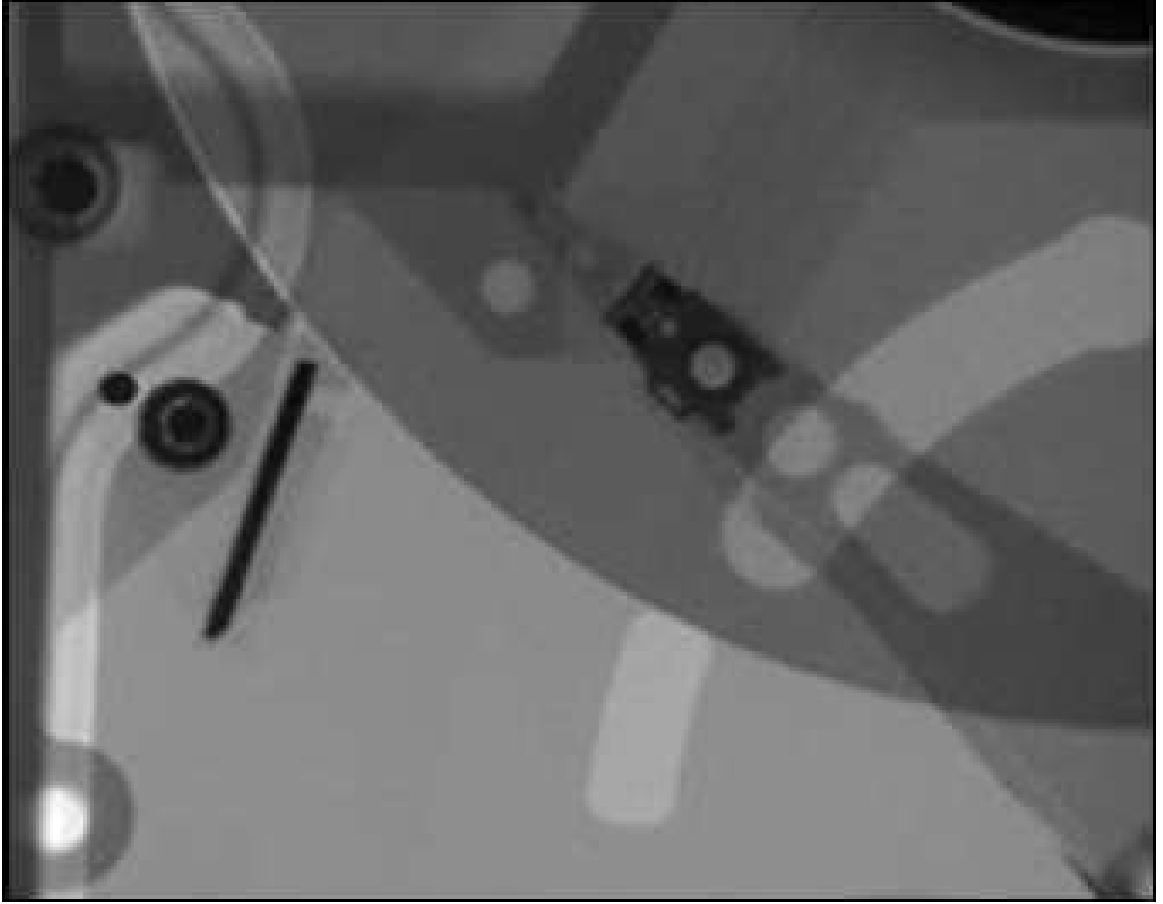


Figure 5.2: Manual HOM detection with X-ray machine.

stand various phenomenons associated with head disk interaction to improve reliability and performance. In the literature, precision mechanical components that experience sliding under contact and analysis of touch-down have been studied [121–125]. Various detection schemes for head/disk contacts based on extraneous sensors or firmware algorithms can be found in [58, 126]. However, HOM, as a worst case scenario of head disk interaction which results in inability of self-recovery, is seldom addressed. In practice, engineers rely on X-ray scanning machine to confirm HOM, as shown in Figure 5.2. If not, the HDD cover must be dismounted in clean room to visibly affirm HOM. Obviously, neither of these two practices is convenient, not

to mention the involvement of technical persons with relevant skills. Worse, an HDD will not be returned to original equipment manufacturers until many spindle spin-up retries have failed.

The disk media will be scratched or even damaged due to spin-up attempts after HOM is created. Consequently, customers' valuable data are at the risk of being corrupted permanently by "blindly" spin-up attempts. To speed up failure analysis in factory and to refrain from further damage to HOM drives in field applications, a method to perform in-drive HOM detection automatically prior to spin-up activities has been demanded for many years.

We propose a novel method of automatic HOM detection by sensing the deformation of Pb-Zr-Ti (PZT) elements when they are actuated simultaneously. The technique, also referred to as self-sensing actuation, models PZT elements as capacitance cascaded with 'induced' voltage source and employs a circuit to extract this voltage for deformation information. The self-sensing technique has been widely applied in applications of structural damage diagnosis and strain or strain rate sensing [60, 70, 127]. With the proposed method, HOM drives can be filtered out during customer and internal qualification processes. The normal drives are not adversely affected during the mass scanning. The impact to time-to-ready is also negligible due to fast execution.

In this chapter, the mechanism of HOM detection and the analytical model of PZT active suspension are presented, followed by discussions on the hardware design to obtain the sensing signal representing deformation of PZT elements caused by

HOM [72]. The proposed method is analyzed as comparison to conventional X-ray scanning method. The effectiveness and consistency are demonstrated and evaluated by experiments.

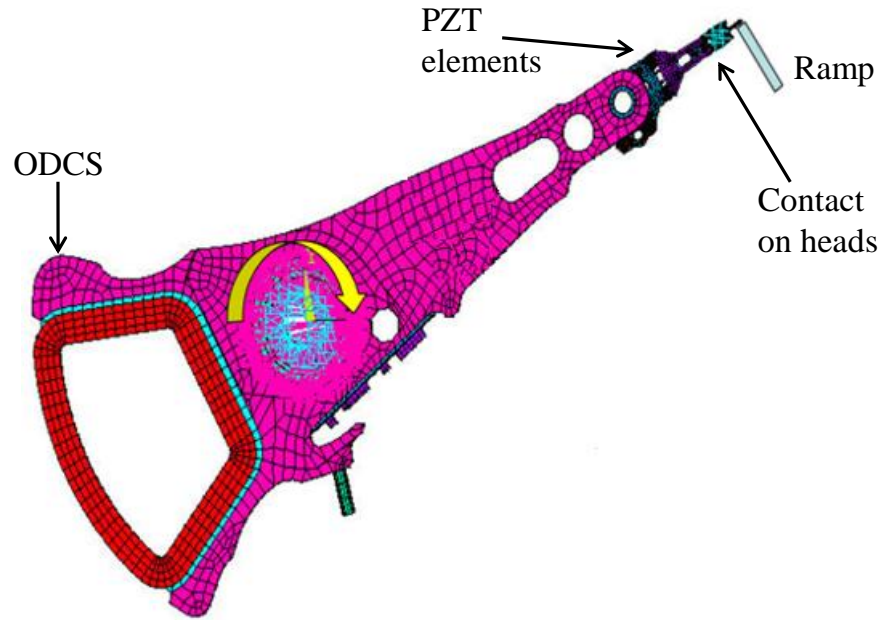
5.2 Mechanism of HOM Detection

In this section, the mechanism of HOM detection is discussed. HOM detection can be achieved by sensing the deformation of PZT elements. It further reveals that deformation of PZT elements can be obtained with a simple network of electronic components connected to PZT active suspension.

5.2.1 Principles of Operation

In normal situations, heads are parked on ramp when the disk stops rotating. This is called Head-on-Ramp (HOR). Referring to Figure 5.3, the motion of actuators is constrained by the structure of Outer Disk Crash Stop (ODCS), which is rubber-made and located at the base of VCM coil support. Damping effects from ODCS with lubricated ramp will result in small friction acting on heads and cause less deformation of PZT elements with minimum oscillations when they are actuated. Under HOM where heads are stuck on media surface, ODCS does not limit the motion of VCM, thus fails to provide damping effects, and larger deformation of PZT elements will be observed when they are actuated. Pivot mode at lower frequencies could be easily excited and the excitation will cause oscillation effects. As the deformations of PZT elements under HOR and HOM are different, HOM can be readily diagnosed by

referencing the deformation of PZT elements in HOR condition.



(a) Contact/friction under HOM with ODCS



(b) Rubber-made ODCS structure

Figure 5.3: Damping effect by ODCS structure.

5.2.2 Relation Between Sensing Voltage and Head Velocity

The PZT active suspension is modelled as a mass-spring damper system, as shown in Figures 2.9 and 2.10. According to piezoelectric relations [95], the electric displacement across the surface of PZT elements is given by

$$D_3 = d_{31}T_1 + \varepsilon_{33}^T E_3, \quad (5.1)$$

where D_3 , d_{31} , T_1 , ε_{33}^T , and E_3 are electric displacement, piezoelectric charge constant, stress, relative permittivity, and applied electric field, respectively. In piezoelectric relations, axes are identified by numerals rather than letters. Subscripts 1, 2, and 3 correspond to directions of x -, y -, and z - axes herein.

Electric charges Q across the surface of PZT elements can be computed as

$$Q = wlD_3. \quad (5.2)$$

Mechanical stress can be described as $T_1 = Y_p S_1$, where S_1 and Y_p are the strain of PZT elements and the Young's modulus of elasticity, respectively. The electric field E_3 satisfies that $E_3 = V_{in}/\rho$, where V_{in} is the PZT driving voltage.

It can be derived that the electric current i flowing through the surface of PZT elements is

$$i = \dot{Q} = \frac{lw\varepsilon_{33}^T}{\rho} \dot{V}_{in} - \frac{w\lambda d_{31}Y_p}{h} \dot{\delta}. \quad (5.3)$$

In Laplace domain, assuming zero initial conditions,

$$I(s) = \frac{slw\varepsilon_{33}^T}{\rho} V_{in}(s) - \frac{w\lambda d_{31}Y_p}{h} \Gamma(s), \quad (5.4)$$

where s denotes the Laplace operator and $\Gamma(s) = s\delta(s)$.

Similarly, it can be derived that

$$F(s) = -\left(\frac{w\varepsilon_{33}^T}{s_{11}^E d_{31} Y_p} + \frac{w d_{31}}{s_{11}^E}\right) V_{in}(s) + \frac{\rho}{s l s_{11}^E d_{31} Y_p} I(s), \quad (5.5)$$

where s_{11}^E is the compliance constant.

We can rewrite (5.4) and (5.5) together in matrix form as

$$\begin{bmatrix} F(s) \\ \Gamma(s) \end{bmatrix} = \Phi \begin{bmatrix} V_{in}(s) \\ I(s) \end{bmatrix}, \quad (5.6)$$

$$\text{where } \Phi = \begin{bmatrix} -\frac{w\varepsilon_{33}^T}{s_{11}^E d_{31} Y_p} - \frac{w d_{31}}{s_{11}^E} & \frac{\rho}{s l s_{11}^E d_{31} Y_p} \\ \frac{s h l \varepsilon_{33}^T}{\lambda \rho d_{31} Y_p} & -\frac{h}{w \lambda d_{31} Y_p} \end{bmatrix}.$$

Equation (5.6) describes the energy transformation process in PZT self-sensing actuators between the mechanical and electrical energy, as characterized by $(F(s), \Gamma(s))$ and $(V_{in}(s), I(s))$, respectively.

Furthermore, we denote PZT ‘induced’ voltage as $V_p(s)$ and capacitance of PZT elements as C_p . The current $I(s)$ across the surface of PZT elements can be expressed as

$$I(s) = s \left[V_{in}(s) - V_p(s) \right] C_p. \quad (5.7)$$

In our applications, the two faces of PZT elements are coated with thin-electrode layers. The capacitance can be determined from $C_p = \frac{\varepsilon_{33}^T w l}{\rho}$ [128].

It follows that

$$\begin{bmatrix} F(s) \\ \Gamma(s) \end{bmatrix} = \begin{bmatrix} -\frac{w d_{31}}{s_{11}^E} & -\frac{w \varepsilon_{33}^T}{s_{11}^E d_{31} Y_p} \\ 0 & \frac{s h l \varepsilon_{33}^T}{\lambda \rho d_{31} Y_p} \end{bmatrix} \begin{bmatrix} V_{in}(s) \\ V_p(s) \end{bmatrix}. \quad (5.8)$$

Equation (5.8) reveals that the deformation of PZT elements as represented by $\Gamma(s)$ can be readily obtained from the PZT-‘induced’ voltage $V_p(s)$.

5.3 Proposed HOM Detection Methodology

In this section, we propose to use self-sensing circuit to detect HOM prior to drive spin-up activities. Following the design of hardware circuit, the method of automatic HOM detection is presented in detail.

5.3.1 Realization of EIDSSA Circuit

The circuit of EIDSSA is employed to transfer the PZT-‘induced’ voltage V_p to PZT sensing voltage V_s . Based on the circuit realization in Figure 2.5, the values of the components are summarized in Table 5.1. Resistors with 1% tolerance are chosen and lumped gain from the differential amplifier is designed to be 33.

Table 5.1: Values of circuit components for automatic HOM detection.

Component	Values
$R_1 = R_2$	1.1 M Ω
$R_5 = R_6$	33 k Ω
$C_p = C_q$	4.7 nF

5.3.2 Design Procedures

With the EIDSSA circuit, the deformation of PZT elements can be obtained. HOM can be detected according to HOM index, which considers the deformation of PZT elements under HOR and HOM conditions. In dual-stage HDDs with PZT active suspension, the HOM index is defined as

$$\alpha = \frac{\bar{V}_{\text{HOM}}}{\bar{V}_{\text{HOR}}}, \quad (5.9)$$

where \bar{V}_{HOM} and \bar{V}_{HOR} are the maximal values of EIDSSA output under HOM and HOR conditions, respectively. The threshold of α for HOM diagnosis is obtained via extensive experimental evaluation on sufficiently large samples. As a rule of thumb, HOM can be confirmed if $\alpha > 1.5$ is satisfied for HDDs in 3.5 inch form factor. Note that the threshold will vary for products in other form factors, but it will not change for HOM levels as heads cannot slide on the media surface.

For comparison purpose, the conventional manual HOM detection based on X-ray scanning is presented in Figure 5.4.

In Figure 5.4, spin-up job is initiated as the first step and errors will be reported if spin-up retries are exhausted. Subsequently, engineers are deployed to manually retrieve the drives to undergo X-ray scanning operation. Based on the X-ray images, engineers will confirm if a drive belongs to HOM. If required, the HDD cover will be dismounted in clean room environment. The process is costly and time-consuming, and it relies heavily on engineers' technical expertise and professional judgement.

Our proposed HOM detection method, as shown in Figure 5.5, has eliminated the manual X-ray scanning operation and detects HOM prior to drive spin-up.

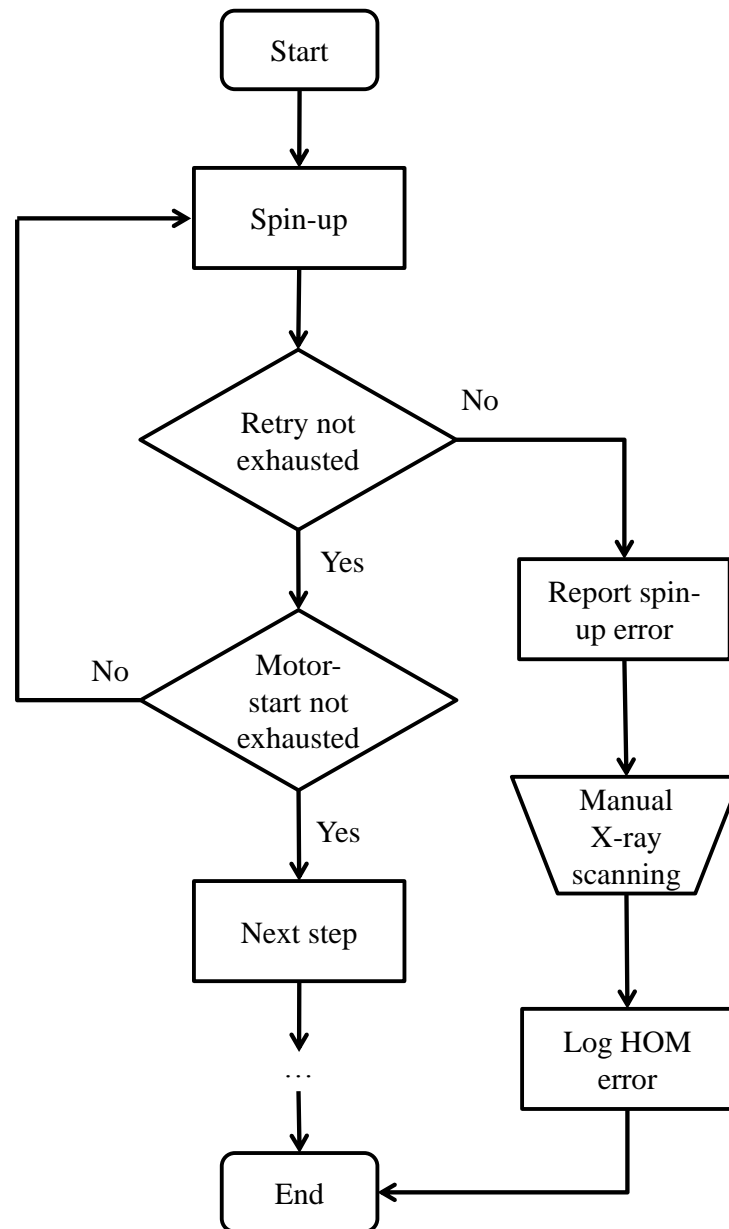


Figure 5.4: Conventional manual HOM detection method.

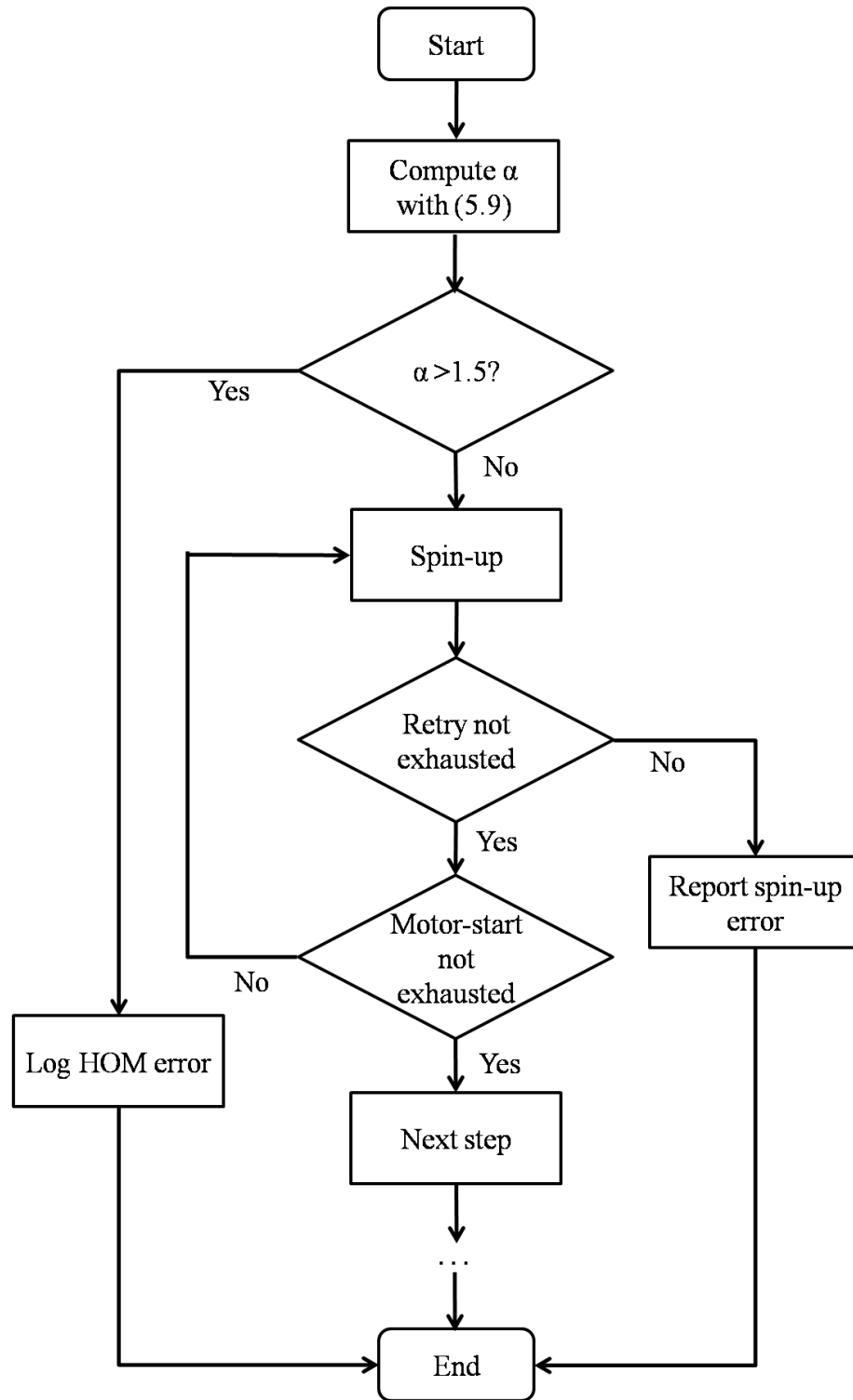


Figure 5.5: Proposed automatic HOM detection method.

In Figure 5.5, the computation of HOM index α is scheduled to be the first job prior to spin-up attempts. The computed α value will be compared against the threshold value of 1.5 for a decision. If it satisfies the criteria of $\alpha > 1.5$, an error representing HOM will be logged and the drive initialization process will be terminated immediately without proceeding to spin-up activities. If the criteria are not satisfied but spin-up retries or motor-start have exhausted, standard operating procedure will be executed as the next step. As the proposed method is able to produce specific error code, the X-ray scanning process in Figure 5.4 can be eliminated. Since the HOM detection is performed prior to spin-up activities, the risk of data loss due to media scratching and head damages can be reduced. In view of the large quantity of HDDs to be qualified during internal and customer testing, the benefits are more apparent if the proposed method is implemented into production.

5.4 Experimental Results and Discussions

In this section, the proposed HOM detection method is experimentally evaluated on a commercially available dual-stage HDDs in 3.5 inch form factor. To purposely actuate PZT elements, probing current as small as 3 mA is injected into the VCM driver. Alternatively, the excitation can be performed by applying an impulse injection at the PZT driver. As long as the PZT elements are actuated, the deformation of PZT elements can be obtained from the output from EIDSSA sensing circuit. In the following screens captured from oscilloscope, vertical divisions for the channels of EIDSSA output and injection current are 200 mV and 10 mA, respectively. The

magnitude of injection current is maintained for all experiments to maintain actuation efforts to PZT elements.

In HOR conditions, the heads are parked safely on ramp structure when the disk rotation speed is reduced. When the PZT elements are actuated, the rubber-made ODCS provides damping effects to the overall actuator structure at the base of VCM coil support. The output from EIDSSA circuit in HOR condition is shown in Figure 5.6.

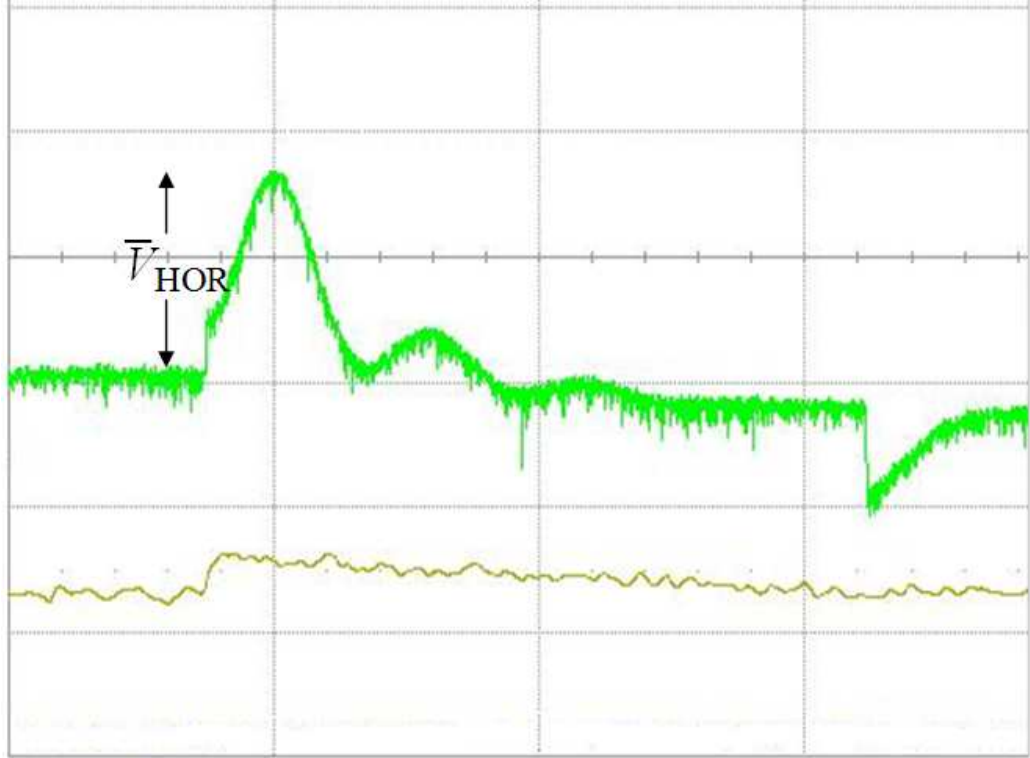


Figure 5.6: HOR detected by the proposed method (Top: sensing voltage V_s ; bottom: injection current).

From Figure 5.6, it can be seen that $\bar{V}_{HOR} = 330mV$ when the PZT elements are actuated by small injection current of 3 mA. Almost no subsequent oscillations can be observed as the in-plane pivot mode is not activated owing to the strong passive

damping effects rendered by the ODCS structure.

In HOM conditions, the heads are stuck on the media media. In practice, HOM can happen at various disk locations, including Inner Disk (ID), Middle Disk (MD), and Outer Disk (OD). The following experiments have beenk conducted to evaluate the proposed method at each disk location. Figure 5.7 refers to a case when heads land on ID after the disk has stopped rotating.

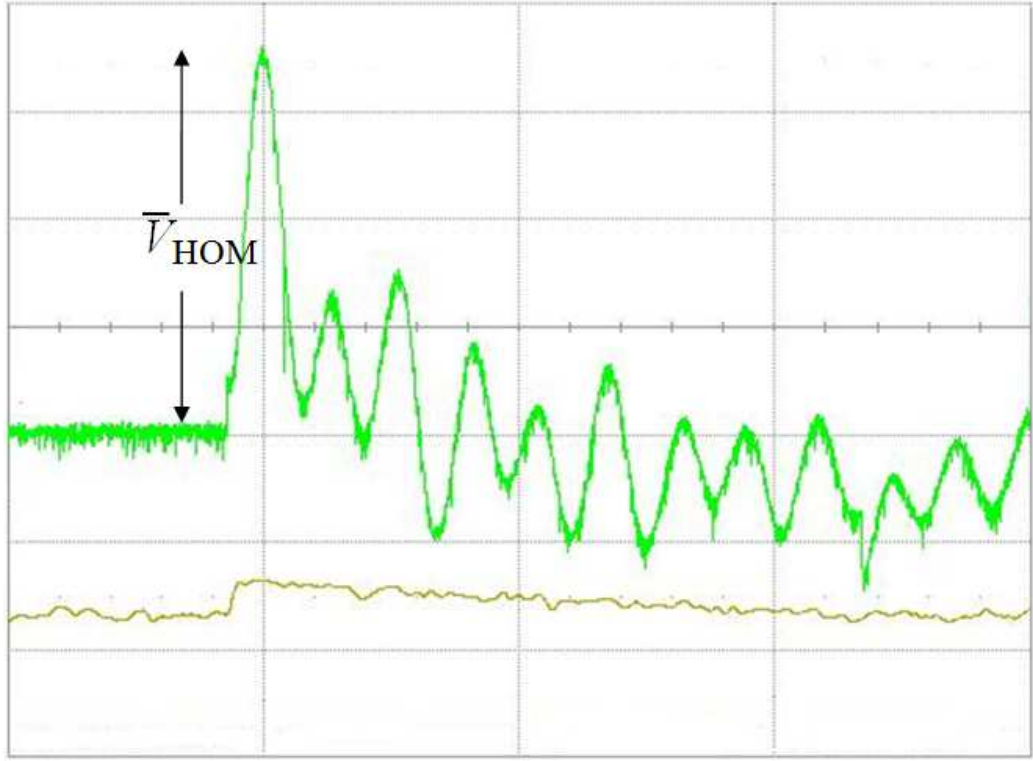


Figure 5.7: HOM at ID detected by the proposed method (Top: sensing voltage V_s ; bottom: injection signal).

In Figure 5.7, it can be seen that the sensing output from EIDSSA exhibits large signal magnitude as $\bar{V}_{\text{HOM}} = 721$ mV. Oscillations are noticeable when the low frequency mode is excited as the damping effects from ODCS no longer exist.

According to (5.9), we have $\alpha = 2.18$ for HOM at ID, which is beyond the pre-set HOM threshold.

Next, the proposed method is evaluated for HOM at MD location, as shown in Figure 5.8.

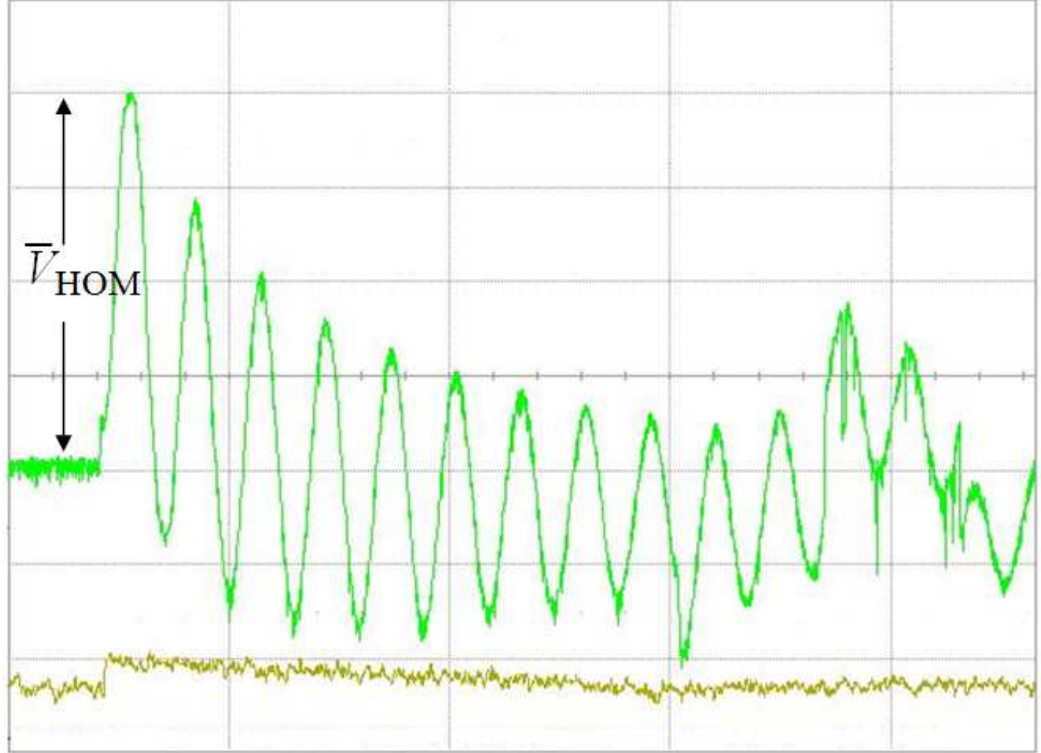


Figure 5.8: HOM at MD detected by the proposed method (Top: sensing voltage V ; bottom: injection signal).

With reference to Figure 5.8, it can be seen that $\bar{V}_{\text{HOM}} = 785$ mV for HOM at MD, which is slightly larger than that in ID. Based on the criteria described in (5.9), it can be obtained that $\alpha = 2.38$. As such, HOM is confirmed using our proposed method. Similar to the case at ID, oscillations are noticeable owing to the absence of passive damping mechanism in HOM conditions.

Furthermore, the detection of HOM at OD is experimentally studied and the results are shown in Figure 5.9.

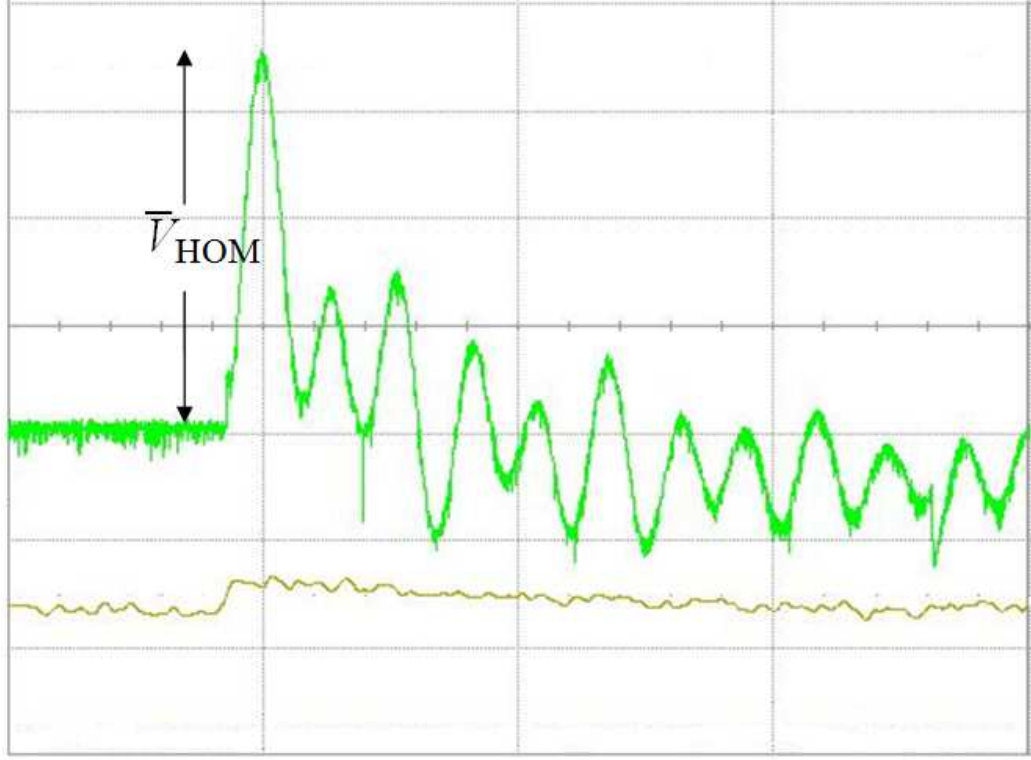


Figure 5.9: HOM at OD detected by the proposed method (Top: sensing voltage V ; bottom: injection signal).

As shown in Figure 5.9, it can be seen that $\bar{V}_{\text{HOM}} = 720 \text{ mV}$. Similar to HOM at ID and MD, the mechanical resonant mode is excited, and the excitation results in prolonged transient response. HOM can be affirmed as $\alpha = 2.18$. HOM error code is logged and spin-up tasks are not be executed.

Last but not least, the repeatability and consistency of the proposed method are evaluated. Experiments are conducted for ten runs for both HOR and HOM at ID, MD, and OD locations on the media surface. The \bar{V}_{HOR} and \bar{V}_{HOM} values are

presented in Figure 5.10.

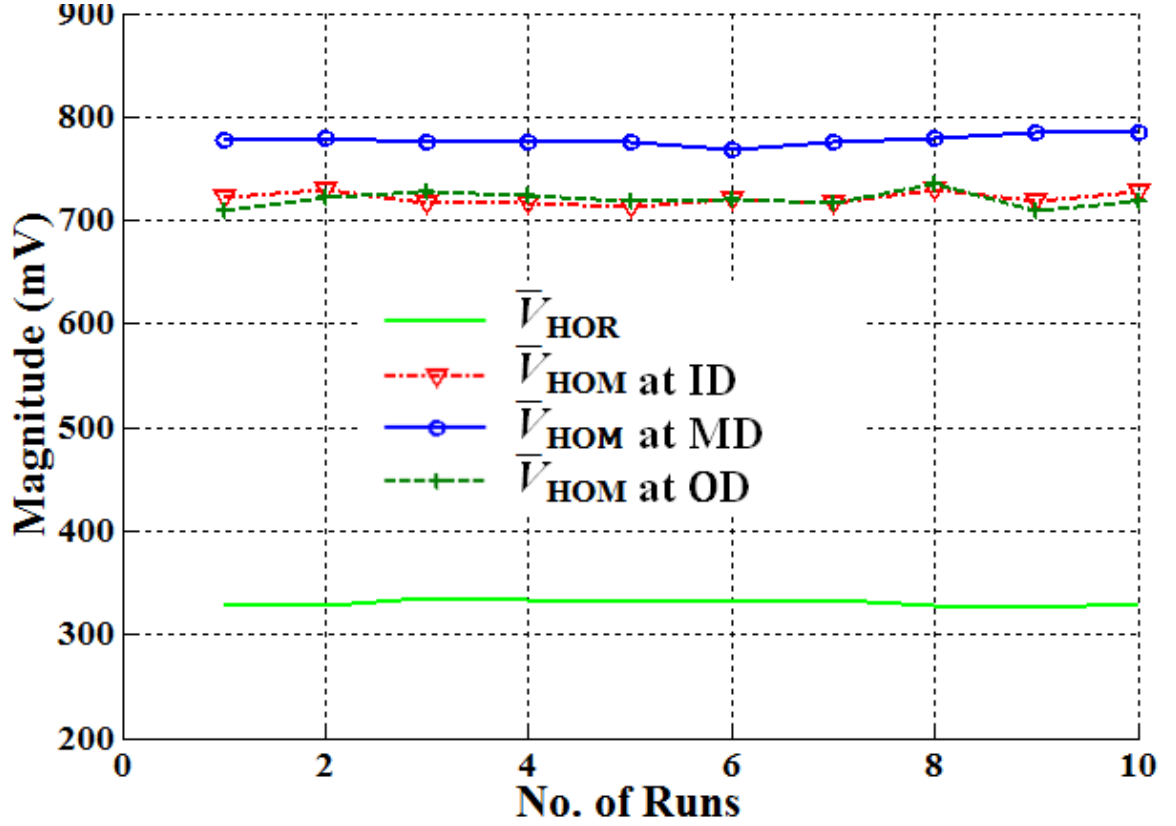


Figure 5.10: \bar{V}_{HOM} and \bar{V}_{HOR} for HOR and HOM at ID, MD, and OD locations.

It is worth noting from Figure 5.10 that $\bar{V}_{HOM} > \bar{V}_{HOR}$ holds for all runs across various disk locations. Further calculation reveals that $\alpha > 1.5$ in all tests for HOM. This means that the proposed method is repeatable to detect HOM.

Statistical analysis on \bar{V}_{HOR} , \bar{V}_{HOM} , and α is also conducted to evaluate the consistency of the propose method. The statistics are summarized in Table 5.2.

Table 5.2: Statistics of \bar{V}_{HOR} , \bar{V}_{HOM} , and α .

	\bar{V}_{HOR}	\bar{V}_{HOM}		
		ID	MD	OD
Mean (mV)	330.7	720.1	777.7	721.1
Std (mV)	3.0	4.9	7.8	4.1
Mean (α)	1	2.17	2.35	2.18

Table 5.2 shows that the mean values of \bar{V}_{HOM} are above 700 mV and the standard deviations are less than 8 mV across disk locations. The mean values of α are significantly larger than the pre-set HOM threshold. Thus, the consistency of the proposed HOM detection method is confirmed.

5.5 Summary

In this chapter, a novel method for HOM detection with PZY self-sensing actuation is proposed. Automatic HOM detection is achieved prior to drive spin-up activities. The risk of data loss due to media scratching is mitigated significantly. The proposed method is useful for failure analysis in both internal and customer qualification processes as well as field applications. Experiments have been carried out to demonstrate the effectiveness and consistency.

In the next chapter, we conclude this dissertation and discuss future research directions.

Chapter 6

Conclusion and Future Work

With the spread of cloud computing and big data applications, the trend of increasing storage capacity demands continuing multifaceted development of Hard Disk Drive (HDD) technologies. This dissertation concentrates on the research and development of advanced sensor fusion and vibration control technologies for the next generation ultra-high density dual-stage HDDs.

The main findings and results presented in this dissertation are:

1. Proposing Enhanced Indirect-Driven Self-Sensing Actuation (EIDSSA) and Asymmetrical Indirect-Driven Self-Sensing Actuation (AIDSSA) to remove the coupling effects between actuation and self-sensing, thus achieving independent design of each function. In particular, AIDSSA extends the self-sensing capability to the entire frequency spectrum and simplifies the decoupling conditions for practicality. Sensitivity of piezoelectric-actuated systems is analyzed to reveal the design trade-offs from a mechanical viewpoint, using the Pb-Zr-Ti (PZT) active suspension in commercial dual-stage HDDs as an example, .
2. Advancing the track-settling process by earliest switch-on of PZT actuators while ensuring non-saturation. Based on the theory of maximum output admissible set, a methodology of calculating the saturation boundary of PZT

actuators is proposed. Based on Position Error Signal (PES) and Voice Coil Motor (VCM) velocity error, the optimal switch-on conditions are determined. Thanks to early activation of dual-stage control loop, the control signal range is utilized more efficiently to reduce both overshoot and post-seek oscillations. The 5 %-track settling time is also shortened by 16%.

3. Constructing a modified Decoupled Master Slave (DMS) servo control structure incorporating self-sensing mechanism for improved rejection of audio-induced vibrations in dual-stage HDDs. Significant reduction of the gain of the sensitivity transfer function between 2 kHz and 3.5 kHz improves the Total Runout (TRO) by 25.2 % under the single tone sinusoidal signal at 2.5 kHz and by 8.89 % under the pink noise across a wider frequency spectrum.
4. Formulating a method for automatic Head-on-Media (HOM) detection, with which PZT actuators are incorporated with EIDSSA to diagnose HOM during internal and customer qualification process. As compared to conventional X-ray scanning method, the proposed approach reduces the risk of media scratching and data loss significantly as it does not require disk spin-up activities.

With the advancements in magnetic recording technologies, the HDD industry is striving to push the boundary of achievable recording density beyond the milestone of 1 Tb/in². To support a recording density of more than 10 Tb/in² for the next generation high-performance HDDs, with specific applications to cloud computing and data centers, advanced magnetic recording with read/write head-positioning accuracy at the sub-nano scale in the presence of internal and external disturbances is required.

The ambitious goal warrants the research and development of advanced sensor fusion and vibration control technologies in HDDs. In view of the results obtained, the following work should be emphasized in future research:

1. In situations where time-varying environmental and operating conditions exist, the accurate estimation of capacitance in piezoelectric elements becomes a challenge. For conventional DDSSA, it has been shown that adaptive mechanism is effective to overcome this difficulty [73, 78, 83]. Further to our work on EIDSSA and AIDSSA, hybrid circuit topologies with adaptive mechanism will be developed. Optimization algorithms, such as Least Mean Square (LMS) can be synthesized to adapt the reference capacitance value. As a result, the capacitance of piezoelectric elements can be estimated in-situ and other non-linear effects such as hysteresis and creep can also be dealt with accordingly.
2. In dual-stage HDD systems, oscillations stemming from the weakly damped resonances of the PZT active suspension are a major source of PES in track-following operation, putting a limitation on the achievable track density. The conventional approach of handling resonant modes is to employ notch filters in series with the PZT active suspension [17]. However, the major drawbacks of notch filters are that they not only attenuate the gain around target frequencies but also create rapid changes of phase which result in phase loss. Mechanical resonances can be compensated by Positive Position Feedback (PPF) Active Mode Damping (AMD) techniques [64, 69], but the damping controller has to be designed for each mode. This causes computation burden and difficulty

in controller tuning. Recently, the Integral Resonant Control (IRC) scheme has been developed to damp the resonant modes of PZT actuators without introducing excess phase loss [129–132]. In future, the self-sensing based IRC technique will be synthesized in the dual-stage HDD servos for Robust Active Mode Damping (RAMD). As a result, increased phase margin and extended servo bandwidth can be expected.

3. In HDD systems, the read/write head flies extremely close to a media. The distance can be as close as 1 nm. With such low flight height, touch-down events occur frequently during the read/write operations. The touch-down may excite resonant modes at very high frequencies, which are beyond the detection capability of PES due to sampling rate constraint. The excitation of resonant modes contaminate the positioning accuracy, thus should be tackled for ultra-high density HDDs. Increasing the number of servo sector for higher sampling rate is infeasible because it inevitably reduces the space for user data storage. In future, the proposed EIDSSA and AIDSSA will be extended to study the correlation between the touch-down and the self-sensing signals. A touch-down detection scheme based on self-sensing mechanism will be established and the touch-down events and associated effects will be managed and compensated for improved head-positioning accuracy.

Bibliography

- [1] J. Williamson. “Roadmap suggests hard drive storage will exceed 100 Tb by 2025”, November 2014. [Online]. Available: <http://www.techspot.com/news/58987-roadmap-suggests-hard-drive-storage-exceed-100tb-2025.html>
- [2] J. VanWagoner. “Will hard disk drives be replaced by solid state drives”, December 2013. [Online]. Available: <https://www.quora.com/Will-hard-disk-drives-be-replaced-by-Solid-State-drives>
- [3] T. Yamaguchi, M. Hirata, and C. K. Pang, *Advances in high-performance motion control of mechatronic systems*. Boca Raton: Taylor & Francis, 2014.
- [4] J. Gantz and D. Reinsel, “The digital universe in 2020: big data, bigger digital shadows, and biggest growth in the far east,” *IDC White paper*, December 2012.
- [5] T. Noyes and W. Dickinson, “The random-access memory accounting machine ii. the magnetic-disk, random-access memory,” *IBM Journal of Research and Development*, vol. 1, no. 1, pp. 72–75, January 1957.
- [6] International Roadmap Committee. “Advanced Storage Technology Consortium Roadmap of HDDs”, 2014. [Online]. Available: http://idema.org/?page_id=2269
- [7] S. Nakamura, K. Suzuki, M. Ataka, H. Fujita, S. Basrour, V. Soumann,

- M. Labachellerie, and W. Daniau, "An electrostatic microactuator using LIGA process for a magnetic head tracking system of hard disk drives," *Microsystem Technologies*, vol. 5, no. 2, pp. 69–71, December 1998.
- [8] H. Toshiyoshi, M. Mita, and H. Fujita, "A MEMS piggyback actuator for hard-disk drives," *Journal of Microelectromechanical Systems*, vol. 11, no. 6, pp. 648–654, December 2002.
- [9] D. A. Horsley, "Microfabricated electrostatic actuators for magnetic disk drives," Ph.D. thesis, University of California, Berkeley, 1998.
- [10] T. Hirano, L.-S. Fan, T. Semba, W. Y. Lee, J. Hong, S. Pattanaik, P. Webb, W.-H. Juan, and S. Chan, "High-bandwidth HDD tracking servo by a moving-slider micro-actuator," *IEEE Transactions on Magnetics*, vol. 35, no. 5, pp. 3670–3672, September 1999.
- [11] H. Fujita, K. Suzuki, M. Ataka, and S. Nakamura, "A microactuator for head positioning system of hard disk drives," *IEEE Transactions on Magnetics*, vol. 35, no. 2, pp. 1006–1010, March 1999.
- [12] H. Kuwajima, H. Uchiyama, Y. Ogawa, H. Kita, and K. Matsuoka, "Manufacturing process of piezoelectric thin-film dual-stage actuator and its reliability for HDD," *IEEE Transactions on Magnetics*, vol. 38, no. 5, pp. 2156–2158, September 2002.
- [13] R. B. Evans, J. S. Griesbach, and W. C. Messner, "Piezoelectric microactuator for dual stage control," *IEEE Transactions on Magnetics*, vol. 35, no. 2, pp. 977–982, March 1999.

- [14] M. Tokuyama, T. Shimizu, H. Masuda, S. Nakamura, M. Hanya, O. Iriuchijima, and J. Soga, “Development of a ϕ -shaped actuated suspension for 100-kTPI hard disk drives,” *IEEE Transactions on Magnetics*, vol. 37, no. 4, pp. 1884–1886, July 2001.
- [15] I. Naniwa, S. Nakamura, S. Saegusa, and K. Sato, “Low voltage driven piggyback actuator of hard disk drives,” in *Proceedings of 12th IEEE International Conference on Micro Electro Mechanical Systems*, Orlando, FL, USA, January 21 1999, pp. 49–52.
- [16] S. Koganezawa, K. Takaishi, Y. Mizoshita, and T. Yamada, “Development of an integrated piggyback milli-actuator for high density magnetic recording,” in *Proceedings of the International Conference on Micromechatronics for Information and Precision Equipment*, Tokyo, Japan, July 1997, pp. 54–55.
- [17] A. Al Mamun, G. Guo, and C. Bi, *Hard disk drive: mechatronics and control*. Boca Raton, FL: CRC Press, 2006.
- [18] J. Nie and R. Horowitz, “Control design of concentric self-servo track writing systems for hard disk drives,” in *Proceedings of the 2010 American Control Conference*, Baltimore, MD, USA, June 30–July 2 2010, pp. 2631–2640.
- [19] X. Chen and M. Tomizuka, “Spiral servo writing in hard disk drives using iterative learning based tracking control,” in *Proceedings of the 18th World Congress of the International Federation of Automatic Control (IFAC)*, Milano, Italy, August 28–September 2 2011, pp. 5279–5285.
- [20] G. F. Franklin, J. D. Powell, and M. L. Workman, *Digital control of dynamic*

- systems*, 3rd ed. Menlo Park, CA, USA: Addison Wesley, 1998.
- [21] M. L. Workman, “Adaptive proximate time-optimal servomechanisms,” Ph.D. thesis, Stanford University, CA, 1987.
 - [22] G. Guo, T. Huang, K. M. Tay, S. Weerasooriya, and A. Al-Mamun, “A DSP based hard disk drive servo test stand,” *IEEE Transactions on Magnetics*, vol. 34, no. 2, pp. 480–482, August 1998.
 - [23] M. Kobayashi and R. Horowitz, “Track seek control for hard disk dual-stage servo systems,” *IEEE Transactions on Magnetics*, vol. 37, no. 2, pp. 949–954, March 2001.
 - [24] S. Hara, T. Hara, L. Yi, and M. Tomizuka, “Novel reference signal generation for two-degree-of-freedom controllers for hard disk drives,” *IEEE/ASME Transactions on Mechatronics*, vol. 5, no. 1, pp. 73–78, March 2000.
 - [25] A. Dhanda and G. F. Franklin, “An improved 2-DOF proximate time optimal servomechanism,” *IEEE Transactions on Magnetics*, vol. 45, no. 5, pp. 2151–2164, May 2009.
 - [26] T. Yamaguchi, K. Shishida, S. Tohyama, and H. Hirai, “Mode switching control design with initial value compensation and its application to head positioning control on magnetic disk drives,” *IEEE Transactions on Industrial Electronics*, vol. 43, no. 1, pp. 65–73, February 1996.
 - [27] B. M. Chen, T. H. Lee, K. Peng, and V. Venkataramanan, “Composite non-linear feedback control for linear systems with input saturation: theory and an application,” *IEEE Transactions on Automatic Control*, vol. 48, no. 3, pp.

427–439, March 2003.

- [28] M. Hirata and M. Tomizuka, “Short track seeking of hard disk drives under multirate control-computationally efficient approach based on initial value compensation,” *IEEE/ASME Transactions on Mechatronics*, vol. 10, no. 5, pp. 535–545, October 2005.
- [29] Y. Li, V. Venkataramanan, G. Guo, and Y. Wang, “Dynamic nonlinear control for fast seek-settling performance in hard disk drives,” *IEEE Transactions on Industrial Electronics*, vol. 54, no. 2, pp. 951–962, April 2007.
- [30] Q. Hu, Q. Hu, C. Du, L. Xie, and Y. Wang, “Discrete-time sliding mode control with time-varying surface for hard disk drives,” *IEEE Transactions on Control Systems Technology*, vol. 17, no. 1, pp. 175–183, January 2009.
- [31] W. Lan, C. K. Thum, and B. M. Chen, “A hard-disk-drive servo system design using composite nonlinear-feedback control with optimal nonlinear gain tuning methods,” *IEEE Transactions on Industrial Electronics*, vol. 57, no. 5, pp. 1735–1745, May 2010.
- [32] C. K. Thum, C. Du, B. M. Chen, E. H. Ong, and K. P. Tan, “A unified control scheme for track seeking and following of a hard disk drive servo system,” *IEEE Transactions on Control Systems Technology*, vol. 18, no. 2, pp. 294–306, March 2010.
- [33] H. Hanselmann and A. Engelke, “LQG-control of a highly resonant disk drive head positioning actuator,” *IEEE Transactions on Industrial Electronics*, vol. 35, no. 1, pp. 100–104, February 1988.

- [34] Y. T. Teo and T. T. Tay, “Application of the l_1 -optimal regulation strategy to a hard disk servo system,” *IEEE Transactions on Control Systems Technology*, vol. 4, no. 4, pp. 467–472, July 1996.
- [35] J. K. Chang and H. T. Ho, “LQG/LTR frequency loop shaping to improve TMR budget,” *IEEE Transactions on Magnetics*, vol. 35, no. 5, pp. 2280–2282, September 1999.
- [36] Z. Li, G. Guo, B. M. Chen, and T. Lee, “Optimal track-following design for the highest tracks per inch in hard disk drives,” *Journal of Information Storage and Processing Systems*, vol. 3, no. 1–2, pp. 27–42, April 2001.
- [37] J. Zhou and Y. Wang, “Fast sliding-mode seek control of hard disk servos,” *Microsystem Technologies*, vol. 10, no. 1, pp. 35–41, December 2003.
- [38] W. C. Wu and T. S. Liu, “Sliding mode based learning control for track-following in hard disk drives,” *Mechatronics*, vol. 14, no. 8, pp. 861–876, October 2004.
- [39] Y. Kim, C. Kang, and M. Tomizuka, “Adaptive and optimal rejection of non-repeatable disturbance in hard disk drives,” in *Proceedings of IEEE/ASME International Conference on Advanced Intelligent Mechatronics*, Monterey, California, USA, July 24–38 2005, pp. 1–6.
- [40] F.-Y. Huang, T. Semba, W. Imaino, and F. Lee, “Active damping in *hdd* actuator,” *IEEE Transactions on Magnetics*, vol. 37, no. 2, pp. 847–849, March 2001.
- [41] M. T. White and M. Tomizuka, “Increased disturbance rejection in magnetic

- disk drives by acceleration feedforward control and parameter adaptation,” *Control Engineering Practice*, vol. 5, no. 6, pp. 741–751, June 1997.
- [42] S. Singh Pannu and R. Horowitz, “Increased disturbance rejection for hard disk drives by using accelerometers,” *Journal of Information Storage and Processing Systems*, vol. 1, no. 1, pp. 95–103, January 1999.
- [43] R. Oboe, “Use of low-cost MEMS accelerometers for vibration compensation in hard disk drives,” in *Proceedings of the 6th IEEE International Workshop on Advanced Motion Control*, Nagoya, Japan, March 30–April 1 2000, pp. 485–489.
- [44] A. Jinzenji, T. Sasamoto, K. Aikawa, S. Yoshida, and K. Aruga, “Acceleration feedforward control against rotational disturbance in hard disk drives,” *IEEE Transactions on Magnetics*, vol. 37, no. 2, pp. 888–893, March 2001.
- [45] K. Usui, M. Kisaka, A. Okuyama, and M. Nagashima, “Reduction of external vibration in hard disk drives using adaptive feed-forward control with single shock sensor,” in *Proceedings of 9th IEEE International Workshop on Advanced Motion Control*, Istanbul, Turkey, March 27–29 2006, pp. 138–143.
- [46] R. Oboe, E. Lasalandra, and M. T. White, *MEMS-based Accelerometers and their Application to Vibration Suppression in Hard Disk Drives*. Boston, MA: Springer US, 2006, pp. 993–1022.
- [47] P. Gao and S.-M. Swei, “Active actuation and control of a miniaturized suspension structure in hard-disk drives using a polyvinylidene-fluoride actuator and sensor,” *Measurement Science and Technology*, vol. 11, no. 2, pp. 89–94, November 1999.

- [48] J. Li, J. Xu, J. Liu, and H. Kohira, “Thermal mechanics of a contact sensor used in hard disk drives,” *Microsystem technologies*, vol. 19, no. 9-10, pp. 1607–1614, September 2013.
- [49] Y. Ma, S. Xue, J.-P. Peng, and D. B. Bogy, “Study of head-disk interface characterization using touchdown sensor and electromagnetic signal in hard disk drives,” *IEEE Transactions on Magnetics*, vol. 51, no. 11, pp. 1–4, November 2015.
- [50] Y. Li and R. Horowitz, “Active vibration control of a pzt actuated suspension in hard disk drives,” in *Proceedings of the American Control Conference*, vol. 2, Anchorage, AK, USA, May 8–10 2002, pp. 1366–1371.
- [51] Y. Li, R. Horowitz, and R. Evans, “Vibration control of a PZT actuated suspension dual-stage servo system using a PZT sensor,” *IEEE Transactions on Magnetics*, vol. 39, no. 2, pp. 932–937, March 2003.
- [52] Y. Li, F. Marcassa, R. Horowitz, R. Oboe, and R. Evans, “Track-following control with active vibration damping of a pzt-actuated suspension dual-stage servo system,” in *Proceedings of the 2003 American Control Conference*, Denver, Colorado, USA, June 4–6 2003, pp. 2553–2559.
- [53] S.-H. Lee, C. C. Chung, and C. W. Lee, “Active high-frequency vibration rejection in hard disk drives,” *IEEE/ASME Transactions on Mechatronics*, vol. 11, no. 3, pp. 339–345, June 2006.
- [54] Y. Huang, M. Banther, P. D. Mathur, and W. C. Messner, “Design and analysis of a high bandwidth disk drive servo system using an instrumented suspension,”

- IEEE/ASME Transactions on Mechatronics*, vol. 4, no. 2, pp. 196–206, June 1999.
- [55] S. Felix, S. Kon, J. Nie, and R. Horowitz, “Strain sensing with piezoelectric zinc oxide thin films for vibration suppression in hard disk drives,” in *Proceedings of the 2008 ASME Dynamic Systems and Control Conference*, Ann Arbor, Michigan, USA, October 20-22 2008, pp. 1455–1462.
- [56] S. Felix, J. Nie, and R. Horowitz, “Enhanced vibration suppression in hard disk drives using instrumented suspensions,” *IEEE Transactions on Magnetics*, vol. 45, no. 11, pp. 5118–5122, November 2009.
- [57] S. Felix and R. Horowitz, “Integration of thin film strain sensors into hard drives for active feedback vibration suppression,” *IEEE Sensors Journal*, vol. 13, no. 5, pp. 1708–1715, May 2013.
- [58] Y. Yuan, H. Du, K. S. Chow, M. Zhang, S. Yu, and B. Liu, “Performance analysis of an integrated piezoelectric ZnO sensor for detection of head-disk contact,” *Microsystem Technologies*, vol. 19, no. 9, pp. 1449–1455, September 2013.
- [59] J. Nie, “Control design and implementation of hard disk drive servos,” Ph.D. thesis, University of California, Berkeley, CA, USA, 2011.
- [60] J. J. Dosch, D. J. Inman, and E. Garcia, “A self-sensing piezoelectric actuator for collocated control,” *Journal of Intelligent Material Systems and Structures*, vol. 3, no. 1, pp. 166–185, January 1992.
- [61] E. H. Anderson, N. W. Hagood, and J. M. Goodliffe, “Self-sensing piezoelectric

- actuation: analysis and application to controlled structures,” in *Proceedings of the AIAA/ASME/ASCE/AHS/ASC 33rd structure, structural dynamics, materials conference*, Dallas, TX, USA, April 13–15 1992, pp. 166–185.
- [62] A. Preumont, *Vibration control of active structures: an introduction*, 3rd ed. Berlin: Springer, 2011.
- [63] H. Yamada, M. Sasaki, and Y. Nam, “Control of a micro-actuator for hard disk drives using self-sensing,” in *Proceedings of the 8th IEEE International Workshop on Advanced Motion Control*, Kawasaki, Japan, March 28 2004, pp. 147–152.
- [64] H. Yamada, M. Sasaki, and Y. Nam, “Active vibration control of a micro-actuator for hard disk drives using self-sensing actuator,” *Journal of Intelligent Material Systems and Structures*, vol. 19, no. 1, pp. 113–123, January 2008.
- [65] K. Chan and W. Liao, “Self-sensing actuators with passive damping for adaptive vibration control of hard disk drives,” *Microsystem Technologies*, vol. 15, no. 3, pp. 355–366, March 2009.
- [66] M. Sasaki, Y. Inoue, and H. Yamada, “Active vibration control of a microactuator for the hard disk drive using self-sensing actuation,” *Smart Materials Research*, vol. 2012, pp. 1–7, January 2012.
- [67] U. Boettcher, L. Matthes, B. Knigge, R. A. de Callafon, and F. E. Talke, “Suppression of cross-track vibrations using a self-sensing micro-actuator in hard disk drives,” *Microsystem technologies*, vol. 18, no. 9, pp. 1309–1317, September 2012.

- [68] C. K. Pang, G. Guo, B. M. Chen, and T. H. Lee, "Nanoposition sensing and control in HDD dual-stage servo systems," in *Proceedings of the IEEE International Conference on Control Applications*, Taipei, Taiwan, September 2–4 2004, pp. 551–556.
- [69] C. K. Pang, G. Guo, B. M. Chen, and T. H. Lee, "Self-sensing actuation for nanopositioning and active-mode damping in dual-stage HDDs," *IEEE/ASME Transactions on Mechatronics*, vol. 11, no. 3, pp. 328–338, June 2006.
- [70] F. Hong and C. K. Pang, "Robust vibration control at critical resonant modes using indirect-driven self-sensing actuation in mechatronic systems," *ISA transactions*, vol. 51, no. 6, pp. 834–840, November 2012.
- [71] B. Hu, J. Wan, and C. K. Pang, "Self-sensing actuation for improved audio-induced vibration rejection in dual-stage hard disk drives," *Microsystem Technologies*, in press.
- [72] B. Hu, J. Wan, and C. K. Pang, "Head-on-media detection with PZT self-sensing actuation in dual-stage hard disk drives," *IEEE Transactions on Magnetics*, in press.
- [73] P. Vallone, "High-performance piezo-based self-sensor for structural vibration control," in *Proceedings of the SPIE Conference on Smart Structures*, vol. 2443, San Diego, USA, February 1995, pp. 643–655.
- [74] B. Ko and B. H. Tongue, "Acoustic control using a self-sensing actuator," *Journal of Sound and Vibration*, vol. 187, no. 1, pp. 145–165, October 1995.
- [75] C. Moutinho, A. Cunha, and E. Caetano, "Implementation of an active damping

- system to reduce harmonic vibrations in a 3-DOF model,” in *Proceedings of ECCOMAS Thematic Conference on Smart Structures and Materials*, Lisbon, Portugal, 2005.
- [76] Y. Y. Lim, S. Bhalla, and C. K. Soh, “Structural identification and damage diagnosis using self-sensing piezo-impedance transducers,” *Smart Materials and Structures*, vol. 15, no. 4, pp. 987–995, June 2006.
- [77] A. S. Putra, S. Huang, K. K. Tan, S. K. Panda, and T. H. Lee, “Self-sensing actuation with adaptive control in applications with switching trajectory,” *IEEE/ASME Transactions on Mechatronics*, vol. 13, no. 1, pp. 104–111, February 2008.
- [78] S. Kuiper and G. Schitter, “Self-sensing actuation and damping of a piezoelectric tube scanner for atomic force microscopy,” in *Proceedings of the 2009 European Control Conference*, Budapest, Hungary, August 23–26 2009, pp. 3887–3892.
- [79] A. Pelletier, P. Micheau, and A. Berry, “Implementation of a self-sensing piezoelectric actuator for vibro-acoustic active control,” in *Proceedings of the SPIE Smart Structures and Materials, Nondestructive Evaluation, and Health Monitoring*, San Diego, California, USA, April 10 2014, pp. 1–10.
- [80] S. I. Moore and S. R. Moheimani, “Vibration control with MEMS electrostatic drives: A self-sensing approach,” *IEEE Transactions on Control Systems Technology*, vol. 23, no. 3, pp. 1237–1244, May 2015.
- [81] G. E. Simmers, J. R. Hodgkins, D. D. Mascarenas, G. Park, and H. Sohn,

- “Improved piezoelectric self-sensing actuation,” *Journal of Intelligent Material Systems and Structures*, vol. 15, no. 12, pp. 941–953, December 2004.
- [82] G. E. Simmers Jr, H. A. Sodano, G. Park, and D. J. Inman, “Thermal protection for a self-sensing piezoelectric control system,” *Smart Materials and Structures*, vol. 16, no. 6, pp. 2492–2500, October 2007.
- [83] D. G. Cole and R. L. Clark, “Adaptive compensation of piezoelectric sensoriaactuators,” *Journal of Intelligent Material Systems and Structures*, vol. 5, no. 5, pp. 665–672, September 1994.
- [84] J. Viperman and R. Clark, “Implementation of an adaptive piezoelectric sensoriaactuator,” *AIAA Journal*, vol. 34, no. 10, pp. 2102–2109, October 1996.
- [85] C. A. Fannin, “Design of an analog adaptive piezoelectric sensoriaactuator,” Master’s thesis, Virginia Polytechnic Institute and State University, Blacksburg, Virginia, 1997.
- [86] W. W. Law, W. Liao, and J. Huang, “Vibration control of structures with self-sensing piezoelectric actuators incorporating adaptive mechanisms,” *Smart Materials and Structures*, vol. 12, no. 5, pp. 720–730, September 2003.
- [87] S. Kuiper and G. Schitter, “Active damping of a piezoelectric tube scanner using self-sensing piezo actuation,” *Mechatronics*, vol. 20, no. 6, pp. 656–665, September 2010.
- [88] M. Asghari, S. M. Rezaei, A. H. Rezaie, M. Zareinejad, and H. Ghafarirad, “Self-sensing actuation using online capacitance measurement with application to active vibration control,” *Journal of Intelligent Material Systems and Structures*

- tures*, vol. 26, no. 2, pp. 186–200, January 2015.
- [89] L. D. Jones and E. Garcia, “Novel approach to self-sensing actuation,” in *Proceedings of 1997 Smart Structures and Materials*, San Diego, CA, USA, June 6 1997, pp. 305–314.
 - [90] A. Kawamata, Y. Kadota, H. Hosaka, and T. Morita, “Self-sensing piezoelectric actuator using permittivity detection,” *Ferroelectrics*, vol. 368, no. 1, pp. 194–201, March 2008.
 - [91] Y. Ishikiriyama and T. Morita, “Improvement of self-sensing piezoelectric actuator control using permittivity change detection,” *Journal of Advanced Mechanical Design, Systems, and Manufacturing*, vol. 4, no. 1, pp. 143–149, January 2010.
 - [92] K. Saigusa and T. Morita, “Self-sensing control of piezoelectric positioning stage by detecting permittivity,” *Sensors and Actuators A: Physical*, vol. 226, pp. 76–80, May 2015.
 - [93] M. Rakotondrabe, I. A. Ivan, S. Khadraoui, P. Lutz, and N. Chaillet, “Simultaneous displacement/force self-sensing in piezoelectric actuators and applications to robust control,” *IEEE/ASME Transactions on Mechatronics*, vol. 20, no. 2, pp. 519–531, April 2015.
 - [94] S. Knight. “HGST becomes first to introduce 10tb hard drive in 3.5 inch form factor”, September 2014. [Online]. Available: <http://www.techspot.com/news/58010-hgst-becomes-first-to-introduce-10tb-hard-drive-in-35-form-factor.html>
 - [95] “IEEE Standard on Piezoelectricity,” *ANSI/IEEE Std 176-1987*, pp. 176–1987,

1988.

- [96] A. J. Fleming, A. G. Wills, and S. O. R. Moheimani, “Sensor fusion for improved control of piezoelectric tube scanners,” *IEEE Transactions on Control Systems Technology*, vol. 16, no. 6, pp. 1265–1276, November 2008.
- [97] Y. K. Yong, A. J. Fleming, and S. O. Moheimani, “A novel piezoelectric strain sensor for simultaneous damping and tracking control of a high-speed nanopositioner,” *IEEE/ASME Transactions on Mechatronics*, vol. 18, no. 3, pp. 1113–1121, June 2013.
- [98] Y. Liu, “Analytical dynamic model for suspension with pzt actuators,” *Microsystem Technologies*, vol. 19, no. 9, pp. 1269–1274, September 2013.
- [99] S. O. R. Moheimani and A. J. Fleming, *Piezoelectric Transducers for Vibration Control and Damping*. Springer Verlag London Limited, 2006.
- [100] K. Mori, T. Munemoto, H. Otsuki, Y. Yamaguchi, and K. Akagi, “A dual-stage magnetic disk drive actuator using a piezoelectric device for a high track density,” *IEEE Transactions on Magnetics*, vol. 27, no. 6, pp. 5298–5300, November 1991.
- [101] L. Guo, D. Martin, and D. Brunnett, “Dual-stage actuator servo control for high density disk drives,” in *Proceedings of IEEE/ASME International Conference on Advanced Intelligent Mechatronics*, Atlanta, USA, September 19–23 1999, pp. 132–137.
- [102] Y.-H. Kim and S.-H. Lee, “An approach to dual-stage servo design in computer disk drives,” *IEEE Transactions on Control Systems Technology*, vol. 12, no. 1,

pp. 12–20, January 2004.

- [103] R. Horowitz, Y. Li, K. Oldham, S. Kon, and X. Huang, “Dual-stage servo systems and vibration compensation in computer hard disk drives,” *Control Engineering Practice*, vol. 15, no. 3, pp. 291–305, March 2007.
- [104] G. Guo, D. Wu, and T. C. Chong, “Modified dual-stage controller for dealing with secondary-stage actuator saturation,” *IEEE Transactions on Magnetics*, vol. 39, no. 6, pp. 3587–3592, November 2003.
- [105] C. K. Pang, D. Wu, G. Guo, T. C. Chong, and Y. Wang, “Suppressing sensitivity hump in HDD dual-stage servo systems,” *Microsystem Technologies*, vol. 11, no. 8, pp. 653–662, August 2005.
- [106] G. Herrmann, M. C. Turner, I. Postlethwaite, and G. Guo, “Practical implementation of a novel anti-windup scheme in a HDD-dual-stage servo-system,” *IEEE/ASME Transactions on Mechatronics*, vol. 9, no. 3, pp. 580–592, September 2004.
- [107] I. Postlethwaite, M. C. Turner, and J. Sofrony, “Anti-windup synthesis using Riccati equations,” *International Journal of Control*, vol. 80, no. 1, pp. 112–128, November 2007.
- [108] B. Hu, C. K. Pang, J. Wan, Y.-H. Kim, and J. K. Tan, “Earliest switch-on of dual-stage actuation in hard disk drives,” *Microsystem Technologies*, vol. 22, no. 6, pp. 1267–1273, June 2016.
- [109] E. G. Gilbert and K. T. Tan, “Linear systems with state and control constraints: the theory and application of maximal output admissible sets,” *IEEE*

- Transactions on Automatic Control*, vol. 36, no. 9, pp. 1008–1020, September 1991.
- [110] R. S. Stockton, *Introduction to linear programming*, 2nd ed. Boston: Allyn and Bacon, 1963.
 - [111] D. Wu, G. Guo, and T. C. Chong, “Midfrequency disturbance suppression via micro-actuator in dual-stage HDDs,” *IEEE Transactions on Magnetics*, vol. 38, no. 5, pp. 2189–2191, September 2002.
 - [112] J. Zheng, C. Du, G. Guo, Y. Wang, J. Zhang, Q. Li, and B. Hredzak, “Phase lead peak filter method to high TPI servo track writer with microactuators,” in *Proceedings of the 2006 American Control Conference*, Minneapolis, MN, USA, June 14–16 2006, pp. 1309–1314.
 - [113] J. X. Xu, D. Huang, V. Venkataramanan, and T. C. T. Huynh, “Adaptive compensation of contact-induced vibration in high density HDD servo systems using peak filter method,” in *Proceedings of the IEEE International Symposium on Industrial Electronics*, Hangzhou, China, May 28–31 2012, pp. 797–802.
 - [114] L. Sun, X. Chen, and M. Tomizuka, “Enhanced wide-spectrum vibration suppression based on adaptive loop shaping,” in *Proceedings of the American Control Conference*, Boston, MA, USA, July 6–8 2016, pp. 6189–6194.
 - [115] J. Zheng, G. Guo, Y. Wang, and W. E. Wong, “Optimal narrow-band disturbance filter for PZT-actuated head positioning control on a spindisk,” *IEEE Transactions on Magnetics*, vol. 42, no. 11, pp. 3745–3751, November 2006.
 - [116] Q. Zheng and M. Tomizuka, “A disturbance observer approach to detecting and

- rejecting narrow-band disturbances in hard disk drives,” in *Proceedings of the 10th IEEE International Workshop on Advanced Motion Control*, Trento, Italy, March 26–28 2008, pp. 254–259.
- [117] Q. Jia, “Disturbance rejection through disturbance observer with adaptive frequency estimation,” *IEEE Transactions on Magnetics*, vol. 45, no. 6, pp. 2675–2678, June 2009.
- [118] J. Wang, Y. Wang, and S. Cao, “Add-on feedforward compensation for vibration rejection in HDD,” *IEEE/ASME Transactions on Mechatronics*, vol. 16, no. 6, pp. 1164–1170, December 2011.
- [119] S. Kumar, V. D. Khanna, and M. Sri-Jayantha, “A study of the head disk interface shock failure mechanism,” *IEEE Transactions on Magnetics*, vol. 30, no. 6, pp. 4155–4157, November 1994.
- [120] G. H. Jang and S. J. Park, “Sensorless detection of a free-falling hard disk drive by electromechanical signal of a spindle motor,” *IEEE Transactions on Magnetics*, vol. 41, no. 10, pp. 3943–3945, October 2005.
- [121] S. Imai, M. Tokuyama, S. Hirose, G. J. Burger, T. S. J. Lammerink, and J. H. J. Fluitman, “A thin-film piezoelectric impact sensor array fabricated on a Si slider for measuring head-disk interaction,” *IEEE Transactions on Magnetics*, vol. 31, no. 6, pp. 3009–3011, November 1995.
- [122] S. V. Canchi, D. B. Bogy, R.-H. Wang, and A. N. Murthy, “Parametric investigations at the head-disk interface of thermal fly-height control sliders in contact,” *Advances in Tribology*, vol. 2012, pp. 1–11, November 2012.

- [123] S. Kim, G. Lim, N.-C. Park, Y.-P. Park, H.-C. Lee, J.-H. Kim, and K.-S. Park, "Analysis of contact phenomena between a head stack assembly and disk during operational shock," *Microsystem Technologies*, vol. 19, no. 9, pp. 1587–1593, September 2013.
- [124] L. M. Matthes, B. Knigge, and F. E. Talke, "Head-disk proximity sensing using contact sensors in hard disk drives," *IEEE Transactions on Magnetics*, vol. 50, no. 11, pp. 1–4, November 2014.
- [125] G. Lim, K.-S. Park, N.-C. Park, Y.-P. Park, Y. Lee, Y. B. Chang, and C.-s. Kim, "Design parametric study on the influence of anti-shock performance during operational condition for a 2.5 inch HDD," *Microsystem Technologies*, vol. 21, no. 12, pp. 2705–2715, December 2015.
- [126] A. Daugela and S. Tadepalli, "Low SNR signal processing for head/media contact detection in hdd," *Microsystem Technologies*, vol. 21, no. 12, pp. 2679–2684, December 2015.
- [127] J. S. Viperman, "Simultaneous qualitative health monitoring and adaptive piezoelectric sensoriaction," *AIAA Journal*, vol. 39, no. 9, pp. 1822–1825, April 2001.
- [128] S. O. R. Moheimani, A. J. Fleming, and S. O. service), *Piezoelectric transducers for vibration control and damping*, 1st ed. London: Springer, 2006.
- [129] S. S. Aphale, A. J. Fleming, and S. O. Reza Moheimani, "Integral resonant control of collocated smart structures," *Smart Materials and Structures*, vol. 16, no. 2, pp. 439–446, February 2007.

- [130] E. Pereira, S. S. Aphale, V. Feliu, and S. O. R. Moheimani, “Integral resonant control for vibration damping and precise tip-positioning of a single-link flexible manipulator,” *IEEE/ASME Transactions on Mechatronics*, vol. 16, no. 2, pp. 232–240, April 2011.
- [131] A. Al-Mamun, E. Keikha, C. S. Bhatia, and T. H. Lee, “Integral resonant control for suppression of micro-actuator resonance in dual stage actuator,” *IEEE Transactions on Magnetics*, vol. 48, no. 11, pp. 4614–4617, November 2012.
- [132] A. Al-Mamun, E. Keikha, C. S. Bhatia, and T. H. Lee, “Integral resonant control for suppression of resonance in piezoelectric micro-actuator used in precision servomechanism,” *Mechatronics*, vol. 23, no. 1, pp. 1–9, February 2013.

List of Publications

The research work related to this dissertation resulted in the following publications:

a) International refereed journals

1. B. Hu, J. Wan, C. K. Pang, and J. K. Tan, “Head-on-media detection with PZT self-sensing actuation in dual-stage hard disk drives,” *IEEE Transactions on Magnetics*, in press.
2. B. Hu, J. Wan, and C. K. Pang, “Self-sensing actuation for improved audio-induced vibration rejection in dual-stage hard disk drives,” *Microsystem Technologies*, in press.
3. B. Hu, C. K. Pang, J. Wan, Y. -H. Kim, and J. K. Tan, “Earliest switch-on of dual-stage actuation in hard disk drives,” *Microsystem Technologies*, vol. 22, no. 6, pp. 1267–1273, June 2016.

b) International refereed conference proceedings

1. B. Hu, J. Wan, C. K. Pang, and J. K. Tan, “Head-on-media detection with PZT self-sensing actuators,” in *Digests of the 2016 APMRC*, S3–03, Seoul, Korea, July 13–15 2016 (invited).
2. B. Hu, J. Wan, C. K. Pang, F. Hong, J. K. Tan, “Enhanced indirect-driven self-sensing actuation for piezoelectric structures,” in *Proceedings of the*

2016 ASME Conference on ISPS, ISPS2016–9505, Santa Clara, CA, USA, June 20–21 2016.

3. B. Hu, C. K. Pang, J. Wan, Y. -H. Kim, and J. K. Tan, “Earliest switch-on of dual-stage actuation in hard disk drives,” in *Proceedings of the 2015 JSME-IIP/ASME-ISPS Joint Conference on MIPE*, MoD–1–1, Kobe, Japan, June 14–17 2015.

His other publications include:

a) International refereed journals

1. M. Luo, H. -C. Yan, B. Hu, J. -H. Zhou, and C. K. Pang, “A data-driven two-stage maintenance framework for degradation prediction in semiconductor manufacturing industries,” *Computers & Industrial Engineering*, vol. 85, pp. 414–422, July 2015.

b) International refereed conference proceedings

1. B. Hu, M. Luo, C. K. Pang, X. Li, and H. L. Chan, “A two-stage equipment predictive maintenance framework for high-performance manufacturing systems,” in *Proceedings of the 2012 IEEE ICIEA*, ThPP.1, Singapore, July 18–20 2012.